Chromium-based alloys for high temperature applications – The importance of Mo in the A2-A15 and A2-B2 system

Von der Fakultät für Ingenieurwissenschaften

der Universität Bayreuth

zur Erlangung der Würde

Doktor-Ingenieurin (Dr.-Ing.)

genehmigte Dissertation

von

M.Sc. Lisa Zander

aus

Siegburg

Erstgutachter: Prof. Dr.-Ing. Mathias Christian Galetz
Zweitgutachter: Prof. Dr.-Ing. Martin Heilmaier

Tag der mündlichen Prüfung: 09.07.2026

Lehrstuhl für Metallische Werkstoffe

Universität Bayreuth

2026

Abstract

The continuous increase of greenhouse gas emissions and the resulting climate change require urgent improvements in energy efficiency and decarbonization across all major industrial sectors. In the aviation and energy conversion industries, increasing operating temperatures and reducing component weight are among the most effective strategies to improve efficiency. However, the service temperatures of state-of-the-art structural materials, namely nickel-based superalloys, are already well-optimized and have reached their limit. Chromium-based alloys represent a promising alternative material class due to their high melting temperature, low density, good thermal conductivity, and favorable availability, yet their application has been historically limited by low-temperature brittleness and insufficient oxidation and nitridation resistance.

This work systematically investigates Cr-based alloys, precipitation-strengthened with the Cr_3Si intermetallic phase, with the objective to extend their application window beyond that of Ni-based superalloys. The primary focus lies on the Cr-rich two-phase A2(Cr) + A15(Cr_3Si) system alloyed with molybdenum (Mo), specifically Cr-xMo-8 at.%Si alloys with Mo contents between 0 and 40 at.%. The role of Mo on phase stability, microstructure, oxidation and nitridation behavior at 1200 °C and mechanical properties from room temperature up to 1000 °C is assessed. Based on the insights gained, an alternative precipitation strategy is developed by replacing the A15($(Cr,Mo)_3Si$) phase with low-misfit B2 (NiAl) precipitates, resulting in a BCC superalloy A2 + B2 concept within the Cr-Mo-Si-Ni-Al system.

The results demonstrate that Mo is a highly effective alloying element in Cr-based alloys, providing strong solid-solution strengthening, pronounced grain refinement, suppression of nitridation, and significantly improved oxidation behavior. An optimal Mo content around 25 at.% yields an attractive combination of high specific strength (100 $N \cdot m \cdot g^{-1}$ at 1000°C vs. 40 $N \cdot m \cdot g^{-1}$ for Ni-based MAR-M-247) and oxidation resistance at temperatures up to 1200 °C, though at the expense of low fracture toughness and a higher ductile-to-brittle transition temperature. The introduction of B2 precipitates improves upon the room-temperature fracture toughness limitations of the A2 + A15 system, while enabling strength up to higher temperatures as compared to the A15-

strengthened alloys. Overall, this work establishes Cr-based Cr-Mo-Si (A2 + A15) and Cr-Mo-Si-Ni-Al (A2 + B2) alloys as promising candidates for next-generation high-temperature structural materials and provides a foundation for further alloy and processing optimization.

Kurzfassung

Der kontinuierliche Anstieg der Treibhausgasemissionen und der daraus resultierende Klimawandel erfordern dringend Verbesserungen der Energieeffizienz und der Dekarbonisierung in allen wichtigen Industriesektoren. In der Luftfahrt sowie in Energiewandlungstechnologien zählen die Erhöhung der Servicetemperaturen und die Reduzierung des Bauteilgewichts zu den effektivsten Strategien zur Effizienzsteigerung. Nickelbasis-Superlegierungen sind der aktuelle technische Standard für Hochtemperatur-Strukturwerkstoffe, jedoch ist die Legierungsentwicklung hinsichtlich ihrer Einsatztemperatur ausgereizt. Chrombasis-Legierungen stellen aufgrund ihrer hohen Schmelztemperatur, geringen Dichte, guten Wärmeleitfähigkeit und günstiger Rohstoffverfügbarkeit eine vielversprechende alternative Werkstoffklasse dar. Ihre Anwendung ist jedoch historisch durch unzureichende Duktilität bei niedrigen Temperaturen, sowie eine unzureichende Oxidations- und Nitrierungsbeständigkeit begrenzt.

Diese Arbeit untersucht systematisch Cr-basierte Legierungen, die mittels der intermetallischen Phase Cr_3Si ausscheidungsgehärtet sind, mit dem Ziel, ihr Anwendungsfenster über das von Ni-basierten Superlegierungen hinaus zu erweitern. Der Schwerpunkt liegt auf dem Cr-reichen zweiphasigen A2(Cr) + A15(Cr_3Si)-System, das mit Molybdän (Mo) legiert ist, insbesondere auf Cr-xMo-8 at.% Si-Legierungen mit Mo-Gehalten zwischen 0 und 40 at.%. Der Einfluss von Mo auf Phasenstabilität, Mikrostruktur, Oxidations- und Nitrierungsverhalten bei 1200 °C sowie auf die mechanischen Eigenschaften von Raumtemperatur bis zu 1000 °C wird untersucht. Auf Basis der gewonnenen Erkenntnisse wird eine alternative Ausscheidungsstrategie entwickelt, bei der die A15-Phase ($(Cr,Mo)_3Si$) durch B2-(NiAl-)Ausscheidungen mit sehr geringer Gitterfehlanpassung ersetzt wird, was zu einem A2 + B2-Legierungskonzept im System Cr-Mo-Si-Ni-Al führt.

Die Ergebnisse zeigen, dass Mo ein äußerst effektives Legierungselement in Cr-basierten Legierungen ist und eine starke Mischkristallhärtung, ausgeprägte Kornverfeinerung, eine Unterdrückung der Nitrierung sowie eine signifikant verbesserte Oxidationsbeständigkeit bewirkt. Ein optimaler Mo-Gehalt von etwa 25 at.% führt zu einer attraktiven Kombination aus hoher spezifischer Festigkeit

(100 $N \cdot m \cdot g^{-1}$ bei 1000°C vs. 40 $N \cdot m \cdot g^{-1}$ für die Ni-basierte Legierung MAR-M-247) und Oxidationsbeständigkeit bei Temperaturen bis zu 1200 °C, allerdings auf Kosten einer geringen Bruchzähigkeit bei Raumtemperatur und einer erhöhten Spröd-Duktil-Übergangstemperatur. Die Einführung von B2-Ausscheidungen verbessert erfolgreich die Bruchzähigkeit bei Raumtemperatur verglichen mit dem A2 + A15-System und ermöglicht eine Hochtemperaturfestigkeit, die die von A15-gehärteten Legierungen übertrifft. Insgesamt etabliert diese Arbeit Cr-basierte Cr-Mo-Si (A2 + A15) und Cr-Mo-Si-Ni-Al (A2 + B2) Legierungen als vielversprechende Kandidaten für Hochtemperatur-Strukturwerkstoffe der nächsten Generation und schafft eine Grundlage für weitere Legierungs- und Prozessoptimierungen.

Acknowledgements

Prof. Dr.-Ing. Mathias Christian Galetz: Thank you for recruiting me to work for DECHEMA-Research Institute (DFI). Not only trusting me in taking control over a four-year BMWK ‘LuFo’ project, but also giving me freedom to shape it into the direction I wanted to. This unexpected opportunity was a once in a lifetime chance and a very pleasant way to work on a dissertation. I am very thankful for this time. Your expertise and interest in material science especially in the high temperature materials led to very helpful discussions and always enabled me to confidently plan my next steps during this project. Which is truly showing that you are a well-equipped advisor, helping to shape the next generation of material scientists.

I am grateful also for everyone at the DFI especially the high temperature alloys team lead by Dr. Emma White. Thank you for the discussions, advice, support, training and good times spend together at conferences. Additionally to Emma for proofreading this work and my publications. To name a few DFI members who especially helped with this thesis: Mathias Röhrig - Helping me and enabling me to build my furnace set-ups in the lab and improving them. Heinrich Kopietz, Yvonne Hohmann and Jano Bender from the workshop performing electrical discharge machining on my alloys. Dr. Gerald Schmidt for execution of the EPMA-WDS, always carefully sticking to my instructions and willing to discuss the results with me. The same holds true for Melanie Thalheimer performing EBSD measurements on my cross sections. Thanks for the valuable tips on metallographic preparation from Ellen Berghof-Hasselbächer, Daniela Hasenpflug and Susann Rudolphi.

Thank you to all the Bachelor and Master students I worked with that helped to investigate even more exciting topics around the Cr-based alloys developed in this work: Pelle Wolf (Cr-V system), Sahiti Katepalli (Water vapor influence on corrosion + coatings), Sarah Auler (Hot Corrosion of Cr based material). All the best for your future careers and personal journey.

To all co-authors of the publications thank you for your interest in the topic the discussions, comments and edits on the manuscripts. Especially thanks to Dr. Thomas Blackburn and Prof. Dr. Alexander J. Knowles (School of Metallurgy and Materials, University of Birmingham) for taking my A2-B2 alloy to perform synchrotron XRD measurements.

Thanks to Prof. Dr. Alexander Kauffmann (Universität Bochum) for arc-melting some of the larger alloy buttons in the AM 200 system (back then at Karlsruhe Institute of technology). For the possibility to let me perform high load Vickers tests (at Staatliche Materialprüfungsanstalt), I want to thank Jurica Filipovic, Fabrizio Windhaus, Robert Kopp and Gerwin van den Dungen from the Technical University of Darmstadt.
Last but not least I want to acknowledge the German Federal Ministry for Economic Affairs and Energy (BMWE) for the financial support of the project under grant no. 20E2125 based on a decision of the German Bundestag.

On a more personal note:
I am repeating words from my Master thesis: “I am very grateful that I was able to make my first work experience in the scientific world, several years ago, under the lead of Dr. Mark Rikel, who I think highly of as a person and who is an exceptionally good scientist. Thank you for always generously sharing your knowledge and excitement for science. Your curiosity is contagious and was one of the reasons that made me start a Master’s distance study program” - and now I even wrote my dissertation.…who would have thought?
I want to thank my parents and sisters, my brother-in-law and nephew and friends for the support they were able to give. Also, my now additional family-in-law thank you for your kindness and interest. Especially thanks to the Zanders for generously sharing their name with me.
My husband Dr. Ing. (first in the family) Julian Zander for your support and love. Having you (and our furry little one Jinbe) around makes life so much better. I can’t wait for the next addition to our family.

Table of Contents

List of abbreviations

AC	As-cast
AN	Annealed
at.%	Atomic percent
BCC	Body-centered cubic
BSE	Backscattered electron mode
CMC	Ceramic matrix composites
CRSS	Critical resolved shear stress
CSP	Concentrated solar power plants
DBTT	Ductile-to-brittle transition temperature
EBSD	Electron backscatter diffraction
EDS	Energy-dispersive X-ray spectroscopy
EPMA	Electron probe microanalysis
FCC	Face-centered cubic
GHG	Greenhouse Gas
HV	Vickers hardness
SE	Secondary electron mode
SEM	Scanning electron microscopy
SFE	Stacking fault energy
SXRD	Synchrotron X-ray diffraction
TCP	Topologically close-packed
TGA	Thermogravimetric analysis
V_f	Volume fraction
vol%	Volume percent
WDS	Wavelength-dispersive X-ray spectroscopy
wt.%	Weight percent
XRD	X-ray diffraction

List of symbols

A	Area
c	Crack length (in high load Vickers test)
F	Force
K_I	Fracture toughness
k_p	Parabolic rate constant
k_V	Volatilization rate constant
l	Length
l_0	Initial length
M	Molar mass
t	Time
T	Temperature
T_m	Melting temperature
V	Volume
α	Opening angle of the Vickers pyramid (136°)
ΔG	Gibbs free energy change
Δl	Change in length
Δm	Mass change
ε	Strain
δ	Density
σ	Stress

List of figures

List of tables

1. Introduction

Eunice Newton Foote was the first to describe a direct connection between the carbon dioxide (CO_2) concentration in the air and the warming of the earth's atmosphere as early as 1865 [1]. First publications, linking the “enormous quantity” of carbon dioxide [2], which had been introduced into the atmosphere by the combustion of fossil fuels to “climatic changes” [3], appeared a century later between 1957 and 1968. By the early 1970s, more scientific evidence confirmed that global warming is primarily driven by human-made greenhouse gas emissions (GHG – consisting not only of CO_2 but also water vapor, methane, nitrous oxide, ozone), mainly stemming from industrialization and the burning of fossil fuels [4]. While climate scientists warned governments and the public at that time, widespread public awareness and acceptance of the risks, both to ecosystems and to future generations, developed much more slowly [5]. In 1987 the “World Commission on Environment and Development” described in the so-called “Brundtland report” that global warming from CO_2 emissions leads to “terrible consequences” for our planet [5]. In this report the term sustainable development was defined as “[…] development that meets the needs of the present without compromising the ability of future generations to meet their own needs” [5]. Due to the multiple decades of delay in applying effective countermeasures, today many internationally agreed-to targets for limiting GHG emissions require urgent and ambitious actions to remain achievable and to limit global warming to levels that keep the planet broadly habitable for humanity in the future.

The European commission published goals to become climate-neutral by 2050 with an intermediate step of reducing net GHG emissions by at least 55% until 2030, which corresponds to the GHG levels present at 1990 [6]. To achieve these goals, primary focus is put on decarbonization and increasing energy efficiencies of processes and components. This also emphasizes the increased relevance of research and innovation, especially in the transport and energy sector, which together account for > 60% of the world-wide CO_2 emissions [7].

In the field of transport via aviation, which is the targeted application field in this work, decarbonization and increase of energy efficiency can be advanced,

amongst other things, by choice of the structural material deployed in the aircraft. Though aviation only accounts for approximately 3% of global CO_2 emissions [7] developing new materials, which have long term stability under various demanding conditions, is also relevant for new and innovative types of energy production. Electricity and heat are accountable for > 40% of global CO_2 emissions [7], so employing new technologies, e.g. concentrated solar power plants (CSP) and biomass combustion is desirable [8, 9].

One of the most challenging environments for structural materials is in the propulsion systems for aircrafts, namely gas turbines. When considering optimization for energy efficiency, reducing overall weight and operating at higher service temperatures yield the clearest benefits [10]. Further reducing efficiency losses by discarding techniques like internal cooling of turbine blades, can help additionally, but cannot be easily implemented due to the lack of available structural materials that operate at temperatures above 1000 °C [10]. In the hottest areas of the gas turbines, typically nickel-based superalloys are the state-of-the-art material. Single-crystal Ni-based alloys can operate at service temperatures up to 1100 °C, while their polycrystalline siblings usually are maxed out at 980 °C [11, 12]. The relatively low melting temperature of Ni, prohibits further increasing the service temperature. Surpassing the limits of Ni-based superalloys with their unique combination of well-balanced properties, remains a monumental challenge amongst material scientists. For lower temperature sections (up to 650 °C), lightweight titanium aluminide (TiAl) based alloys made it into gas turbines in the late 2000s [13]; embrittlement, as well as insufficient oxidation resistance, of TiAl-based materials still exclude them from being used in higher temperature areas [14].

Approaches to go beyond the service temperature of Ni-based superalloys usually lead to materials that have a heavily imbalanced property profile that can provide mechanical resistance but little oxidation resistance. Recently, ceramic matrix composites (CMC) have been discussed for replacing metallic alloys at higher service temperatures, promising strong weight reduction and potentially enabling higher operating temperatures, but also bringing along issues like fabricability, lack of repair techniques and low damage tolerance [15]. Remaining in the more traditional field of metallic materials, the focus in the last decades has

been on refractory-based alloys [16]. Due to their high melting temperatures, they promise higher service temperature capability. Especially Mo- and Nb-based alloys were intensely investigated [16, 17, 18, 19, 20], both having tremendous high temperature strength, but very poor oxidation behavior at the targeted service temperatures above 1000 °C. Mo forms volatile MoO_3 [21] leading to so-called “pesting” phenomena (catastrophic disintegration), which is typically dominant around 800 °C, while Nb-based materials form very voluminous unprotective oxides [17, 18].

Developing chromium-based alloys with the focus on a balanced property profile, to go beyond the application field of Ni-based alloys, is the goal of this work. Between the 1940-70s Cr-based alloys received some attention, and their key properties were investigated, focusing on increasing their ductility at low temperatures and on strengthening methods for high-temperature applications. The ‘iodide process’ that enabled the production of high-purity Cr was developed in the early 1950s [22] and was key in studying Cr-based alloys and later identifying nitrogen (N) as major impurity in Cr which causes brittleness [22]. Interest in Cr peaked around 1955 at a conference about “Ductile Cr-based alloys”, which was held in Cleveland, Ohio [22, 23]. Around the 1980s the development of single crystal Ni-based superalloys enabled increased operating temperatures [24] and research on Cr-based alloys was forgotten for a while [25]. With increasing Ni price and decreasing availability [26, 27], Cr once more received attention. Starting from the 1990s, again more research on Cr-based materials was published, focusing on overcoming the main challenges: low temperature brittleness and high temperature nitridation effects, to finally make use of the promising key features of Cr, namely: low density, high melting point, high thermal conductivity, good availability and lower price [26, 27, 28]. Especially alloying silicon (Si) and molybdenum (Mo) showed promise to counterbalance some of the disadvantages of Cr-based materials. Si strengthens the alloy by forming the intermetallic A15 phase, Cr_3Si, and improves oxidation resistance [29, 30, 31]. Mo provides solid solution strengthening, improves creep resistance and has shown a beneficial effect on reducing nitridation of Cr [29, 32, 33, 34, 35].

This work systematically investigates the role of Mo in the Cr-rich two phase (A2 + A15) Cr-xMo-8 at.%Si system. Based on the results, the alloying strategy is expanded to an alternative precipitate for the Cr-based alloy, by using an A2 + B2 approach utilizing NiAl precipitates. The overall goal is to advance Cr-based alloys and alloying strategies, defining future research fields and application windows for high temperature Cr-based alloys.

1.1 Chromium based alloys for high temperature application – Chances and challenges

When selecting or designing structural materials for high-temperature applications (>500 °C), two aspects of the property profile must be considered. Firstly, the mechanical performance is critical. This includes sufficient ductility and fracture toughness at room temperature to ensure manufacturability and adequate high-temperature strength, creep resistance and fatigue resistance under service conditions. Secondly, environmental stability plays a decisive role. The suitability of a material is strongly influenced by its oxidation and corrosion behavior at the intended operating temperature and in the relevant service atmospheres. For a given application, these mechanical and environmental requirements must be balanced to ensure both structural integrity and long-term durability.

For oxidation resistance at high temperatures, Si, aluminum (Al) and Cr are relevant, because they form the most protective oxide scales: alumina (Al_2O_3), silica (SiO_2) and chromia (Cr_2O_3). For an oxide scale to be protective, several criteria must be fulfilled. First, the oxide must be thermodynamically stable at a given temperature and under a specific oxygen partial pressure, which can be assessed using Ellingham-Richardson diagrams (Figure 1 a)). These diagrams indicate which oxide formation is energetically favored, and thus, which oxide(s) are stable under certain conditions. In addition, the oxide scale must be continuous, dense and adherent to the underlying substrate to effectively limit transport of oxygen and metal ions and to avoid spallation under thermal or mechanical loading. Finally, protectiveness requires slow oxide growth kinetics. This behavior is typically characterized by parabolic growth laws, assuming

diffusion-controlled oxidation, and can be evaluated using Arrhenius plots of the parabolic rate constants as a function of temperature (Figure 1 b)). Only oxide scales that combine thermodynamic stability with dense morphology, good adhesion, and low growth rates provide long-term environmental protection at high temperatures.

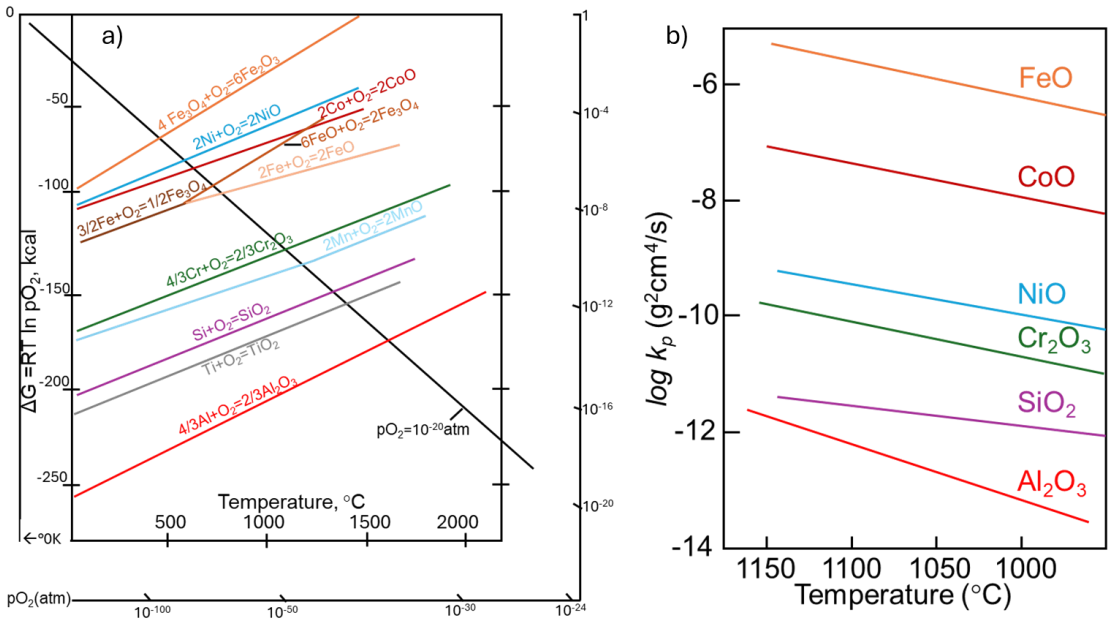

Figure 1: a) Thermodynamic- (Ellingham/Richardson diagram after [108]) and, b) Kinetic aspect of oxide growth (Arrhenius plot: Parabolic growth rates vs. temperature for common oxides after [110] with kind permission from Wiley).

While Cr is widely used in commercial high temperature alloys as an alloying element and oxide former, it is less known as a base material for high temperature alloys. The key issues that need solving before Cr can be used as a base material were summarized by Klopp in 1969: “(1) The protection of chromium from oxidation / nitridation-embrittlement; (2) Improvement in the intrinsic impact ductility of chromium alloys at low temperatures; and (3) further improvement in the high temperature strength of chromium” [22]. Thus, Cr-base alloys currently have limitations on both sides of the property profile. The stated challenges must be overcome to make use of the attractive intrinsic properties of Cr: high melting temperature (Cr: 1863-1907 °C vs. Ni: 1455 °C [36, 37, 38]) - which promises the possibility of high service temperatures -, low density (Cr: 7.14 g/cm^3 vs. Ni: 8.9 g/cm^3 [28]) enabling lower overall weights of components, high thermal conductivity (Cr: 94 W/m·K vs. Ni: 91 W/m·K [36]), wide availability (Cr: 41 vs. Ni:

3.6 million tons per year [27]) and low price (Cr: 10.000 vs. Ni: 23.000 $/ton [26])]. These benefits are the major drivers for ongoing research.

1.1.1 High temperature oxidation and nitridation of Cr and Cr alloys

For engineers, understanding the oxide growth kinetics of alloys is essential to determine if they can withstand the targeted service temperature and environment for an acceptable lifetime. As mentioned, in many alloys Cr is used as alloying element to improve oxidation resistance. The most stable oxide for Cr is chromium-(III)-oxide also called chromia (Cr_2O_3). Chromia-forming alloys are usually protected up to temperatures of 1000 °C. Up to 1000 °C, chromia scale formation can be described with the parabolic growth law [39]:

$$\frac{dx}{dt} = \frac{k_p}{x} \tag{1}$$

Formular 1 integrates into:

$$x^2 = 2k_P t \tag{2}$$

Where x is the oxide scale thickness, k_P is the parabolic growth rate and t is the isothermal exposure time. In practice, the weight gain per surface area of an exposed material is often used to determine the oxide growth kinetics for simplicity:

$$\frac{\Delta m}{A} = \sqrt{k_p t} \tag{3}$$

With Δm being the mass change and A being the exposed surface area. The first description and usage of these parabolic oxidation kinetics to describe oxidation of metals was published by Tammann in 1920 [40] and Pilling and Bedworth in 1923 [41]. Wagner was the first one to take into account the oxide properties for the description of the growth kinetics [42].

Parabolic oxidation kinetics describe a decreasing oxide growth rate over time for a protective oxide layer, because ions/vacancies and electrons/holes must diffuse through the already existing oxide layer before further oxidation of the metal substrate can take place. This theory assumes a diffusion-limited process and a perfectly adherent oxide scale without cracks. Since the diffusion rate is dependent on the temperature, the oxide growth rate, k_p, is also temperature

dependent and increases with increasing temperature (see also Figure 1 b)). This simplified description of scale growth behavior is especially accurate for pure metals or alloys forming a single protective oxide scale. Above 1000 °C other factors have to be taken into account for chromia formers which can strongly affect the oxide growth kinetics:

1. Volatility of oxides

Above 1000 °C, chromia will start to partly react to a volatile species, forming chromium-(VI)-oxide (CrO_3):

$$Cr_2O_3\,(s) + \frac{3}{2}O_2 \rightarrow 2CrO_3\,(g) \tag{4}$$

In order to describe the oxide growth rate accurately, as soon as volatility starts to take place, this loss of material has to be taken into account by including a linear volatilization rate, k_v [39, 43]:

$$\frac{dx}{dt} = \frac{k_p}{x} - k_v \tag{5}$$

Integrating this formula for the boundary condition x = 0 at t = 0 gives [43]:

$$t = \frac{k_p}{{k_v}^2}\left[-\frac{k_v}{k_p}x - \ln\left(1 - \frac{k_v}{k_p}x\right)\right] \tag{6}$$

In practice, thermogravimetric data is used to measure the oxidation kinetics of alloys and thus an adjusted formula can be used, as developed in ref. [44]. However, a simplified approximation to the formula stated in ref. [44] was applied by ref. [45] and successfully used to describe the oxide growth kinetics of Cr-Si alloys in ref. [30], using mass change per area instead of oxide thickness, taking into account the parabolic growth rate, k_P, and subtracting the linear volatilization rate, k_v:

$$\frac{\Delta m}{A} = \sqrt{k_P t} - k_v t \tag{7}$$

Figure 2 schematically depicts typical mass change curves of isothermally exposed metals over time. In the parabolic case, as stated above, the oxidation rate decreases with increasing exposure time. For exclusively volatile oxide formation (e.g. Mo rapidly forming MoO_3), linear mass loss can be observed. Whereas for paralinear kinetics, both processes, oxide growth (mass gain) and volatility (mass loss), occur at the same time and a steady state condition is reached eventually. However, it is crucial to understand that metallic material is still being lost at that stage. Often, this phenomenon is not sufficiently discussed in literature and therefore leads to wrong assumptions. The parabolic growth dominates the kinetics during short exposure times. The seemingly low mass change leads to wrong conclusions, if the formation of volatile species and paralinear law is neglected.

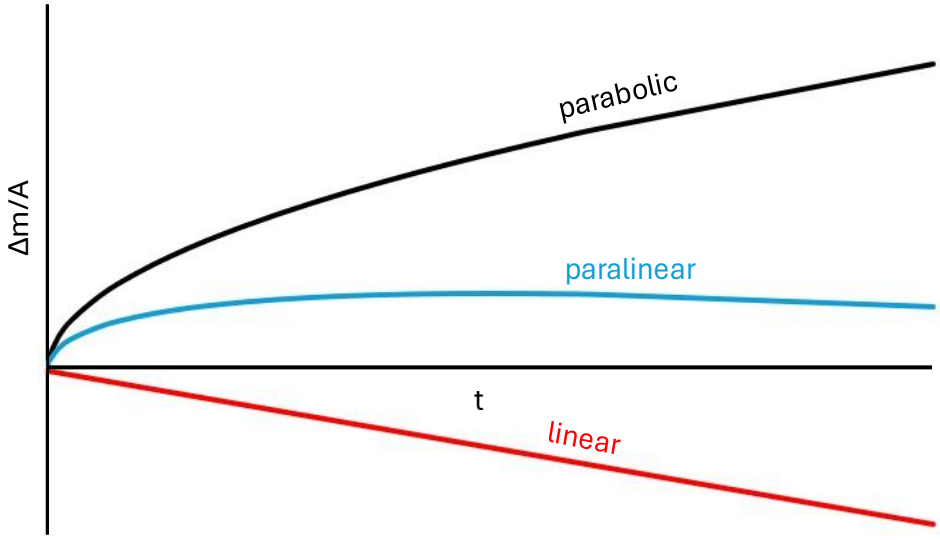

Figure 2: Schematic mass change per surface area versus isothermal oxidation time for the parabolic, paralinear and linear case.

2. Nitridation of Cr

Another aspect that will change the oxidation kinetics of chromia formers and especially Cr based alloys is that Cr tends to show strong nitridation when exposed to air at high temperatures, which happens especially quickly above 900 °C. The Cr-N phase diagram is depicted in Figure 3 after [46]. For temperatures above 900 °C, the Cr solid-solution (Cr_{ss}) starts to have some solubility for interstitial N. Dichromium nitride (Cr_2N) is the compound formed at high N partial pressures and high temperatures:

$$4Cr_{(s)} + N_{2(g)} \rightarrow 2Cr_2N_{(s)} \quad (8)$$

The second, N-richer compound, chromium nitride (CrN) is not stable for N partial pressures below 1 atm and temperatures above 1049 °C [25].

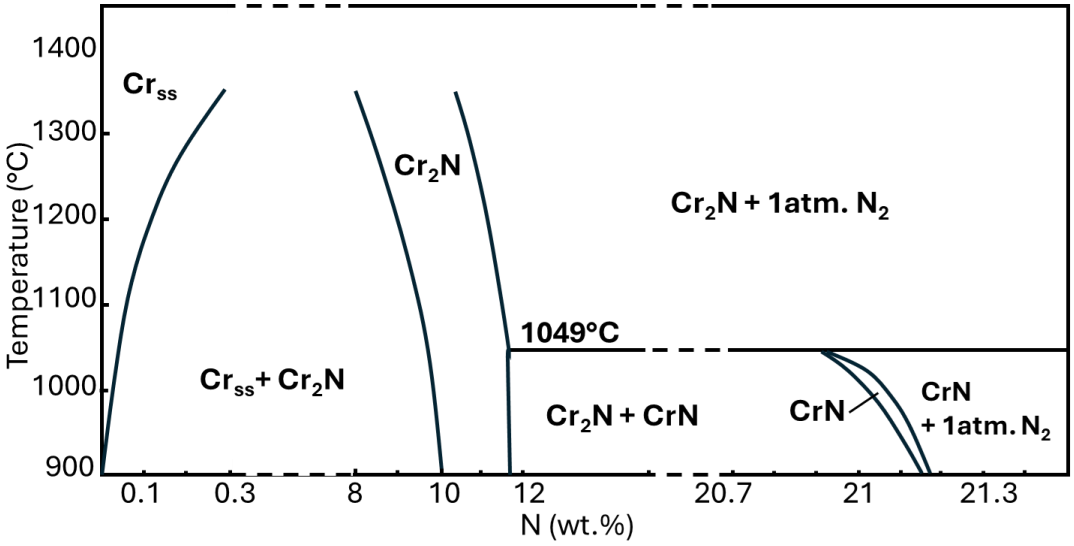

Figure 3: Cr-N phase diagram between 900 and 1350 °C after [46] (with kind permission of Elsevier).

As mentioned, Cr or Cr-based alloys exposed to air at temperatures >900 °C are observed to form a Cr_2N subscale beneath chromia, due to reduced oxygen partial pressure (pO_2) below chromia and higher nitrogen partial pressure (pN_2). If the oxide layer spalls off, or the pO_2 is increased in some other way, this would destabilize Cr_2N and lead to oxidation of Cr_2N to Cr_2O_3 [47]:

$$2Cr_2N_{(s)} + 3O_{2(g)} \rightarrow 2Cr_2O_{3(s)} + N_{2(g)} \quad (9)$$

Solimani et al. [48] showed that if initially a dense and continuous chromia layer is formed (during a pre-oxidation step at 1050 °C, excluding N_2), then subsequent exposure in pure N_2 does not result in Cr_2N subscale formation, which indicates that a uniform chromia scale can be a good barrier for nitrogen, and thus nitridation. However, if the subsequent exposure is performed in synthetic air (N_2/20%O_2) nitridation is observed and can be linked to further growth of chromia and opening up of transport paths for N_2 to the substrate material [48]. Since chromia scales are prone to wrinkling and cracking, as discussed in the next section, they cannot prevent nitridation of Cr-based materials in the targeted application case.

Nitridation of the substrate contributes to the overall mass change in addition to oxidation. As a result, the oxide growth kinetics of Cr-based alloys in air cannot be described using equations (3) and (7), since these formulations cannot differentiate between mass change induced by oxidation and mass change induced by nitridation. Cross-sectional analysis is required in addition to mass change data to identify the formed oxidation and corrosion products and to determine the overall metal loss. Nitrogen uptake and the associated formation of nitrides represent a key challenge for Cr-based materials [22], as they cause severe embrittlement. This effect arises not only from the formation of a thick Cr_2N subscale layer but also from nitrogen in solid solution and nitride phases precipitating within the bulk material, as discussed in detail in section 1.1.2.

3. Scale spallation

Thermogravimetric analysis (TGA) is used to monitor the mass change in situ during isothermal exposure and determine the oxidation kinetics of materials. For chromia forming on Cr, especially at high temperatures, and thus higher oxide growth rates, mass gain discontinuities are observed during TGA experiments [30]. This phenomenon is depicted in Figure 4.

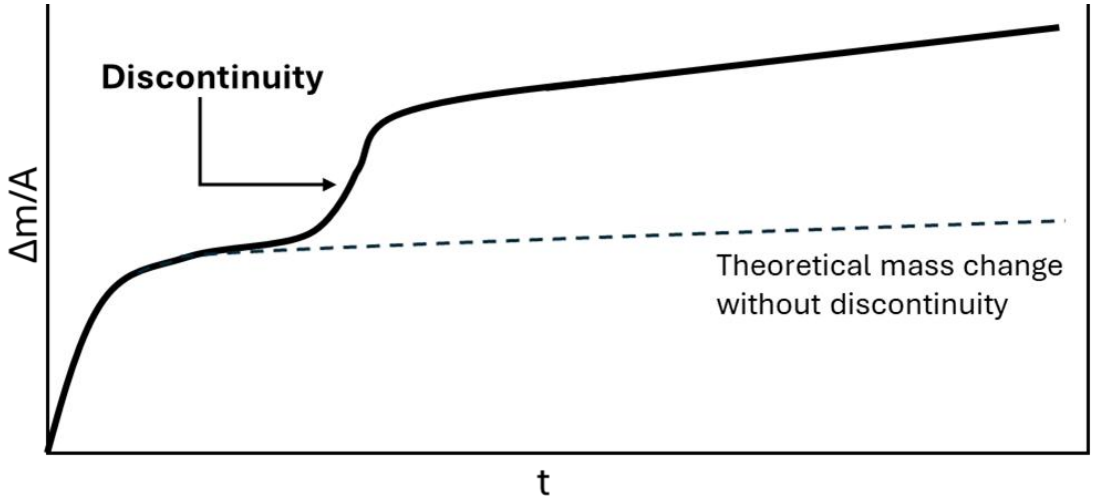

Figure 4: Schematic representation of discontinous mass change of chromia formers.

At the discontinuity a sharp rise in mass gain is observed followed by a decrease in growth rate over time. This behavior is linked to local oxide scale failure/spallation leading to exposed substrate material, which again forms a new chromia scale. Ulrich et al. [49] showed, in detail, how these discontinuities affect

the growth kinetics of Cr at high temperatures. Scale spallation during high temperature exposure is thus another obstacle during characterization of Cr oxide growth kinetics. The reason for spallation is discussed in the following. Cr is known to form protective/adherent chromia scales at intermediate temperatures (< 900 °C) for Fe-, Ni- or Co-based alloys containing approximately > 20wt.% Cr and is thus a popular alloying element to increase oxidation resistance. However the phenomenon of chromia spallation and buckling due to compressive stresses is frequently described in literature for high temperatures (≥ 900 °C), especially for chromia growing on pure Cr [50, 51, 52, 53, 54, 55, 56]. Determining the Pilling Bedworth ratio, R_{PB}, gives a good first indication, if a metal is capable of forming an adherent oxide layer during exposure in air. R_{PB} ratio is defined as [41]:

$$R_{PB} = \frac{V_{Oxide}}{n * V_{metal}} = \frac{M_{Oxide} * \rho_{metal}}{n \cdot M_{metal} * \rho_{Oxide}} \quad (10)$$

Where n is the number of metal atoms per molecule of the oxide, V is the molar volume, M is the atomic/molecular mass and ρ is the density.

For values smaller than one, no protective oxide layer can form on top of the metal. The oxide forms a porous non-protective oxide layer. This is, for example, the case for Mg forming MgO on Mg and Ca forming CaO on Ca. For values of 1-2, protective oxide layers can form. This is the case for Al forming Al_2O_3 on Al or Zn forming ZnO on Zn. For values higher than two, compressive stresses can lead to crack formation and spallation of the oxide, which can be the case for Fe forming Fe_2O_3 on Fe [57].

The R_{PB} for Cr forming Cr_2O_3 on Cr is only slightly above two (2.05 [57]) and thus it behaves protectively at intermediate temperatures in air. However, for temperatures ≥ 900 °C, on Cr (and also Cr-base material) the chromia scale is non-adherent and thus less protective, as shown by many groups [50, 51, 52, 53, 54, 55]. Other than e.g. insulating alumina (Al_2O_3), chromia is a semiconductor (E_g = 3.0-3.5 eV [54]) and able to allow n- or p-type conduction, which heavily influences its growth mechanism. Latu-Romain et al. [54, 55] confirmed in their investigation of chromia formation on pure Cr substrate at 900 °C, that the type of predominant point defects in chromia lead to different growth mechanisms. The types of point defects strongly depends on the pO_2. For high pO_2, p-type defects

are dominant, meaning that Cr^{3+}-cation vacancies are forming in the chromia structure and enable outward cation diffusion. This type of mechanism leads to outward growing columnar chromia grains at the oxide/gas interface. For lower pO_2, an n-type dominated defect structure forms, containing O^{2-}-anion vacancies and enabling O^{2-} inward diffusion leading to rather dense, equiaxed, strained inward growth of chromia at the oxide/metal interface. Latu-Romain et al. [54, 55] showed that on pure Cr, chromia does in fact show both growth types and forms an oxide scale with a duplex morphology. From an initial chromia layer a columnar p-type chromia scale is formed on top, and, beneath the initial scale, equiaxed n-type chromia is observed. Diffusion of ions is not only happening through the described vacancies but also along the grain boundaries [57]. Here, both anion and cation diffusion can take place. This enables the formation of new oxide within the scale and leads to crack formation and spallation [57]. Additionally, after isothermal exposure in synthetic air, spallation of chromia is often observed after cooling and located between the p- and n-type chromia layers, as described in ref. [55]. This mechanism is thus decreasing the protectiveness of chromia scales on Cr during high temperature oxidation and remains to be studied for Cr-based alloys.

1.1.2 Mechanical characteristics of Cr and Cr alloys

While designing a structural material for high temperature application, especially balancing out the necessary mechanical properties of an alloy is challenging. Key properties for turbine applications are: low temperature ductility, fracture toughness, high temperature strength, creep and fatigue resistance. Unfortunately, increasing high temperature strength often is coupled to a decrease in the low temperature ductility. Compromise is necessary to develop an alloy for high temperature applications that can perform reasonably under the targeted service temperatures (>1100°C).

Pure metals are typically not strong enough at elevated temperatures and are especially prone to creep (time-dependent deformation under constant stress). Strengthening mechanisms are therefore an indispensable tool.

In general, usual strengthening methods are directed either towards the microstructure or composition of an alloy. Microstructure wise strengthening via

cold working, which implements a high density of dislocations (line defects in the crystal lattice) into the material that form obstacles for further dislocation motion, can be applied [58]. In grain boundary strengthening the increased number of grain boundaries act as a barrier for dislocation motion, strengthening the material. However, neither of these methods is suitable for materials which are designed to operate at temperatures greater than 40% of their melting temperature ($0.4 \cdot T_m$) [58]. In that temperature range, dislocations, implemented by cold working, recover and a smaller grain size is detrimental for creep resistance, because the large amount of grain boundaries promote faster diffusion and grain boundary sliding [58].

Thus, for high temperature applications, strengthening by altering the composition of the alloy is the only relevant one. Solid solution strengthening and precipitation or particle strengthening are mechanisms to retain strength at elevated service temperatures. Solid solution strengthening is the method of introducing foreign atoms to the base metal crystal structure. A certain solubility of the foreign atom is required either as substitutional atom (for similar atomic radii) or as interstitial atoms. Introducing these foreign atoms leads to a distorted host lattice. Dislocations now must move around the lattice distortion, which requires more energy, and thus increases the strength of the material. Another possibility to pin or hinder dislocation motion is through precipitation of a second thermodynamically stable phase (for example γ’ and/or γ’’ in Ni-based superalloys [11]) or introduction of particles like carbides, nitrides, or oxide dispersoids. Usually, single phase materials that are only strengthened via solid solution strengthening are not considered suitable as structural high temperature materials (>1000 °C) and additional second phase/particle strengthening is essential for reasonable creep resistance [59].

Designing a Cr-based high temperature alloy will require solid solution strengthening and some form of second phase strengthening. These strengthening mechanisms will benefit the alloy in the high temperature regime in terms of strength and creep resistance, but often worsen the already low ductility and fracture toughness at low temperatures; a known problem of body centered cubic (BCC) metals.

The disadvantage of the ‘open’ BCC crystal structure of Cr, when comparing it to Ni with its close-packed face centered cubic (FCC) crystal structure (see Figure 5), is not only the higher self-diffusion rates, and a resulting lower creep resistance for the same homologous temperature (ratio of a material's absolute temperature to its melting temperature in Kelvin) compared to Ni [22], but also the significantly lower ability for plastic deformation at low temperatures. For plastic deformation to occur, dislocation motion is necessary. Dislocations allow planes of atoms to slip past each other, which is a mechanism that controls the overall mechanical response of a crystalline material [60]. Two idealized types of line defects are fundamental: The edge dislocation and the screw dislocation. In FCC structures, edge as well as screw dislocation glide occurs primarily on the planes that are close-packed, because here the energy barrier, or critical resolved shear stress (CRSS) [which is the minimum shear stress required on a slip system to initiate dislocation motion in a crystal], for dislocation motion in minimized. Also screw dislocations in FCC metals can change from one slip plane

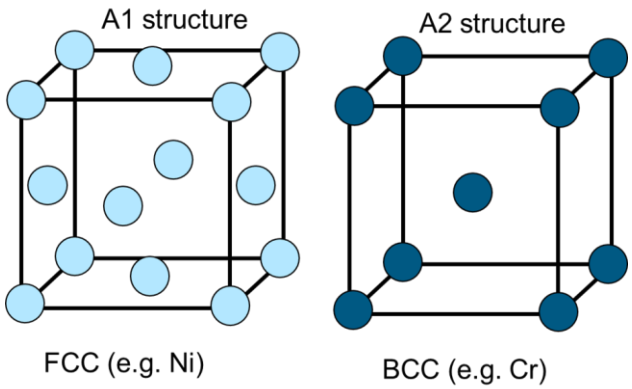

Figure 5: Unit cell of FCC and BCC crystal structure.

to another which is called cross-slip [60].

Apart from these dominant deformation mechanisms, another possible deformation type is called twinning. If twins are formed, a portion of a crystal undergoes a coordinated shear, so that its lattice becomes a mirror image of the parent lattice across a specific twin plane [60]. The process reorients the crystal locally, rather than producing simple shear as in dislocation slip. Twinning therefore changes the texture (grain orientation pattern) and can activate new slip systems by lattice reorientation [60]. Usually, it only occurs at low temperatures,

very high strain rates, or in materials with limited slip systems and thus high lattice resistance to dislocation motion [60, 61].

Stacking fault energy (SFE) further differentiates BCC and FCC metals. Stacking fault energy is defined as the energy per unit area required to separate partial dislocations and create a stacking fault, which is a local deviation from the ideal stacking sequence of close-packed planes [60]. FCC metals typically have moderate to high stacking fault energies, which stabilizes mobile dislocations and facilitates cross-slip [60]. This promotes a more homogeneous distribution of plastic strain and reduces the likelihood of strain localization. As a consequence, the FCC crystal structure is able to distribute strain uniformly and continuously and thus shows rather high deformability, which is mostly independent of temperature [61]. Twinning is favored for low SFE, because low SFE stabilizes partial dislocations and stacking faults, making the sequential partial dislocation motion required for twinning energetically favorable [60].

BCC metals do not have close-packed slip planes and do not form intrinsic stacking faults in the same way as FCC materials. Even though BCC crystals possess more theoretically available slip systems, their effectiveness is limited by the high energy that is necessary to move screw dislocations through the lattice, whereas edge dislocations are rather mobile [62]. The Peierls barrier, which is the energy barrier that a dislocation must overcome to move from one stable lattice position to the next, is high for screw dislocations in the BCC lattice, meaning that dislocations are strongly pinned by the lattice and require significant thermal activation to move. As a result, dislocation motion in BCC metals is highly temperature dependent [61].

Figure 6 illustrates the impact strength of BCC and FCC materials as a function of temperature. While the impact strength of FCC materials is almost temperature-independent, there is a clear transition observed for BCC materials. At lower temperatures, the impact strength is low, and fracture is characterized as brittle; the favorable ductile fracture is limited to higher temperatures areas. At intermediate temperatures, a mixed fracture is usually observed, which is the location of the so-called ductile to brittle transition temperature (DBTT).

It follows that for BCC metals like Cr, it is complicated to increase strength and creep resistance at high temperatures without further decreasing already low plasticity at lower temperatures.

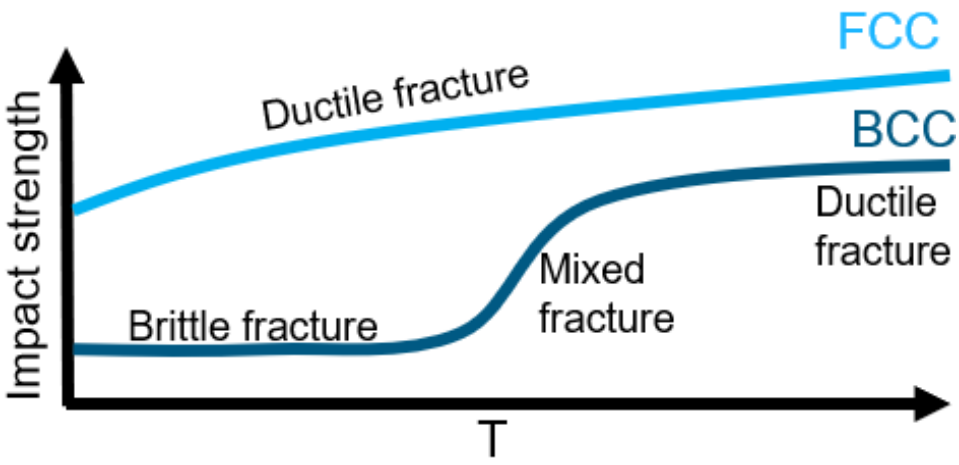

Figure 6: Impact strength vs. temperature for FCC and BCC materials after [61].

However, the drive to go beyond the service temperature of Ni-based material motivates tackling this challenge, since all more affordable refractory metals, that are potential base materials for a high temperature alloy, are BCC metals.
The DBTT of commercially pure Cr is usually around 150 °C [63], while ultra-pure Cr can have a DBTT of - 45 °C [64]. Nitrogen was identified as a major impurity contributing to the increase of the DBTT, while sulfur (S) as well as oxygen (O) did not contribute as significantly [22, 63, 65, 66, 67]. Figure 7 depicts the influence of the nitrogen level, manufacturing and cooling method on the DBTT of Cr. The presented data clearly shows an increase in the DBTT for Cr with increasing N content. It also reveals that the manufacturing method and the cooling rate play a key role [68, 69]. For high cooling rates, the DBTT rises sharply. Actually it is not N trapped in the solid solution upon quenching that is the embrittling factor, but rather nitrides that form during cooling [22, 63, 65]. Fast cooling leads to the formation of fine, intragranular, needle-like precipitates on preferred crystallographic planes (dislocation lines) and increases the DBTT [22, 63, 65]. Slow cooling rates enable the formation of larger nitrides, which are not as detrimental.

Apart from processing, alloying can influence the DBTT of Cr. Especially cerium (Ce), Ti, yttrium (Y) and zirconium (Zr), used as scavenging elements, e.g for nitrogen, can improve the low temperature ductility of Cr [70, 63]. In [64] the influence on the DBTT of 25 elements, each alloyed to Cr with up to 3 wt.%, was

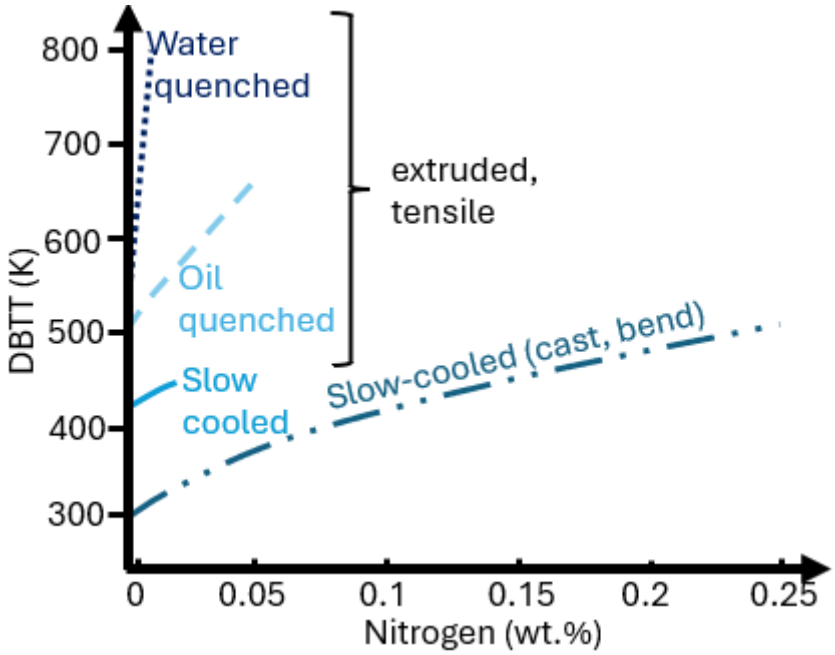

Figure 7: Influence of the nitrogen level, manufacturing, and cooling method on the DBTT of Cr after [22] with data from [67, 66] (with kind permission of Springer Nature).

investigated. The key finding was that: “The brittle-ductile transition temperature of high purity chromium is decreased by the addition of elements which are in solid solution and have an atomic diameter larger than that of chromium but not exceeding the 15% size limit” [64]. This is the case for e.g. Mo and vanadium (V), when added as minor alloying additions up to a few percent. Y, Zr and Ti were stated as elements increasing the DBTT in this study [64], so the available literature is partly contradictory in this respect. The addition of high amounts (> 25 at.%) of rhenium (Re), cobalt (Co), ruthenium (Ru) and iron (Fe) were shown to decrease the DBTT of Cr as well, utilizing the so called “Rhenium-Ductilizing Effect”. This effect is attributed to a change in the deformation mode of Cr, specifically through the activation of twinning, as discussed in several studies [71, 72, 73].

Production and testing of several Cr-based alloys started in the 1950s in Australia, the USA and the Soviet Union [22]. In the 1960s, turbine blades

produced from the Australian chromium alloys [Cr-2Ta-0.5Si+0.1Ti+0.5RE (rare earth element)] showed good creep resistance in a rig, however, they failed impact testing by showing fracture at the colder roots of the blades, which was possibly due to the high DBTT of the tested alloy or due to nitridation [22]. This example shows that preferably the DBTT of a structural material should be as low as possible. However, γ-TiAl alloys, which made it into the low-pressure turbine (LPT) as blades and vanes in gas turbine engines, have a DBTT in the range of 650 to 820 °C and fracture toughness between 10-33 $MPa \cdot m^{0.5}$ [22, 61, 63] depending on the exact composition and microstructure [74]. That shows that higher DBTTs do not exclude materials from structural applications in general, and as long as a certain fracture toughness threshold (stated to be above 15 $MPa \cdot m^{0.5}$ [75]) is maintained, engine designers can start using the material.
Strengthening Cr utilizing solid-solution can lead up to a sevenfold increase in strength [63], but large amounts of solid solution strengtheners will lead to an increase in the DBTT. In the high temperature regime, precipitate and particle strengthening is more effective in order to limit the amount of necessary solid solution strengthening and thus limit the increase of DBTT [22, 63]. In the 1960s, Scruggs [76] developed a Cr-based alloy incorporating MgO particles (with the composition Cr-6MgO-0.5wt.%Ti according to [22]) using a powder metallurgical route. This alloy showed a surprisingly high ductility at room temperature (RT) with 8% tensile elongation before fracture. In 2003, Brady et al. [77] revisited this work and achieved 10% tensile elongation at RT for hot-pressed and extruded Cr-6MgO-0.75wt.%Ti. It was observed that nitrogen segregated to interfaces between the MgO and the formed spinel $MgCr_2O_4$, likely reduced the detrimental effect of intragranular fine nitride precipitates [77].

1.2 The Cr-rich Cr-Mo-Si system (A2 + A15 approach)

In the 1990s, the development of intermetallic alloys, which retain their strength up to very high application temperatures (>1100 °C), received great interest. Since alumina- and silica-forming alloys provide especially protective oxides, aluminides and silicides got much attention. For the aluminides, TiAl seemed most promising. For the silicides, Mo-based systems were focused on, additionally Cr_3Si was intensively investigated [29]. The initial focus was put on

properties like inherently high creep resistance, low density, high oxidation resistance at high temperatures and high thermal conductivity [29]. The discussion or improvement of plasticity at lower temperatures was not prioritized at that time. Eventually, in order to increase plasticity for the Cr_3Si intermetallic, the A2-Cr matrix was added to the system, resulting in Cr + Cr_3Si alloys. In the 1990s, mostly the Cr_3Si-rich part of the system was investigated [29, 78, 75], but the absence of plasticity at low temperatures demanded either strictly limiting the amount of Cr_3Si (A15) or modifying the microstructure to generate some deformability. With the more recent incorporation of Cr as the matrix phase, the challenge of nitridation became relevant again [30] and made it necessary to find suitable alloying additions to the Cr + Cr_3Si system. Mo turned out to be especially beneficial, increasing not only the resistance against nitridation but also the creep resistance of the alloys [33, 79, 32] and thus became a relevant alloying addition to the system.

1.2.1 Binary Cr-Si alloys

The latest Cr-Si phase diagram by Ioroi et al. [38] is depicted in Figure 8. Besides the solid solutions of Cr and Si, it contains four intermetallic compounds Cr_3Si, Cr_5Si_3, CrSi, $CrSi_2$, which are listed in Table I. For structural materials, the Cr-rich

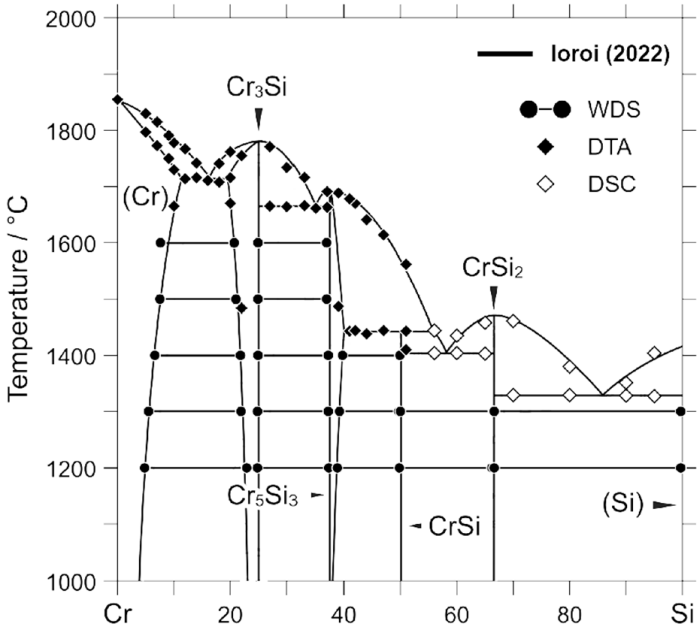

Figure 8: Latest Cr-Si phase diagram after Ioroi et al. [38] (with kind permission of Springer Nature).

part of the phase diagram seems most promising, which is the two-phase region of the Cr solid solution and the Cr_3Si intermetallic phase. At 1200 °C, 4.8 at.% [38] Si is soluble in the Cr solid solution. The addition of more Si leads to the formation of the Cr_3Si intermetallic. Eutectic solidification of the liquid to the Cr + Cr_3Si phases occurs at about 15 at.% Si and at 1705 °C, leading to a fine lamellar microstructure of Cr and Cr_3Si.

Table I: Phases in the Cr-Si system after [38].

Phase	System	Prototype	Strukturbericht
(Cr)	Cubic	W	A2
Cr_3Si	Cubic	Cr_3Si	A15
Cr_5Si_3	Tetragonal	W_5Si_3	D8m
CrSi	Cubic	FeSi	B20
$CrSi_2$	Hexagonal	$CrSi_2$	C40
(Si)	(Diamond) Cubic	C	A4

The A15 crystal structure of Cr_3Si is depicted in Figure 9. The Cr-Si phase diagram, shows that the solubility of Si in Cr solid solution is increasing with increasing temperature, meaning it is possible to apply a precipitation hardening heat treatment for Cr-Cr_3Si alloys. The goal of such a heat treatment is to apply a high temperature homogenization step, aiming for full dissolution of Si in the Cr matrix. A second step at lower temperature, and thus reduced Si solubility, leads to precipitation of finely and uniformly distributed intermetallic Cr_3Si phase.

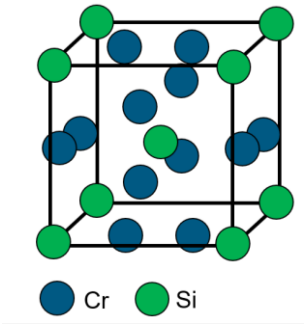

Figure 9: Cubic A15 crystal structure of Cr_3Si.

However, the solvus line of the phase boundary between Cr and Cr-Cr_3Si field is rather steep, so high temperatures are necessary in the first heat treatment step, which is not ideal in terms of energy efficiency of the process and also can lead

to large grain sizes and high volatilization rates of Cr due to its high vapor pressure [80].

Soleimani-Dorcheh et al. [30] investigated the high-temperature oxidation and nitridation behavior of pure chromium and several arc-melted Cr-Si alloys: single-phase solid solution Cr(Si), two-phase Cr-Cr_3Si alloys and single phase Cr_3Si silicide were exposed in synthetic air at 1200 °C for up to 1000 h. All alloys were chromia formers [30]. It was observed that, adding Si to Cr strongly improved the oxidation resistance and slowed down Cr_2N formation [30]. Single-phase Cr_3Si material was highly stable and did not show nitridation [30]. Upon formation of chromia, the single phase material Cr_3Si became Cr-depleted and Cr_5Si_3 was stabilized at the alloy interface [30]. This Si-rich phase was able to form a protective SiO_2 layer beneath the chromia layer [30]. In the Cr-Cr_3Si eutectic alloy, Cr solid solution was selectively oxidized, creating an A15 layer beneath the oxide that blocked nitrogen uptake and protected the alloy from nitridation [30]. All alloys suffered from oxide scale spallation, but Si additions reduced this effect [30]. Using equation (7) Soleimani-Dorcheh et al. [30] analyzed the acquired TGA data (Figure 10) after 100 h of exposure at 1200 °C. The results

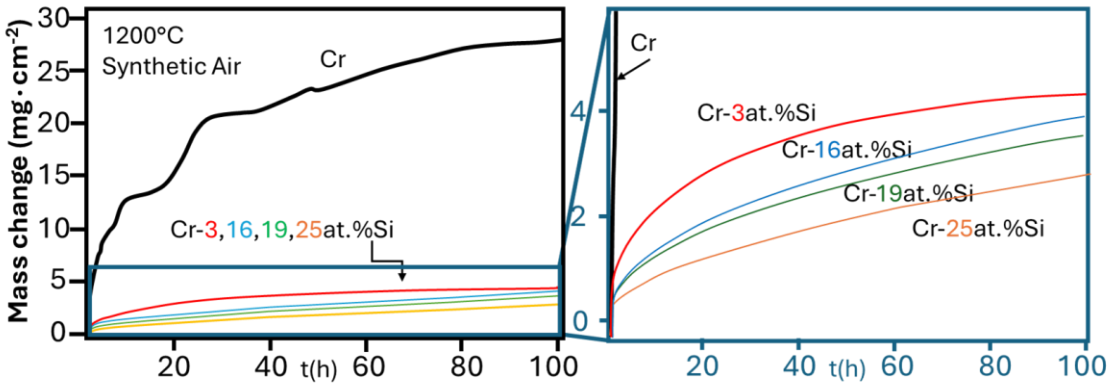

Figure 10: Mass change of Cr and Cr-Si alloys exposed at 1200 °C in synthetic air for 100 h after [30] (with kind permission form Springer Nature).

showed that increasing the Si content in Cr based alloys leads to a decrease in the parabolic growth rate k_p ($5.6 \cdot 10^{-9}$ and $3.0 \cdot 10^{-11}$ g^2/cm^4s for pure Cr vs. Cr-25 at.%Si [30]), and a decrease in volatilization rate k_v ($4.7 \cdot 10^{-8}$ and $8.6 \cdot 10^{-10}$ g/cm^2s for pure Cr vs. Cr-25 at.%Si [30]). The underlying reasons for reduced volatilization could not be resolved and need further investigation. Aono et al. [31] studied the mechanical properties of induction melted Cr-Si alloys, annealed at

1400 °C for 24 h and slowly cooled. Si contents between 0 and 16 at.% were tested under compression [31]. Before that all samples were annealed at 1400 °C for 24 h and slowly cooled. The results showed that the 0.2% proof stress at 1000 °C increased with Si content (which is accompanied with an increased fraction of A15) up to 15 at.%, with a pronounced improvement between 10-13 at.% (Figure 11 a)) [31]. Higher Si contents led to dominant brittle fracture before deformation was observed [31]. Aono et al. [31] also stated that the Cr-13 at.%Si alloy combined excellent high-temperature strength with good ductility at 1000 °C, but its ductility below 400 °C needs improvement, suggesting that

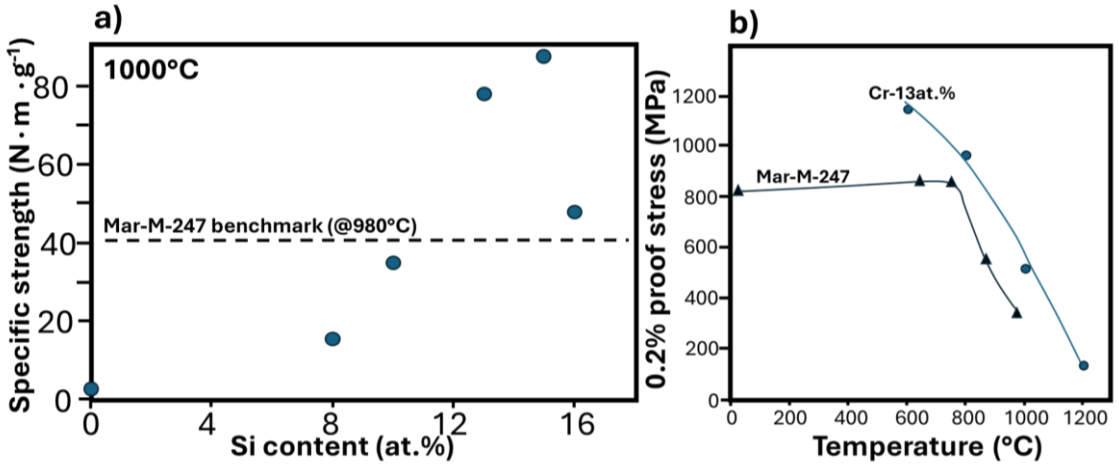

Figure 11: a) Specific strength of Cr-Si alloys with increasing Si content; b) Proof stress vs. temperature of Cr-13 at.% and Ni-based superalloy MAR-M-247 after [31] (with kind permission from Elsevier).

the DBTT for Cr-13 at.%Si is around 400 °C [31]. Compared to the Ni-based superalloy MAR-M-247, the Cr-13 at.%Si alloy has higher high-temperature strength and lower density (6.68 g·cm^{-3}), resulting in a specific strength of 78 N·m·g^{-1}, which is twice as high as MAR-M-247 (Figure 11 b)).

Thus, additions of Si to Cr have beneficial effects on the oxidation resistance, the nitridation resistance and the high temperature strength. But the studies also show it is relevant to find a balance between the benefits that the intermetallic phase can provide for the system and the disadvantages it can pose if the phase fraction is too large.

1.2.2 Cr-Mo-Si alloys

The phase diagrams of Cr-Mo and Mo-Si are depicted in Figure 12 after ref. [81] and [82]. Cr and Mo have complete mutual miscibility in the solid state. This means they form a continuous solid solution across the entire composition range. Both elements have the same BCC crystal structure and very similar atomic sizes with a difference of ~ 10% [64]. As a result, no stable intermetallic compounds form between them. The Cr-Mo phase diagram depicted in Figure 12 a) therefore shows full solid-state miscibility. Therefore, Cr and Mo can substitute one another

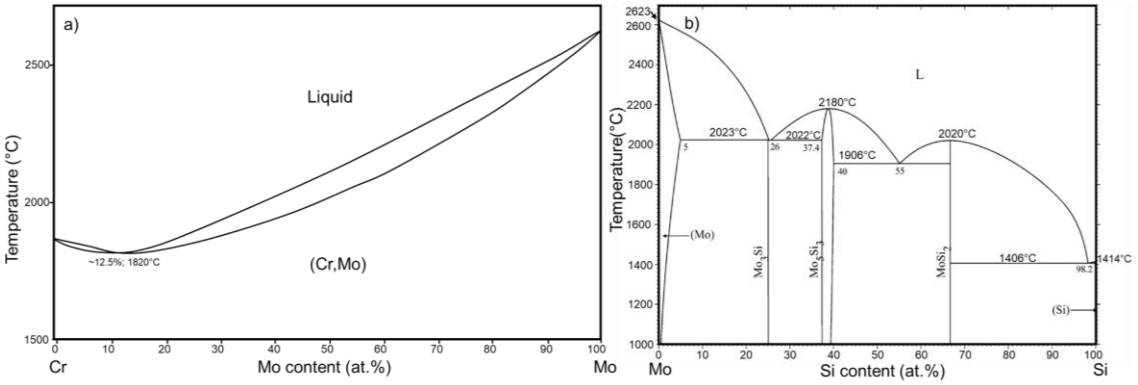

Figure 12: a) Cr-Mo phase diagram and b) Mo-Si phase diagram after [81] and [82] (with kind permission from Springer Nature).

in many alloys. Both are commonly used in steels and superalloys to enhance high-temperature strength (Mo) and oxidation resistance (Cr). Simulations suggest the existence of a miscibility gap at lower temperatures of around 880 °C for Mo content of 39 at.% [81]. Surprisingly, the experimental proof of the miscibility gap is lacking, due to the low diffusion rates at that temperature [81].

Mo does not form protective oxides at high temperatures, since it tends to form the volatile oxide MoO_3 (>700 °C) [21], which leads to the so called ‘pesting’ phenomena, describing catastrophic disintegration of the metal. However, when Mo is combined with Si, e.g. in Mo-Si or $MoSi_2$-based alloys, oxidation behavior changes significantly [21]. Silicon oxidizes preferentially to form a dense, continuous SiO_2 layer, which acts as a protective diffusion barrier. This SiO_2 scale limits oxygen ingress and suppresses further formation and volatilization of MoO_3, thereby reducing or preventing ‘pesting’ [21].

Figure 12 b) shows the Mo-Si phase diagram, which has similarities with the Cr-Si phase diagram (Figure 8), especially in the Mo-rich/Cr-rich part. After the

maximum solubility of Si is reached in the solid solution, the intermetallic A15 phase (Cr_3Si / Mo_3Si) forms. For Mo the Si solubility is lower than for Cr, and is around 1.5 at.% at 1200 °C. Another difference is that the Mo_3Si phase is a line compound in the Mo-Si phase diagram, exhibiting a nearly fixed stoichiometry, whereas the Cr_3Si phase field permits some deviation from the ideal 3:1 composition.

The ternary phase diagram of Cr-Si-Mo was published in ref. [83] and more recently investigated in Refs. [84, 85] and is depicted in Figure 13. Note that in ref. [83] the A15 phase $(Mo_xCr_{1-x})_3Si$ was incorrectly described as $(Mo_xCr_{1-x})_3Si_3$ in the diagram; this error was corrected for Figure 13. Also, the data for the σ phase (see section 1.2.3) was extracted from [86] but named τ_1 in ref. [83], which was changed here to σ for consistency.

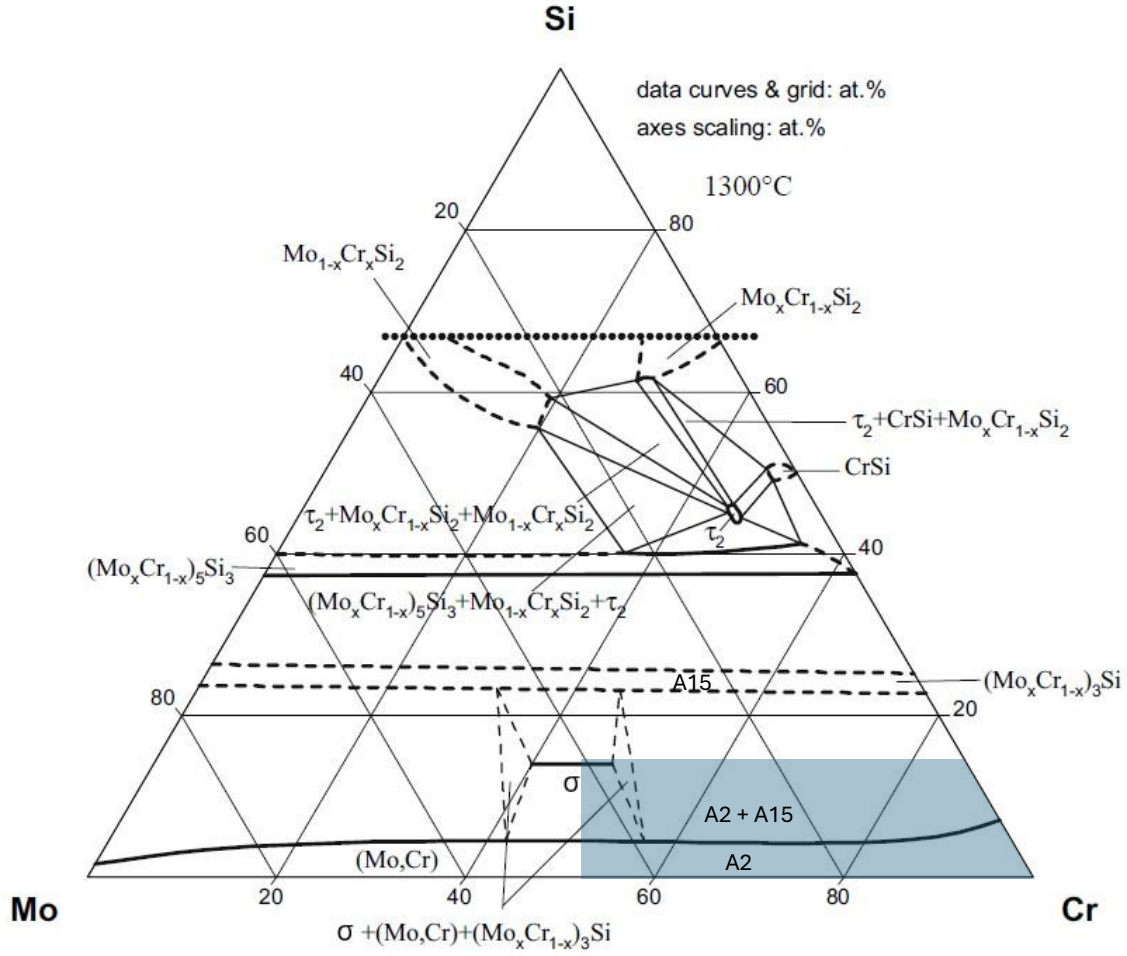

Figure 13: Ternary Cr-Mo-Si phase diagram (1300 °C) after [83] with an additional shaded area in the lower right corner highlighting compositional regime of interest for this work (with kind permission of Springer).

In 1995 Raj et al. [29], investigated a Cr-30Mo-30 at.%Si alloy forming a two-phase microstructure consisting of $(Cr,Mo)_3Si$ and $(Cr,Mo)_5Si_3$ designed for aircraft engine components and exposed it to high-velocity combustion gases in a burner rig test. During oxidation tests at 1100-1200 °C, the alloy formed a protective chromia layer at low temperatures and α-cristobalite (SiO_2) at high temperatures [29]. Raj et al. [29] suggested that adding molybdenum resulted in increased oxide volatility, allowing a silicon-rich surface to form and then oxidize at high temperatures. The arc-melted alloy had a compressive strength of 600 MPa at 1223 °C [29]. Burner rigs tests suggest a life of over 100 cycles at 1200 °C [29]. However, the fully intermetallic alloy exhibited a very high DBTT of around 1223 °C [29]. Fracture toughness was very poor with only 2-3 $MPa \cdot m^{0.5}$, making the alloy irrelevant for structural applications, but interesting as erosion- and oxidation-resistant coatings on turbine airfoils [29].

An alloy with lower Si content (Raj et al. [29]: Cr-30Mo-30 at.%Si) was reported by Hinrichs et al. [34] in 2022, testing the composition of Cr-32.2Mo-13.5 at.%Si. In the arc-melted state, this alloy was stated to be monolithic σ phase, which, upon annealing at 1200 °C showed eutectoid decomposition to a fine lamellar A2 + A15 microstructure [34]. The alloy showed promising oxidation behavior in air at 800 °C (no ’pesting’ observed) and reasonable oxidation resistance at 1100 °C. At 1200 °C, mass loss was evident after 40 h of exposure [34]. The samples were exposed for 100 h in total and cycled without spallation of the oxide [34]. SiO_2 formation beneath chromia was observed predominantly on the A15 phase, but also occurred on top of the A2 phase, forming a continuous film [34]. No nitridation of the A2 phase was observed [34].

These observations suggest that Mo protects the Cr A2 from nitridation and also has a beneficial effect on the adherence of the oxide scale, since the eutectoid binary Cr-16 at.%Si alloy investigated in ref. [30] did show nitridation and spallation during similar exposure. Hinrichs et al. [34] does not mention the mechanical properties of the alloy, but concludes that less Si could still lead to good oxidation resistance, while at the same time increasing the amount of A2 phase could improve ductility.

Earlier than that between 2018-2020, lower amounts of Mo and Si were studied by Ulrich and Pfizenmaier et al. [32, 33, 79]. In their studies, a Cr-2Mo-8Si at.%

alloy was developed, to produce a precipitation strengthened A2-A15 alloy with a high fraction of the A2 matrix phase. Ulrich et al. [32, 79] state that Mo partitioned homogeneously between the Cr solid solution (Cr_{ss}) and the A15 (Cr_3Si) phase in Cr-2Mo-8Si at.% alloy, and Mo refined the A15 precipitates. During oxidation at 1200 °C in synthetic air, Cr-2Mo-8Si at.% exhibited a reduced parabolic oxidation rate constant compared to binary Cr-Si alloys, indicating slower oxide growth [32, 79]. Mo promoted the formation of a thin, continuous SiO_2 layer at the metal/oxide interface, which acted as an effective diffusion barrier and contributed to a slightly reduced overall oxide scale thickness [32, 79]. The resulting Cr_2O_3 scale was characterized by fine, equiaxed grains, consistent with predominantly inward-growing (n-type) chromia [32, 79]. In addition, Mo strongly suppressed nitridation: the formation of Cr_2N was significantly reduced, and a Mo-enriched Cr_{ss} subsurface layer with ca. 5 at.% Mo developed that seemed resistant to nitrogen uptake [32, 79]. However the matrix beneath this region, containing only 2 at.% Mo, still showed nitridation (see Figure 14) [32, 79].

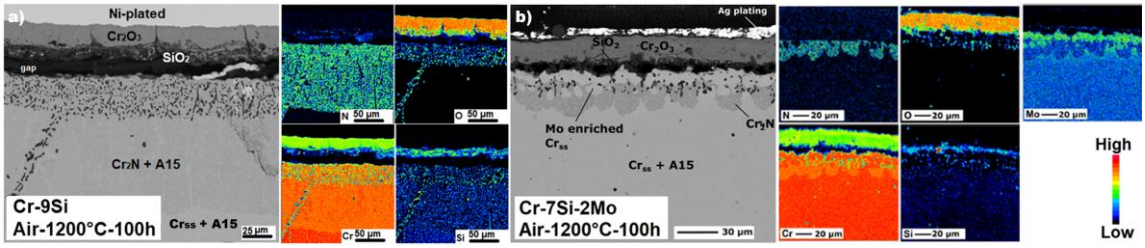

Figure 14: Cross secion and elemental distribution mapping of Cr-Si(-Mo) alloys after exposure in air for 100 h at 1200 °C a) Cr-9 at%Si b) Cr-7Si-2 at%Mo after [109]

Pfizenmaier [33] et al. tested the creep properties of the Cr-2Mo-8Si at.% alloy and compared it to the reference material Cr-9 at.%. From these studies, it was seen that the addition of 2 at.% Mo had a strong beneficial effect on tensile creep behavior at 980 °C in air (Figure 15) [33]. During the experiments, the addition of Mo significantly increased the resistance to environmental degradation by limiting nitrogen uptake during long-term exposure in air, thereby delaying nitridation-induced embrittlement [33].

More recently, Hinrichs et al. [35] studied the deformation mechanisms in single phase A2 material with the compositions of Cr-37.2Mo and Cr-36.1Mo-3Si (at.%). The alloys were produced by arc melting and examined in the as-cast condition,

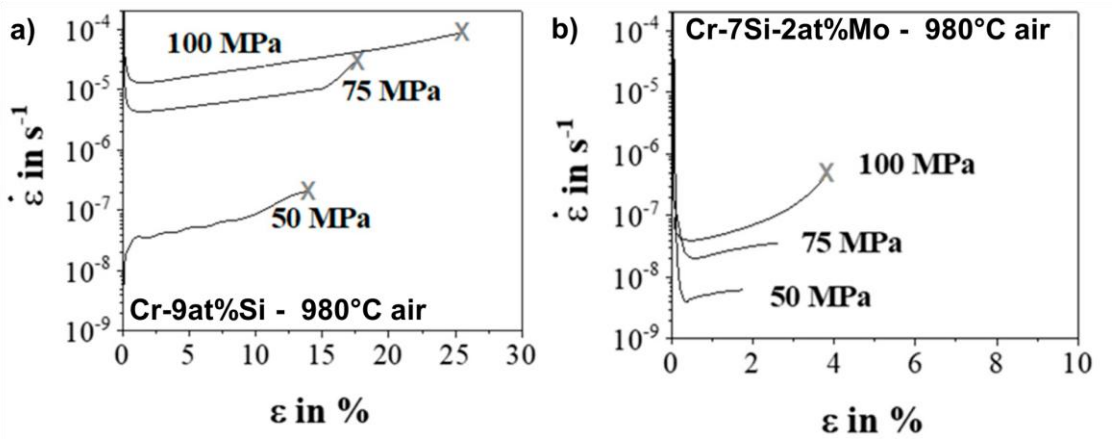

Figure 15: Creep rate vs. strain in air at 980 °C in air of a) Cr-9 at%Si b) Cr-7Si-2 at%Mo after [33]

with Cr-36.1Mo-3Si additionally homogenized at 1600 °C for 48 h [35]. Oxidation behavior was assessed by cyclic oxidation in air at 800 °C and 1100 °C for up to 100 h [35]. The Si-free Cr-37.2Mo alloy showed continuous mass loss at 800 °C due to MoO_3 evaporation and formed a porous, non-protective oxide scale, while at 1100 °C it suffered rapid mass loss and disintegration [35]. In contrast, Cr-36.1Mo-3Si exhibited negligible mass change at 800 °C and remained intact at 1100 °C [35]. Microscopy and atom probe tomography revealed a thin, continuous Cr_2O_3 scale, a Mo-enriched subsurface region as described in [32], and SiO_2 near the scale-substrate interface.

Mechanical behavior was investigated by compression testing from room temperature up to 900 °C [35]. Both alloys showed high strength and measurable plasticity at room temperature, with Cr-36.1Mo-3Si reaching 6% compressive strain in the annealed state [35]. Yield strength remained high up to 700 °C, forming a broad strength plateau, and at 900 °C, approximately 70% of the room-temperature strength was retained [35]. Deformation was serrated at all temperatures, reflecting discontinuous plastic flow [35]. Post-deformation EBSD analyses showed that plasticity occurred by a combination of dislocation slip and deformation twinning [35]. Twinning was prominent at room temperature, persisted up to 900 °C, and was more dominant in coarse-grained material, contributing to high work-hardening rates but also to localized cracking along twin and grain boundaries [35]. Overall, the tests demonstrated that a single-phase Cr-36.1Mo-3Si solid solution exhibits stable oxidation behavior up to 1100 °C with high strength and room-temperature plasticity [35]. However, particle and/or

second phase strengthening remains necessary for high creep resistance of these alloys at temperatures >1100 °C.

1.2.3 The σ phase in the Cr-Mo-Si system

In multicomponent alloy systems, most commonly found in Fe-, Cr-, Mo-, and Ni-based alloys, σ phases can be present. The designation “sigma phase” originates from early X-ray diffraction studies in the 1930s [87], where unidentified complex phases in Fe-Cr alloys were labeled sequentially with Greek letters. The σ phase designation persisted even after its structure was resolved. The σ phase has a complex tetragonal crystal structure with space group $P4_2/mnm$ and is a topologically close-packed (TCP) phase. It belongs to the class of intermetallic phases, but usually allows for a large compositional variability [88].

Especially during long-term exposure at intermediate temperatures, precipitation of the σ phase is a known issue [88, 89], since it leads to rapid degradation of mechanical properties, such as toughness and ductility, due to its inherently brittle nature [88, 89, 90]. Increasing the Cr and Mo content in Fe- and Ni-based alloys is known to increase the stability regime of the σ phase [88, 90].

In 1974, Rudy et al. [86] discovered a ternary σ phase in the Cr-Mo-Si system. The stable compositional range at 1500 °C was described to be: $Cr_{0.39\text{-}0.57}Mo_{0.47\text{-}0.29}Si_{0.14}$. Eutectoid decomposition of the σ phase into (Cr, Mo) solid solution and the A15-$(Cr,Mo)_3Si$ intermetallic phase was observed at temperatures around 1200 °C. More recently in 2022-23 Wu et al. [84, 85] explored the ternary phase diagram of Cr-Mo-Si. Due to the limitation of these studies to isothermal sections at 1000 °C and 1200 °C, the σ phase was not stabilized in their research, which is in line with descriptions by Rudy et al. [86]. The earlier mentioned studies of Hinrichs et al. [34] confirm the presence of a σ phase in the ternary Cr-Mo-Si system and claimed the composition of Cr-32.2Mo-13.5 at.%Si to solidify fully into σ-phase during arc-melting. Also, eutectoid decomposition after annealing the alloy at 1200 °C confirmed the observations by Rudy et al. [86]. The full stability range of the σ phase remains unclear and needs further investigation to prevent it during processing and determine which compositional and temperature ranges can be utilized for a high temperature alloy in the Cr-Mo-Si system.

1.3 The Cr-NiAl system (A2 + B2 approach)

The degree of coherency between the precipitate and the alloy matrix can have a significant influence on the strengthening at high temperatures. High coherency is achieved when the precipitate has a crystal structure and lattice parameter very close to that of the matrix. This can lead to continuous atomic planes across the interface and thus to very low interfacial energy [11, 91]. This is especially relevant at high temperatures, where the low interfacial energy of precipitates leads to superior thermal stability, due to slow coarsening rates. Through heat treatment control, fine and homogenous distribution of coherent precipitates within the matrix phase is possible. This enables a uniform microstructure, which is not easily achieved with non-coherent precipitates (like the A15 phase). The most prominent example of using high-coherency precipitates for strengthening at high temperatures is the γ-γ' microstructure used in several Ni-based superalloys, where γ is the A1(FCC) Ni_{ss} matrix and γ' are the $L1_2$ -Ni_3(Al,Ti) precipitates [11].

Several studies have tried to imitate this principle for BCC base materials [92] (e.g. for Fe [93, 94, 95], Cr [96, 97, 98], W [99, 100] and for high-entropy alloys [12]), combining the disordered BCC matrix with an ordered BCC intermetallic phase like the B2-type [96]. For Cr (A2), NiAl (B2) precipitates provide a low lattice misfit since the lattice parameter for Cr is 2.885 Å [96] and for NiAl is 2.887 Å [101]. Kube et al. [102] calculated in their studies that apart from NiAl, the following B2 phases could also offer a stable A2/B2 phase field in a Cr(Mo) matrix: RuAl, RuNb, FeTi, RuHf, RuZr, RuTi, CoHf, NiTi and CuY.

Ma et al. [96] studied NiAl-strengthened Cr and Cr-Fe alloys and showed that both systems offer reasonable coarsening rates (see Figure 16 a) due to a low misfit of only ~ 0.1% between B2 precipitates and the A2 matrix. It is especially noticable at high temperatures (1000 °C) that the coarsening rates are superior in the Cr(Fe)-NiAl system (~10^2 nm^3/h at 1000 °C), compared to ferritic-superalloys (~10^8 nm^3/h) and Co- and Ni-superalloys (~10^5 nm^3/h) [96]. The strengthening effect was studied via compression testing and revealed that the Cr(Fe)-NiAl alloy reaches a high strength at room temperatue of about 1300 MPa [96] and 320 MPa [96] at 1000 °C (see Figure 16 b).

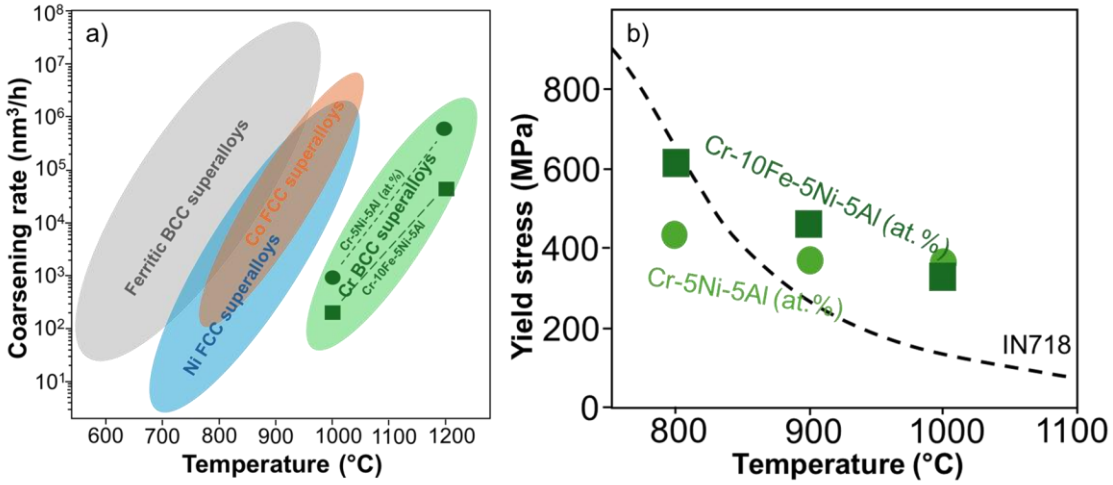

Figure 16: a) Coarsening rates of several alloy systems including the Cr-NiAl A2+B2 system after [96] and b) yield stress vs. temperature of Cr-based alloys strengthened with B2 particles vs. Ni based alloy IN718 after [96].

Microstructual studies on eutectic Cr(Mo)-NiAl systems forming composite materials are available in several studies [103, 104, 105, 106]. However, additions of low amounts of NiAl in the Cr(Mo)-NiAl system targeting precipitation strengthening and the interaction with Si in the system was not previously studied to the authors knowledge.

2 Objectives of Research

The overriding goal of this work is to advance precipitation strengthened Cr-based alloys for high temperature applications and identify future directions for research of high-temperature chromium-based alloys.

The detailed objectives for this work can be formulated as follows:

Initially, the role of Mo in the arc-melted Cr-rich two phase (A2 + A15) Cr-xMo-8 at.%Si alloys is systematically studied. The amount of Si is fixed to 8 at.% to limit the total amount of the intermetallic phase and thus retain reasonable plasticity. Mo contents are varied between of 0-40 at.% to systematically study the influence of Mo on:

- Microstructure (phase composition, formation and distribution in as-cast and annealed states, grain size and shape)
- Stability regime of the σ phase
- The lattice parameter of the phases
- Oxidation and nitridation behavior at 1200°C (via thermogravimetric analysis and cross-sectional evaluation)
- Mechanical properties (hardness of alloys and phases, fracture toughness, compressive strength from 21 to 1000°C)

During this work possible optimization of the microstructure by applying heat treatments is tested and used to expand the limited information about σ phase and the ternary system in the studied compositional range. Based on the findings an optimum amount of Mo in Cr-xMo-8 at.%Si alloys can be determined.

In a further step the gained insights of the Cr-Mo-Si (A2+A15) system are implemented in an alternative precipitation approach. Lower misfit NiAl (B2) particles are introduced to the system, replacing the Cr_3Si (A15) intermetallic, with the goal of improving fracture toughness at room temperature, compared to the A2 + A15 system, while keeping the benefits of Mo and Si in the matrix phase.

3 Results and Discussion (Publications)

3.2 Publication overview

Explanation of the structure of this dissertation:

This dissertation is structured as a cumulative thesis. Accordingly, the introductory chapter, research and objectives, synopsis, conclusions and outlook are written in connection with the following three publications - that form the core of this work - and are accompanied by a separate reference section at the end of the dissertation and a separate list of figures and tables in the beginning. The references cited within each publication are listed individually at the end of the respective articles.

Publication 1: *Koliotassis, L., White, E.M.H. and Galetz, M.C. (2024),* ***The Influence of Mo Content and Annealing on the Oxidation Behavior of Arc-Melted Cr–xMo–8Si Alloys.*** *Advanced Engineering Materials, 26, (2024), 2301906.*
https://doi.org/10.1002/adem.202301906

Arc-melted Cr-xMo-8 at.%Si alloys (with x= 0-40 at.%) are studied focusing on the influence of Mo additions on microstructure in the as-cast and annealed state and analyzing the oxidation behavior at 1200 °C for up to 100 h. A beneficial effect of Mo on the corrosion behavior is observed for up to 25 at.% Mo. Nitridation was inhibited for all Mo-containing alloys. The most promising oxidation behavior was observed for Cr-25Mo-8 at.%Si, showing the formation of a SiO_2 subscale beneath the Cr_2O_3 layer during high-temperature exposure.

Publication 2: *Zander, L., Kerbstadt, M., White, E.M.H. and Galetz, M.C. (2025),* ***Cr-Based High Temperature Alloys - The Strengthening Effect of Molybdenum on Chromium-Silicon Alloys****. International Journal of Refractory Metals and Hard Materials, Volume 132, (2025), 107287. https://doi.org/10.1016/j.ijrmhm.2025.107287*

This study explores how varying molybdenum levels in Cr-xMo-8Si alloys affect mechanical properties such as hardness, strength, and fracture toughness. Increased Mo content enhances hardness and high-temperature strength but

shifts the DBTT to higher temperatures. Despite an initial drop, fracture toughness improves at higher Mo levels due to grain and precipitate refinement, offering insights for future alloy optimization.

Publication 3: *Zander, L., Zander, J. ,Blackburn, T., White, E.M.H., Knowles A. J. and Galetz, M.C. (2025),* ***Advanced Cr-Based BCC Superalloys - A2-B2 Strengthening in the Cr-Mo-Si-(NiAl) System.*** Published in JOM, The Minerals, Metals & Materials Society, Ultra-High Temperature Refractory Metals and Alloys for Complex Environments, 77, (2025), 9608–9622.
https://doi.org/10.1007/s11837-025-07915-w

Advances in the two-phase Cr-Mo-Si system (A2 matrix + A15 precipitate) are combined, with the approach of strengthening the Cr matrix with the low misfit precipitate NiAl (B2). By implementing NiAl (B2) precipitates to a Mo- and Si-strengthened Cr matrix, the developed alloy, Cr-10Mo-3Si-5Ni-5Al (at.%), retains strength up to 1000 °C (specific strength of 95 $N \cdot m \cdot g^{-1}$) without showing the toughness trade-offs, which are present when utilizing A15 phase strengthening. Adjusting Mo and Si content as well as decreasing the Ni/Al ratio helps to suppress brittle σ phase formation.

3.3 The Influence of Mo Content and Annealing on the Oxidation Behavior of Arc-Melted Cr-xMo-8Si Alloys

Published in Advanced Engineering Materials, 26, 17 (2024), 2301906
DOI: 10.1002/adem.202301906

Authors
Lisa Koliotassis[1], Emma M. H. White[1], Mathias C. Galetz[1]

[1] DECHEMA Research Institute, Theodor-Heuss-Allee 25, 60486 Frankfurt a.M., GER.

Abstract
The influence of Mo (10–40 at.%) additions to Cr–8 at.%Si is systematically studied by analyzing arc-melted alloys in the as-cast and annealed state. The oxidation resistance is tested by thermogravimetric analysis (TGA) at 1200 °C in air for up to 100 h. Samples are characterized by X-ray diffraction, scanning electron microscopy, and wavelength-dispersive X-ray spectroscopy. The studied Cr–*x*Mo–8Si alloy series shows a beneficial effect of Mo on the corrosion behavior. For all of the investigated Mo contents, no nitridation is observed and the oxide scale adhesion is improved. An increased amount of intermetallic A15 phase leads to the formation of a SiO_2 scale beneath the Cr_2O_3 layer during high-temperature exposure. The internal SiO_2 layer inhibits further internal oxidation of the A15 phase. Uniform size and distribution of A15, benefits the formation of a duplex oxide scale. Cr–25Mo–8 at.%Si, shows the most promising oxidation behavior. The TGA data follows the paralinear law, with both the growth rate, k_p, and volatilization rate, k_v, of Cr_2O_3 being reduced by adding 10–25 at.% Mo. A binary Cr/Mo–Si phase diagram is generated in order to determine accurate annealing conditions and estimate the stability range of the metastable σ phase.

1. Introduction

One possibility to decrease efficiency losses in high-temperature applications, such as gas turbines, is to exchange the state-of the-art Ni-based superalloys with materials that do not require additional internal cooling [1,2]. This can be realized by materials that allow higher service temperatures while retaining high mechanical strength, such as refractory metal alloys [1,3]. One promising base

material candidate among the refractory metals is chromium [4]. Cr as a base material has a lower density and higher melting temperature when compared to nickel, while being abundant and reasonably priced [5–7]. Challenges in developing Cr-based alloys are mainly connected to high-temperature mechanisms like fast nitridation, as well as the spallation and evaporation of protective chromia layers above 1000 °C [8–10] An often-discussed additional challenge is the high ductile-to-brittle transition temperature (DBTT) of Cr, which has been linked to impurities and can be influenced by alloying [1,4,11,12].

Alloying Cr with 4–15 at.% Si leads to the formation of a two-phase microstructure composed of an A2 (Cr_{ss}) matrix and nitridation-resistant A15 (Cr3Si) precipitates [13,14], resulting in increased mechanical strength at high temperatures [15,16], higher oxidation resistance [14], decreased nitridation of A2, and lower volatilization of chromia at 1200 °C [14,17]. With more Si added to Cr, the A15 phase fraction increases and thus the oxidation properties improve. On the downside, additional Si lowers the fracture toughness at low temperatures [15,18], which limits application as structural material.

Alloying Mo as a ternary element results in the substitution of Cr by Mo in both the A2 and A15 phases [19]. Matrix coarsening resistance, solid solution hardening of A2, further improvement of creep properties of the A15 phase, and promoted SiO_2 formation have all been attributed to Mo alloying [16,20]. Adding up to 2 at.% Mo resulted in an equal distribution of Mo between the A2 and A15 phases and reduced nitridation of the solid solution while further decreasing the volatilization rate during exposure in air at 1200 °C [20]. Recent studies showed that adding approximately 32 at.% Mo to Cr–13.5 at.%Si fully suppressed nitridation [21]. Stability of the system in the Mo pesting regime of 800 °C has also been confirmed [21]. The ternary Cr–Mo–Si system is well described in the literature [22–24]. Rudy et al. state that the Cr–Mo–Si system contains a metastable σ phase ($Cr_{0.39\text{-}0.57}Mo_{0.29\text{-}0.47}Si_{14}$) [25]. The stability regime of the σ phase is under discussion [22], which is important because the formation of the σ phase can produce cracks during processing and it is transformed into A2 and A15 when annealed at 1200 °C [25].

This work systematically investigates the microstructure development, phase formation, and high-temperature oxidation resistance of arc-melted Cr-rich Cr–

*x*Mo–8Si alloys (x = 10–40 at.%) as a function of the Mo content and annealing temperatures. The Si content was fixed at 8 at.% in order to prevent initial A15 phase formation in the as-cast (AC) arc-melted ingots and to allow a reasonable fracture toughness. The AC state was compared to the annealed (AN) state through determining phase compositions and microstructures. Thermogravimetric analysis (TGA) tests were performed in air at 1200 °C for up to 100 h to evaluate the influence of varying Mo content in Cr–*x*Mo–8Si alloys on the oxidation resistance.

2. Results and Discussion

2.1 Microstructure and Phase Analysis

2.1.1 Arc-Melted Samples

X-ray diffraction (XRD) results of the AC Cr–*x*Mo–8Si series are depicted in Figure 1. All samples contain the cubic A2 phase of Cr. As Mo is fully soluble in the A2 Cr phase and is the larger atom [19,26], increasing the Mo content leads to a shift in the A2 reflections to lower angles, corresponding to a larger LP. No primary precipitation of intermetallic $(Cr,Mo)_3Si$ phase (A15) phase was observed in the Cr–8Si reference sample. For the 10 and 20 at.% Mo samples, a slight

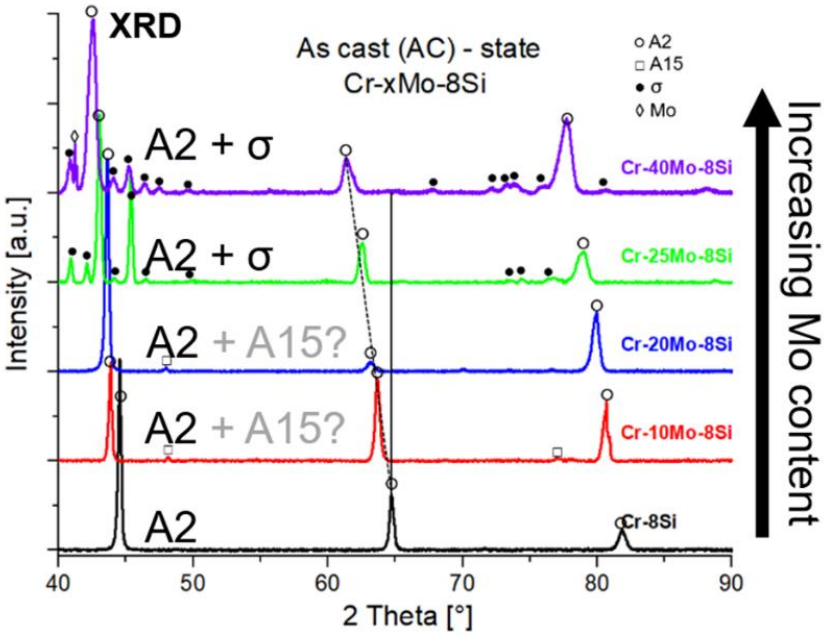

Figure 1: XRD of AC states of the Cr–xMo–8Si alloy series.

indication for A15 phase was visible, whereas the samples with 25 and 40 at.% Mo show the formation of σ phase instead.

These results are confirmed by WDS measurements (Table 1). For 20, 25, and 40 at.% Mo, two A2 phases were observed: “A2_B” is richer in Mo and poorer in Si than the “A2_A.” This segregation within the A2 explains the increasing broadening of the XRD reflection of the Cr solid solution.

EPMA maps of the Cr–*x*Mo–8Si series (Figure 2) show the semiquantitative distribution of elements in the microstructure. Note that the A15 phase is not present in these images due to the very minor amount present in only the 10 and 20 at.% Mo samples. An increased Mo content in the Cr–*x*Mo–8Si system leads to increasing inhomogeneity in the elemental distribution. For 10 at.% Mo, the distribution of all elements appears homogeneous, while the 20–40 at.% Mo samples show increasing segregation, as reflected in the broadening of the A2 reflection (Figure 1) and the two types of A2 reported in Table 1. Strong dendritic solidification is observed for Mo contents of 25 and 40 at.%, where the σ phase is present. Mo is preferably enriched in Si-poor areas, which is the location of A2 phase.

Table 1: EPMA/WDS quantitative measurements of the observed phases in the AC states.

Nominal composition	Phase	Cr [at%]		Mo [at%]		Si [at%]	
Cr–10Mo–8Si	A2	82.9	1.4	10.0	0.3	7.0	1.2
	A15	70.0	0.2	11.2	0.2	18.8	0.4
Cr–20Mo–8Si	A2_A	74.5	0.4	18.2	0.2	7.3	0.5
	A2_B	74.8	0.3	19.0	0.3	6.3	0.5
	A15	65.4	0.2	17.4	0.2	17.2	1.4
Cr–25Mo–8Si	A2_A	68.1	1.0	25.1	1.3	6.8	1.0
	A2_B	66.2	1.0	28.6	1.4	5.2	0.5
	σ	64.1	0.8	23.0	0.8	13.0	0.6
Cr–40Mo–8Si	A2_A	52.6	3.1	42.1	3.7	5.3	0.7
	A2_B	45.0	1.6	51.6	1.9	3.4	0.4
	σ	56.7	2.0	31.0	2.9	12.3	1.1

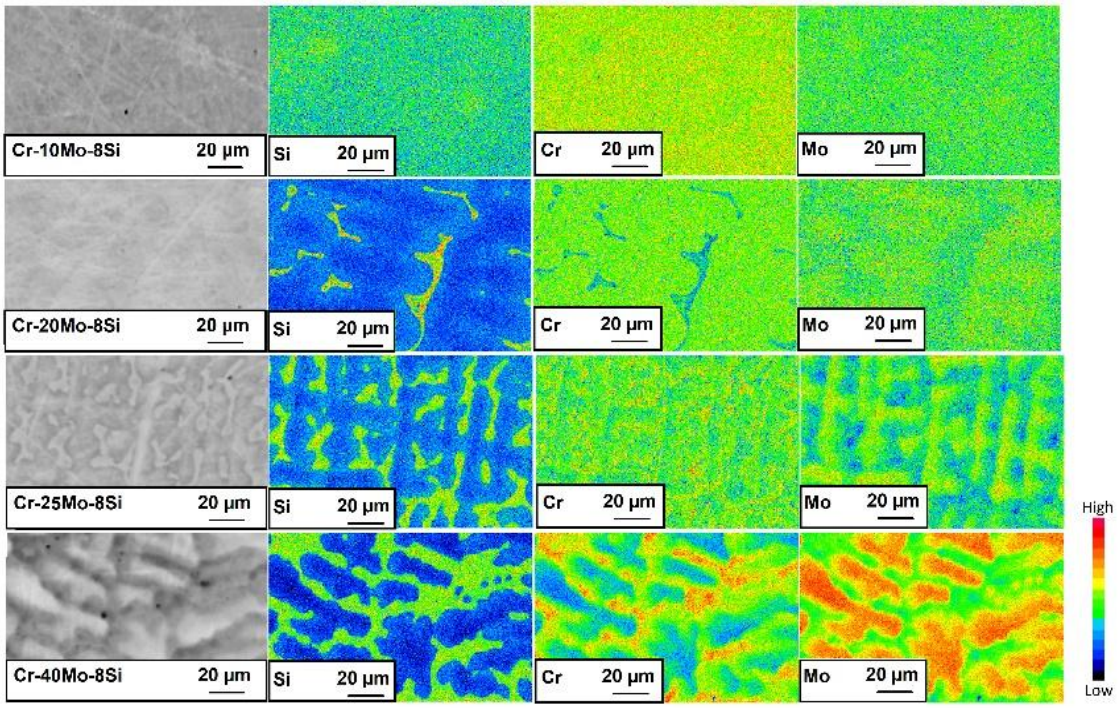

Figure 2: EPMA/WDS maps of AC states of the Cr–xMo–8Si alloy series.

2.1.2 Annealed States

The two types of anneals that were performed were under the same Ar/5%H2 atmosphere for the same duration of 100 h and were both followed by a water quench (Q); thus, the only difference was the temperature of 1200 °C or 1350 °C. Figure 3 shows the diffractograms and calculated LPs for the 1200 and 1350 °C anneals of the Cr–*x*Mo–8Si series. After annealing at 1200 °C for 100 h, all samples of the Cr–*x*Mo–8Si series showed formation of the A15 phase in addition to the A2 solid solution. The formerly visible σ phase decomposed to A15 and A2 in both cases, which is in line with the suggested phase diagram presented in ref. [22]. For the anneal at 1350 °C, the behavior is similar except for the sample containing 40 at.% Mo. For 40 at.% Mo, some A15 did form but the σ phase remained, suggesting the stable regime of the σ phase is in line with the ternary diagram for Cr–Si–Mo at 1300 °C in ref. [22].

The calculated LPs of the A15 and A2 phases are plotted against the Cr/Mo ratio (as determined by WDS) in Figure 3c. The LP of the A2 phase ranges from a minimum 2.92 Å (Cr–*x*Mo–8Si with *x* = 10 at.%) to a maximum of 3.02 Å (Cr–*x*Mo–8Si with *x* = 40 at.%), whereas the LP for the A15 phase varies between 4.62 and 4.72 Å. Interestingly, in both cases an increase of about 0.1 Å results for the same overall increase in Mo content (Cr–*x*Mo–8Si with 10 vs 40 at.% Mo), even though the Mo contents in the respective phases are not the same (higher in A2 than in A15, see Section 2.1.3). After both anneals, the LPs of the A2 phases are consistent with the literature data [19,27].

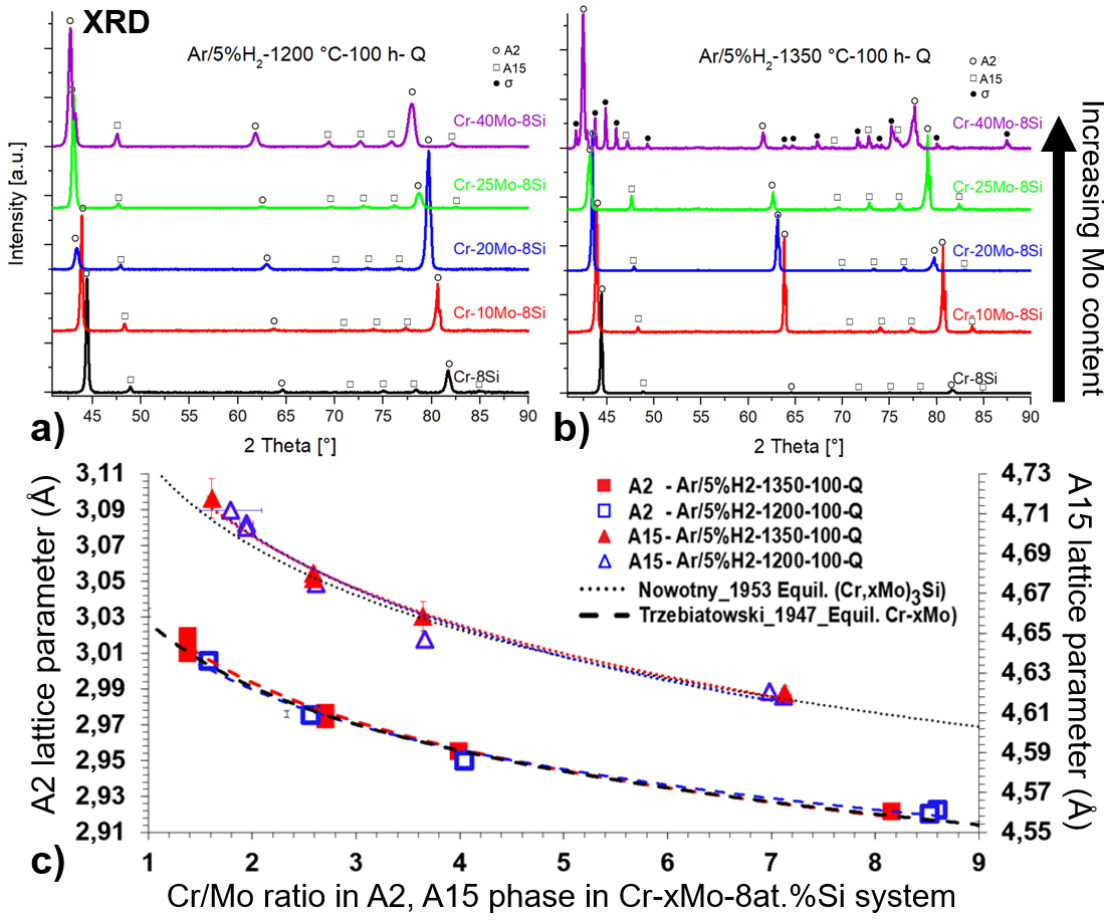

Figure 3: a) XRD after 1200 °C anneal; b) XRD after 1350 °C anneal; and c) LPs of A2 and A15 phases as a function of the Cr/Mo ratio including the trendlines for the literature data of refs. [19,27].

Microstructural observations (see Section 2.1.3) of both anneals (1200 and 1350 °C) show that for the lower 1200 °C anneal and the samples with Mo contents ≥25 at.%, the strongly pronounced dendritic microstructure from the AC condition determines the regions where the A15 phase formed (predominantly in

the formerly Si-rich areas). The overall distribution of the A15 phase is thus inhomogeneous. For Mo contents ≤20 at.%, A15 precipitation along the grain boundaries is dominant. The A15 precipitates inside the grains are also rather irregularly spread. For the higher 1350 °C anneal, the A15 precipitates coarsened and were overall fewer in quantity, but were more homogeneous in size and distribution, especially for Cr–25Mo–8Si. Grain boundary precipitation of the A15 phase was observed for 10 and 20 at.% Mo after the 1200 °C anneal, while this effect was only dominant for the 10 at.% Mo sample after the 1350 °C anneal. An increased Mo content appears to reduce the grain boundary precipitation of A15. Similar effects have been described in refs. [16,28] for low Mo contents of 2 at.%. Higher temperature annealing provides the additional benefit of reducing grain boundary precipitates.

Using phase compositional data from wavelength-dispersive X-ray spectroscopy (EPMA/WDS), the influence of the Mo content on the Mo distribution inside the phases, the Si solubility, and the overall amount of A15 phase was analyzed (Figure 4a–c). The distribution coefficient, k, was calculated via Equation (1):

$$k = \frac{c_{Mo}(A15)}{c_{Mo}(A2)} \tag{1}$$

It can be seen even though Mo is present in both phases (A2 and A15), Mo is preferably enriched in the A2 phase and this effect increases with increasing Mo content and is stronger for the lower 1200 °C anneal (Figure 4a). The Si solubility

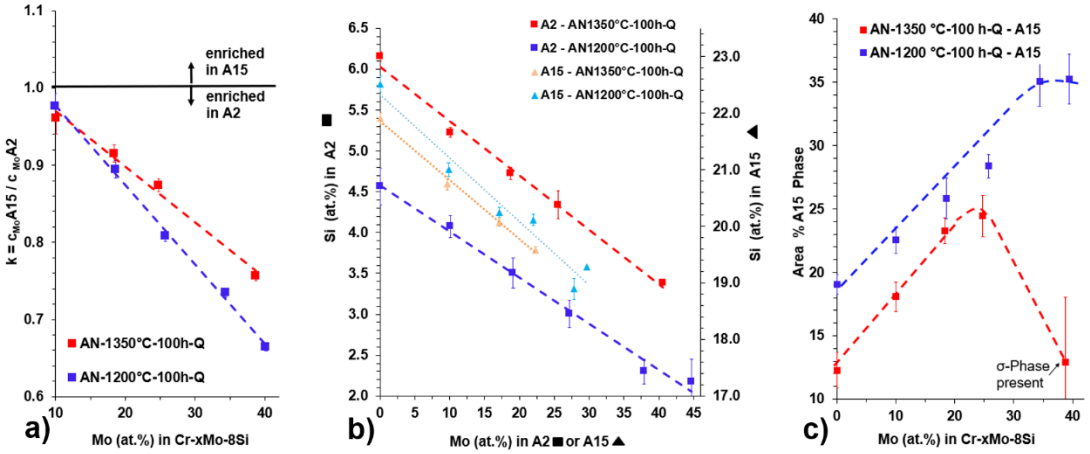

Figure 4: Influence of Mo content on the a) Mo distribution, b) Si solubility, and c) amount of A15 phase.

decreases linearly in both phases with increasing Mo content (Figure 4b). This leads to an increasing amount of intermetallic A15 phase with increasing Mo content (Figure 4c). One extra sample containing 35 at.% Mo was produced and added to the 1200 °C anneal to confirm that a plateau is approached at around 35 area percent of A15 due to the limited overall Si content (8 at.%). The proportion of the A15 phase is strongly reduced in Cr–40Mo–8Si due to the presence of the σ phase.

2.1.3 Quasibinary Cr/Mo – Si Phase Diagram

To gain a better understanding of annealing conditions for arc-melted Cr–xMo–8Si samples, the WDS data (Table 2) were used to develop a quasibinary Cr/Mo–Si phase diagram (Figure 5). For this purpose, a third annealing at 1450 °C was performed and Si solubilities of A2 and A15 phases were added and compared to the literature data for the Cr–Si and Mo–Si binary phase diagrams. A stable regime of the σ phase was observed for 25 and 40 at.% Mo at 1450 and 1350 °C, respectively. Increasing the Mo content in Cr–xMo–8Si shifts the phase boundary between the A2 single phase field and the A2 + A15 regime, as well as between the A15 + A2 and A15 single-phase field, to lower Si contents when compared to the Cr–Si system. To further improve the distribution of the intermetallic A15 phase inside the solid solution A2 matrix, a two-step precipitation hardening anneal would likely be beneficial. This type of anneal consists of a homogenization step at high temperature, entering the single-phase field (A2) and adding a precipitation anneal at a lower temperature (two-phase field of A2 + A15). For the studied alloy series, temperatures of >1600 °C would be necessary to enter the single-phase field, which can result in rather strong Cr evaporation during the anneal. Also due to uncertainty about where σ phase is stable, a higher temperature anneal might lead to an A2 + σ phase mixture instead of single-phase A2. An alternative way to address even A15 distribution without heat treatment >1600 °C could be the development of a powder metallurgical production route for these kinds of alloys.

Table 2: WDS analysis of investigated samples.

Nominal	Phase	Ar/5%H2–1200 °C–100 h–Q									
		Cr [at%]		Mo [at%]		Si [at%]		Cr/Mo		Area [%]	
Cr–8Si	All	92.0	0.1	–	–	8.0	0.1	–	–	100	
	A2	95.4	0.2	–	–	4.6	0.2	–	–	81.0	2.0
	A15	77.5	0.1	–	–	22.5	0.1	–	–	19.0	0.8
Cr–10Mo–8Si	All	82.1	0.1	10.0	0.1	7.9	0.1	8.20	0.01	100	
	A2	85.9	0.1	10.1	0.1	4.1	0.1	8.53	0.01	77.5	2.0
	A15	69.2	0.1	9.8	0.1	21.0	0.1	7.03	0.01	22.5	1.1
Cr–20Mo–8Si	All	73.6	0.1	18.6	0.1	7.8	0.1	3.95	0.01	100	
	A2	77.4	0.1	19.1	0.1	3.5	0.2	4.05	0.01	74.2	2.0
	A15	62.7	0.1	17.1	0.1	20.2	0.1	3.66	0.01	25.8	1.6
Cr–25Mo–8Si	All	66.4	0.1	25.7	0.1	7.9	0.1	2.58	0.00	100	
	A2	69.8	0.1	27.2	0.1	3.0	0.2	2.57	0.01	71.6	2.0
	A15	57.9	0.1	22.0	0.1	20.1	0.1	2.64	0.01	28.4	0.9
Cr–40Mo–8Si	All	52.4	0.1	39.4	0.1	8.2	0.2	1.33	0.00	100	
	A2	53.1	0.1	44.7	0.1	2.2	0.3	1.19	0.01	64.8	2.0
	A15	51.0	0.1	29.7	0.1	19.3	0.2	1.72	0.01	35.2	2.0

Nominal	Phase	Ar/5%H2–1350 °C–100 h–Q									
		Cr [at%]		Mo [at%]		Si [at%]		Cr/Mo		Area [%]	
Cr–8Si	All	91.9	0.1	–	–	8.1	0.1	–	–	100	
	A2	93.8	0.1	–	–	6.2	0.1	–	–	87.7	2.0
	A15	78.1	0.1	–	–	21.9	0.1	–	–	12.3	1.4
Cr–10Mo–8Si	All	81.9	0.1	10.0	0.1	8.0	0.1	8.17	0.01	100	
	A2	84.7	0.1	10.1	0.1	5.2	0.1	8.38	0.01	81.9	2.0
	A15	69.5	0.1	9.7	0.1	20.7	0.1	7.16	0.01	18.1	1.2
Cr–20Mo–8Si	All	73.3	0.1	18.4	0.1	8.3	0.1	3.99	0.01	100	
	A2	76.5	0.1	18.7	0.1	4.7	0.1	4.08	0.01	76.7	2.0
	A15	62.8	0.1	17.1	0.1	20.1	0.1	3.66	0.01	23.3	1.0

Nominal	Phase	Ar/5%H2–1350 °C–100 h–Q									
		Cr [at%]		Mo [at%]		Si [at%]		Cr/Mo		Area [%]	
Cr–25Mo–8Si	All	67.2	0.1	24.8	0.1	8.1	0.1	2.71	0.01	100	
	A2	70.1	0.1	25.5	0.1	4.3	0.2	2.74	0.01	75.6	2.0
	A15	58.1	0.1	22.3	0.1	19.6	0.1	2.60	0.01	24.4	1.6
Cr–40Mo–8Si	All	53.1	0.7	38.3	0.7	8.6	0.7	1.38	0.03	100	
	A2	56.0	0.1	40.6	0.1	3.4	0.1	1.38	0.01	53.5	4.0
	A15	48.7	0.1	30.7	0.1	20.6	0.1	1.59	0.01	12.9	6.0
	σ	50.0	0.8	37.6	0.8	12.4	0.5	1.33	0.04	33.6	4.0

Nominal	Phase	Ar/5%H2–1450 °C–20 h–Q									
		Cr [at%]		Mo [at%]		Si [at%]		Cr/Mo		Area [%]	
Cr–10Mo–8Si	All	81.9	0.1	10.0	0.1	8.1	0.1	8.18	0.01	100	
	A2	83.3	0.2	10.1	0.1	6.6	0.2	8.28	0.01	89.6	2.0
	A15	69.8	0.1	9.6	0.1	20.6	0.2	7.31	0.01	10.4	1.0
Cr–20Mo–8Si	All	72.2	0.0	19.8	0.1	7.9	0.1	3.64	0.01	100	
	A2	74.0	0.1	20.1	0.1	5.9	0.2	3.69	0.01	85.9	2.0
	A15	61.5	0.2	18.5	0.1	20.0	0.3	3.33	0.01	14.1	1.5
Cr–25Mo–8Si	All	61.7	0.1	30.0	0.2	8.3	0.3	2.05	0.01	100	
	A2	65.4	0.2	29.3	0.1	5.3	0.1	2.23	0.01	61.1	2.0
	A15	54.9	0.2	25.4	0.3	19.7	0.7	2.16	0.02	2.5	4.0
	σ	55.8	0.1	31.7	0.1	12.5	0.1	1.76	0.00	36.4	2.0
Cr–40Mo–8Si	All	54.5	0.0	38.1	0.1	8.4	0.1	1.43	0.00	100	
	A2	56.8	0.1	38.8	0.2	4.3	0.3	1.46	0.01	49.8	2.0
	σ	51.1	0.1	36.7	0.2	12.2	0.3	1.39	0.01	51.2	2.0

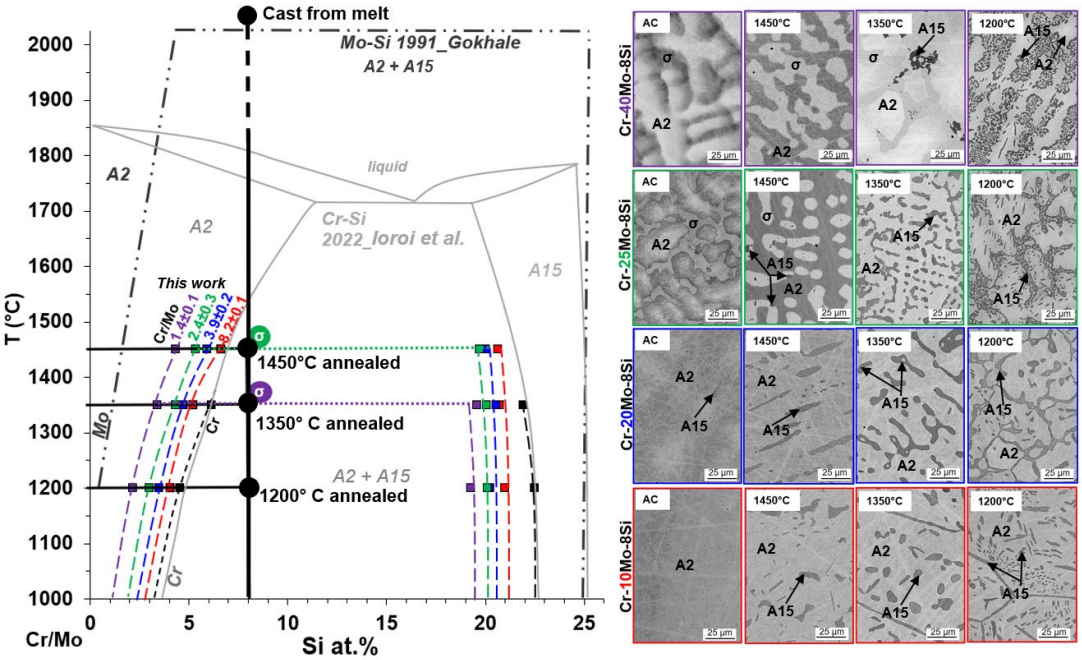

Figure 5: Graphical estimation of the quasibinary phase diagram of Cr/Mo-Si based on the studied alloys including Mo–Si and Cr–Si data from refs. [13,39] (l.); microstructures of the studied alloys after arc melting and varying anneals (r.).

2.2 High Temperature Corrosion Behavior in Air

2.2.1 Adhesion of Oxide Layer Versus Composition

The results of oxidation exposures of samples annealed at 1350 °C are visible in Figure 6. The macro images of the alloy series exposed at 1200 °C in static laboratory air for 50 h are compared with a second experiment of cuboids exposed at 1200 °C in flowing dry synthetic air for 100 h.

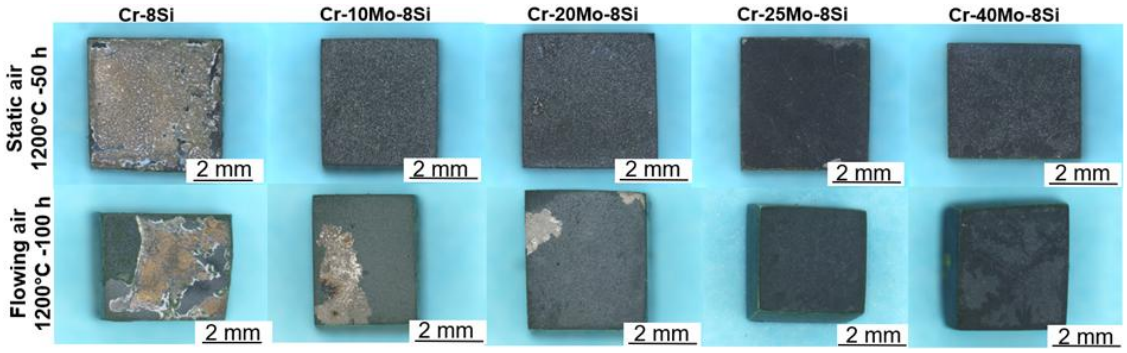

Figure 6: Cuboids after exposure at 1200 °C in static and flowing air for 50 and 100 h.

Note that the difference in shape and size of the cuboids (especially the bottom row of Figure 6) is due to manufacturing and not due to oxidation effects. For the 50 h exposure, the reference sample without Mo is the only sample showing severe spallation of the dark gray oxide that formed. All Mo-containing samples showed no obvious spallation except for some regions near the edges of the cuboids. XRD identified the dark gray oxide as Cr_2O_3.

For the 100 h exposures in flowing air, not only the reference, but also the 10 and 20 at.% Mo compositions show some spallation of the oxide, while the 25 and 40 at.% Mo alloys do not show any spallation. As the cuboids with 10 and 20 at.% Mo did not show sudden mass decrease during the exposure duration, it is likely that the rather harsh cooling conditions in flowing air lead to spallation.

These results suggest that Mo has a positive influence on the adhesion of the formed oxide layer as the alloys containing 25 at.% Mo or more did not show spallation during the experiments. Chromia scales are known to contain compressive stresses that lead to buckling and spallation, especially when grown on pure Cr [17,29–31]. This has been linked to the formation of a duplex oxide of outward growing columnar chromia grains and inward growing equiaxed chromia grains in oxidizing atmospheres, where the new oxide forms within the scale and

creates such stresses [32,33]. It is assumed that detachment of the external and internal part of the oxide scale occurs during cooling, causing spallation [32]. The addition of Mo alters this scale growth mechanism and leads to lower stresses in the scale, either by doping or the creation of free volume by Mo volatilization. In either case, it prevents scale spallation.

2.2.2 Cross Sections - Exposure in Static Laboratory Air at 1200 °C for 50 h

Electron images and EPMA/WDS maps of surface cross sections of oxidized regions of the arc-melted cuboids annealed at 1350 °C and exposed at 1200 °C in static laboratory air for 50 h are depicted in Figure 7.

The elemental distributions (Figure 7) show that the Cr–8Si reference is the only sample that formed a nitrogen-rich subsurface phase. Due to spallation of chromia in most areas, XRD could confirm that Cr_2N formed in the subsurface zone. The alloys containing Mo annealed in laboratory air for 50 h at 1200 °C did not show any nitridation of the Cr solid solution as compared to Cr–8Si. Mo contents ≥10 at.% in Cr–*x*Mo–8Si fully inhibit nitridation of the A2 matrix. Apart from formation of a 10 ± 2 µm chromia layer, the elemental maps of Figure 7 show internal oxidation of the former A15 precipitates, especially for 10 and 20 at.% Mo. Spot measurements from WDS suggest A15 oxidizes to SiO_2. The A15 phase does seem to be nitridation resistant, but is internally oxidized for Mo contents below 25 at.%.

For the 10 and 20 at.% Mo samples, a very similar behavior is observed but the internal oxidation depth is increased and the thickness of the chromia layer is decreased as compared to the reference sample as summarized in Table 3. It should be noted that the images shown in Figure 7 are not the only ones used for determination of the average scale thicknesses and oxidation depths. The A2 phase is Si depleted in the interdiffusion zone, which is especially visible for 0 to 20 at.% Mo in Figure 7. Surprisingly, Cr–25Mo–8Si shows almost no internal oxidation of the A15 phase, but a rather thick continuous chromia layer. However, 40 at.% Mo shows not only outward growing chromia, but also inward growth of the oxide, separated by discontinuous SiO_2 particles that likely developed out of former A15 phase precipitates. Cr–40Mo–8Si overall shows the thickest chromia

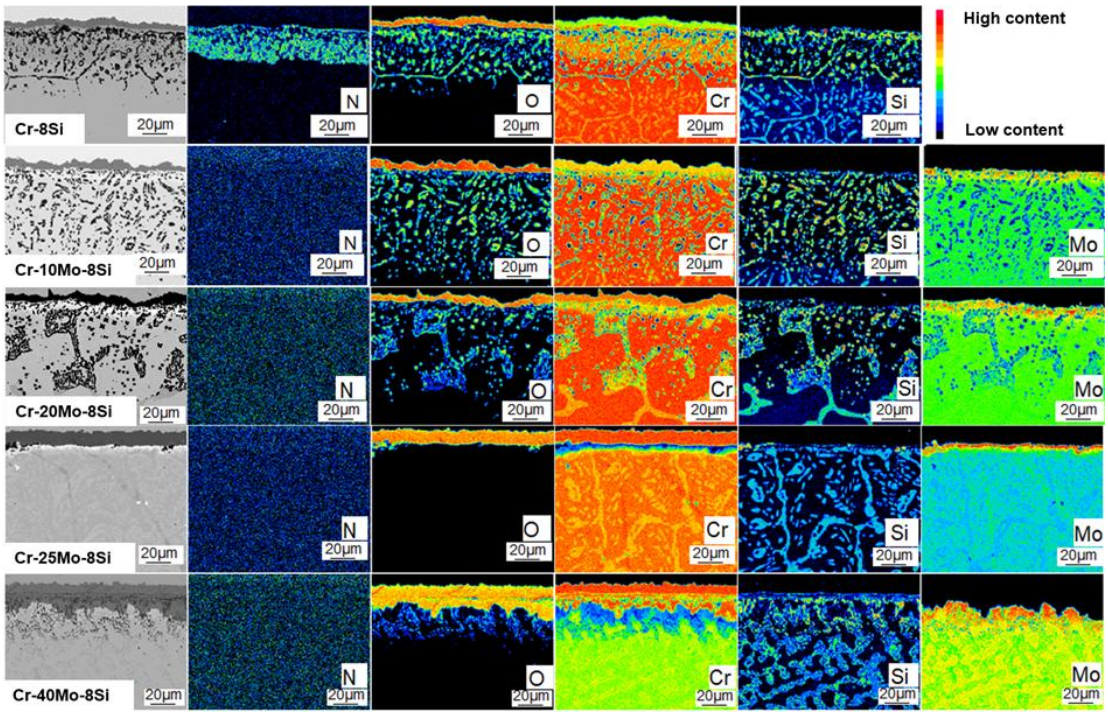

Figure 7: Surface cross-sectional electron microscope and EPMA/WDS maps of oxidized regions of varying Mo-content samples annealed at 1350 °C and exposed to static laboratory air at 1200 °C for 50 h.

scale (23 ± 5 µm) and a rather low internal oxidation depth of A15 when compared to the reference sample without Mo.

Mo is strongly enriched in the layer beneath the oxide scale, forming a Mo-enriched A2 phase. The outer chromia oxide layer thickness increases with increasing Mo content, while the penetration depth of the internal oxidation (A15 → SiO_2) decreases simultaneously.

The exceptionally good oxidation behavior of Cr-25Mo-8Si can be explained through a closer examination of the subscale beneath the chromia layer (Figure 8). Negligible internal oxidation occurs, and instead a continuous SiO_2 subscale forms beneath the chromia layer. There appears to be a threshold of Mo content that increases the Si activity to a degree where Si outward diffusion is faster than O inward diffusion, and thus, initially a dense SiO_2 layer below the Cr_2O_3 layer is able to form. In addition to the increase in Si activity, however, a minimum fraction of A15 phase must be present and the precipitates must be within a certain proximity to each other in order to create this continuous SiO_2 layer. Figure 8b

shows the oxide scale formed on a Cr–25Mo–8Si sample previously annealed at 1200 °C with a less homogenous distribution of the A15 phase. During oxidation at 1200 °C in air, this leads to the formation of discontinuous SiO_2 and thus also internal oxidation of A15 occurred. So, not only the composition, but also the annealing conditions have a large influence on the oxidation behavior of Cr–25Mo–8Si.

Table 3: Chromia thickness and internal oxidation depth of A15 phase in Cr-xMo-8Si after exposure at 1200 °C for 50 h in static laboratory air.

Nominal composition	Anneal T [°C]–100 h–Q	Exposure at 1200 °C in static air for 50 h	
		Chromia scale thickness d [µm]	Internal oxidation depth [µm]
Reference Cr–8Si[a)]	1200	10 ± 2	44 ± 9
Cr–10Mo–8Si	1200	7 ± 3	81 ± 6
	1350	6 ± 1	87 ± 6
Cr–20Mo–8Si	1200	13 ± 1	47 ± 4
	1350	6 ± 1	80 ± 2
Cr–25Mo–8Si	1200	12 ± 2	16 ± 3
	1350	11 ± 1	1 ± 4
Cr–40Mo–8Si	1200	21 ± 3	38 ± 9
	1350	23 ± 5	18 ± 1

[a)] Nitridation of A2 and strong spallation of chromia observed.

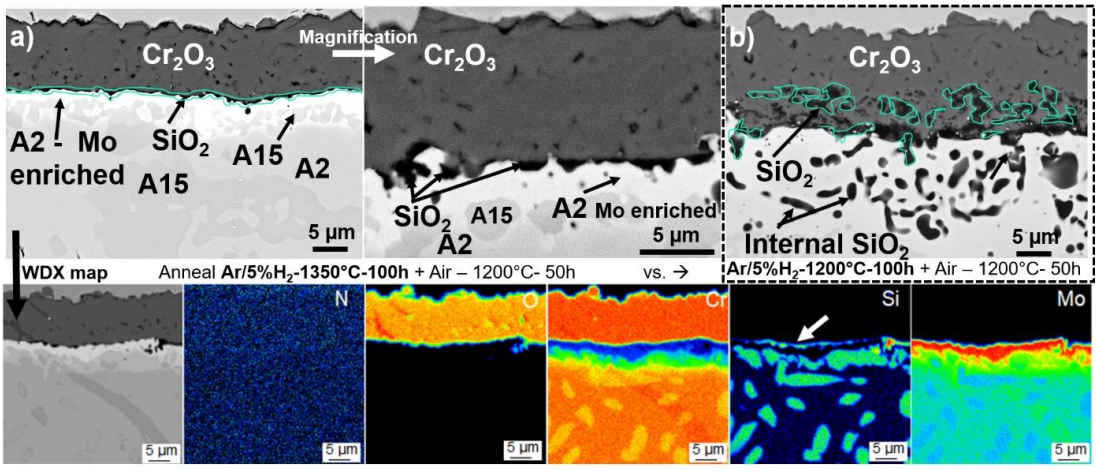

Figure 8: Scanning electron microscopy images and EPMA/WDS maps of surface cross sections of oxidized Cr–25Mo–8Si (static air, 1200 °C for 50 h) for two different anneals: a) 1350 °C and b) 1200°C.

2.2.3 Thermogravimetric Analysis (Air- 1200 °C-100 h)

The mass changes during exposure at 1200 °C in dry synthetic air for 100 h are plotted in Figure 9a. The Cr–8Si reference sample suffers from breakaway oxidation, as also described in ref. [34], after around 95 h and reaches an overall mass gain of 3.4 mg·cm^{-2} after 100 h. The mass gain is lower for Mo-containing samples and reaches 3.1 mg·cm^{-2} for Cr–10Mo–8Si, 2.3 mg·cm^{-2} for Cr–20Mo–8Si, and only 1.5 mg·cm^{-2} for Cr–25Mo–8Si. All curves up to 25 at.% Mo initially show a parabolic growth rate and then change to paralinear behavior. The Cr–

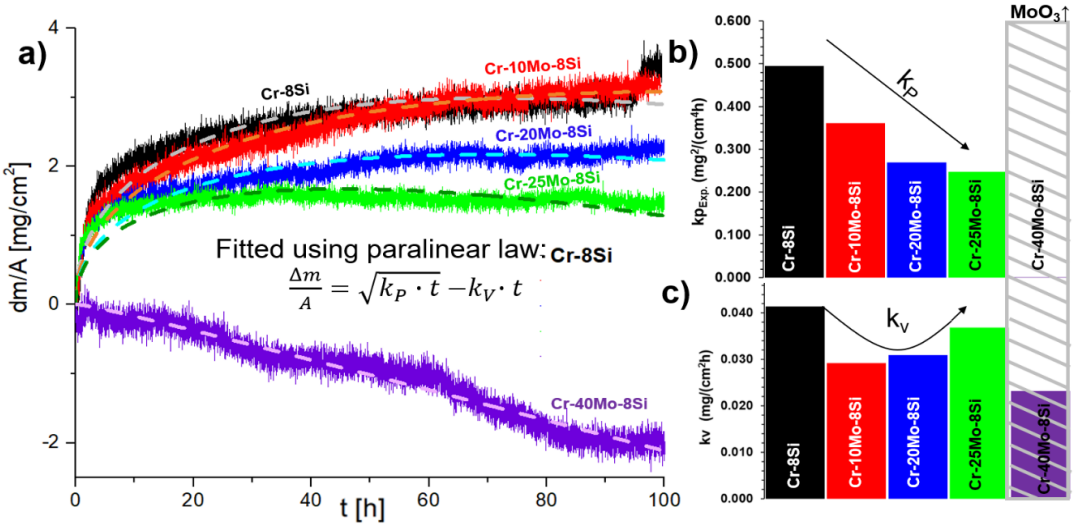

Figure 9: a) Mass changes and b) calculated parabolic (kp) and c) volatilization rate (kv) for exposures at 1200 °C for 100 h in flowing dry synthetic air.

40Mo–8Si alloy shows continuous mass loss, reaching -2 mg·cm^{-2}. The trend is not perfectly linear and hints at a rather complex process of oxide formation and volatilization of likely more than one species.

Besides some MoO_3 evaporation, the chromia scale can form the volatile oxide CrO_3 (Equation (2)) at the investigated temperature [10,35]. Thus, the mass gain of the specimens can be described by a parabolic growth rate, k_p, and a linear volatilization rate, k_v. Therefore, the paralinear law depicted in Equation (3) was used to fit all of the mass gain curves and determine values of k_p and k_v as included in Figure 9b,c. The origin of the paralinear law used here is described in ref. [10].

$$Cr_2O_3 + \frac{3}{2}O_2(g) = 2CrO_3(g) \qquad (2)$$

$$\frac{\Delta m}{A} = \sqrt{k_p t} - k_v t \quad (3)$$

The calculations show that the parabolic growth rate of the oxides decreased with increasing Mo content (Figure 9b). While the reference Cr–8Si shows a k_p of 0.4953 $mg^2 \cdot cm^{-4} \cdot h^{-1}$, it decreases to 0.2474 $mg^2 \cdot cm^{-4} \cdot h^{-1}$ for 25 at.% Mo. Correspondingly, Table 3 confirms that the chromia thicknesses decrease for specimens containing 10–20 at.% Mo. For Cr–25Mo–8Si, the chromia layer has a similar thickness as the Cr–8Si reference (Table 3), but the internal oxidation of A15 was inhibited and thus an overall lower k_p value is reasonable. Trying to use the paralinear fit for the Cr–40Mo–8Si alloy does not allow for good agreement with the cross sections and a reasonable value for k_p. The cross sections showed that the chromia layer is the thickest for this composition, while the calculated k_p has the lowest value of 0.004 $mg^2 \cdot cm^{-4} \cdot h^{-1}$. As this composition is the only one showing strong continuous mass loss, it is likely that not only chromia is evaporating but also large amounts of MoO_3 are also volatilizing due to the high Mo content. Additionally, some internal oxidation is evident. So, for the Cr–40Mo–8Si composition volatilization dominates the oxidation mechanisms and the paralinear law for the description of oxide growth kinetics cannot be used. The volatilization rate, k_v (Figure 9c), for the reference sample Cr–8Si is 0.0414 $mg \cdot cm^{-2} \cdot h^{-1}$. It decreases for the Mo containing samples to 0.0293, 0.0309, and 0.0369 $mg \cdot cm^{-2} \cdot h^{-1}$ for 10, 20, and 25 at.% Mo, respectively. These values are higher than for other non-Mo-containing chromia forming alloys like, e.g., Ni–40Cr, which are around 0.0145–0.0149 $mg \cdot cm^{-2} \cdot h^{-1}$ described in refs. [36,37].

The oxide growth kinetics and adherent oxide scales of the Cr–*x*Mo–8Si alloys (x = 10, 20, and 25 at.%) show high potential for a new class of lightweight refractory alloys for high temperature applications. Especially worthwhile of further development is the Cr–25Mo–8Si alloy with extremely low mass gain and continuous SiO_2 subscale formation, preventing internal oxidation. Future investigations will include long-term exposures up to 1000 h to see if the Mo-enriched layer beneath the duplex oxide scale remains stable, or will lead to spontaneous failure due to formation of MoO_3. The keys to future work within this class of alloys will be avoiding σ phase formation and ensuring uniform

distribution of the A15 phase, while perhaps lowering the DBTT which was not addressed in this work.

3. Conclusions

Mo additions of up to 25 at.% to Cr–8Si change the microstructure of annealed arc-melted alloys and have a beneficial effect on the oxidation behavior at 1200 °C in air.

Microstructural summary: 1) Mo is present in both A2 and A15 phases but is preferably enriched in A2. This effect increases with increasing Mo content. 2) Grain boundary precipitation of A15 phase is reduced for increased Mo contents and increased annealing temperature. 3) Increasing the amount of Mo leads to decreased solubility of Si in both phases (A2 + A15) and thus leads to an increasing amount of A15 phase. 4) Higher temperature anneal (1350 °C vs 1200 °C) of arc-melted alloys leads to less and coarser, but overall more evenly distributed, A15 precipitates. 5) A binary Cr/Mo–Si phase diagram was developed for the alloy series including an estimation of the stability range of the metastable σ phase.

Oxidation properties at 1200 °C in air: 1) For all investigated Mo contents, nitridation of the A2 solid solution was fully inhibited. 2) The oxide scale adhesion was improved by Mo addition. For Mo >25 at.%, no spallation was observed. 3) Below a certain phase fraction and distribution, the A15 phase is prone to internal oxidation. 4) An increased amount of A15 can lead to the formation of a continuous SiO_2 scale beneath the Cr_2O_3 external oxide layer. The continuous internal SiO_2 layer prevents further internal oxidation of the Si in the A15 phase. 5) Evaluation of TGA data using the paralinear law suggests that the parabolic growth rate, k_p, and volatilization rate, k_v, of Cr_2O_3 are reduced by adding 10–25 at.% Mo.

A predictable and stable oxidation behavior was achieved for Cr–25Mo–8Si. Nitridation of the solid solution phase and internal oxidation of the intermetallic A15 phase were inhibited during exposure up to 100 h at 1200 °C in flowing synthetic air, making the Cr–25Mo–8Si composition of great interest for further study.

4. Experimental Section

Synthesis of the Alloy

Chromium (Cr > 99.95 wt%, PLANSEE), silicon (Si > 99.999 wt%, GfE), and molybdenum pieces (Mo > 99.97 wt%, PLANSEE) were used to produce a CrMoSi alloy series (Mo= 10–40 at.% and Si = 8 at.%) via arc melting. The overall mass of each produced ingot was 7 g (resulting in ellipsoidal buttons of ca. 15x10x8 mm). The elements were weighed with a high precision balance (Mettler Toledo XP205DR/M), with a deviation of 1 mg of the calculated mass. To compensate for Cr loss during the arc melting process, 1 wt% excess Cr was added to each composition. A mini arc melting system MAM-1 (Edmund Bühler GmbH) was used to perform the arc melting process. The ingots were produced on a water-cooled Cu crucible using a nonconsumable tungsten electrode. The melting chamber was alternately evacuated and purged with Ar 5 times before melting. Also, Zr was melted twice before melting the actual sample to get any residual oxygen in the chamber. In a first step, Cr and Mo were prealloyed and subsequently Si was added. The ingots were remelted at least 5 times and flipped each time to ensure homogeneity.

Annealing

Annealing of the arc-melted samples was performed to 1) homogenize any concentration gradients and 2) achieve uniform formation of $(Cr,Mo)_3Si$ precipitates inside the (Cr,Mo)-solid solution matrix. All anneals were performed in a tube furnace (Carbolite type STF 14/450) in a flowing Ar/5 vol%H2 atmosphere using an alumina tube. The samples were placed in an alumina crucible. A second crucible was used containing Ti chips to get residual oxygen during the anneal. All samples were rapidly quenched in water after the desired annealing time was achieved, resulting in brief exposure to air while hot. This oxidized layer was ground off before further analysis or exposure. Microstructures resulting from annealing temperatures of 1200 and 1350 °C (for 100 h) were compared. To further investigate the stability range of the σ phase, an anneal at 1450 °C (for 20 h) was also included.

Microstructure and Phase Analysis

For microstructure and phase analysis of the AC and AN states, as well as after oxidation, samples were embedded in a graphite-filled phenolic mounting compound, using a hot press (25 kN, 180 °C, 7 min). Prior to embedding, the oxidized samples were coated with an Au layer (≈4 nm) by plasma vapor deposition and afterward Ni-plated using an electrochemical bath. The embedded samples were ground using P320, P500, P800, P1200, and P2400 grit SiC paper with water before final polishing with 3 µm and 1 µm diamond suspensions and a lubricant consisting of ethylene glycol, ethanol, and isopropyl alcohol.

XRD (Bruker D8 Advance) and the "ICDD" materials database were used to identify the phases and determine the lattice parameters (LPs) of the cubic (Cr,Mo)-solid solution and the intermetallic $(Cr,Mo)_3Si$ phase. The XRD system was equipped with a Cu cathode as the X-ray source using a Ni filter to block the kβ-line of Cu. Absorption correction for thick samples was performed as described in ref. [38]. A z-scan was performed before every measurement to minimize the z-position error.

Electron microscopy (Hitachi FlexSEM 1000II) was used to generate back-scattered electron (BSE) images of the microstructures and wavelength-dispersive X-ray spectroscopy (WDS) was used to measure the overall and local phase compositions and generate semiquantitative elemental distribution maps. The BSE images and the software "ImageJ.JS" were used to determine the fractions of the different phases. The phase compositions of all samples were determined using at least ten WDS measurements per phase. The overall composition was calculated by taking into account the observed area fraction of each phase as determined via "ImageJ." In the case of a single-phase material, the overall composition was determined using a WDS grid measurement and averaging over 121 points.

High Temperature Exposure and Thermogravimetry

To investigate and compare the oxidation and nitridation behavior of the alloys, annealed cuboids (ca. 4x4x3.5mm^3), cut by electrical discharge machining and then ground using SiC paper up to P1200 grit, were exposed in a box furnace (Nabertherm HTC 03/15) in static laboratory air at 1200 °C. Prior to the exposure

the cuboids were ultrasonically cleaned with acetone and isopropyl alcohol. The ramp from RT to 1200 °C was 10 K·min^{-1} and the samples were furnace cooled after 50 h.

To follow mass changes accurately, samples annealed at 1350 °C in Ar/5%H2 for 100 h and then quenched were additionally measured in a TGA system in flowing (205 cm·min^{-1}) dry synthetic air (80% N_2, 20% O_2) at 1200 °C (Furnace Nabertherm type HT 04/17). The mass change was continuously measured (Precision balance M25D-V, Sartorius) during the 100 h high-temperature exposure with one weight measurement per minute. The samples were connected to the balance via a vertical hanging sample holder system consisting of Pt wire and alumina tubes placed in the tube furnace. The linear Pt volatilization was taken into account by performing a reference measurement (empty sample holder) before loading the actual sample. The ramp rate was adjusted to prevent exceeding 1200 °C (RT to 1100 °C at 15 °C·min^{-1}, 1100–1190 °C at 10 °C·min^{-1}, and 1190–1200 °C at 5 °C·min^{-1}). After 100 h exposure at 1200 °C, the furnace was shut down and the sample was furnace cooled under continuing gas flow. Reproducibility was confirmed by repeating most of the experiments.

Acknowledgements

The authors gratefully acknowledge the German Federal Ministry for Economic Affairs and Climate Action (BMWK) for the financial support of the project under grant number 20E2125 based on a decision of the German Bundestag. The authors thank Dr. G. Schmidt from DECHEMA-Forschungsinstitut (DFI) for the EPMA-WDS measurements and the members of the DFI workshop Heinrich Kopietz, Yvonne Hohmann and Jano Bender for electrical discharge machining of the samples. Open Access funding enabled and organized by Projekt DEAL.

Conflict of Interest

The authors declare no conflict of interest.

Data Availability Statement

The data that support the findings of this study are available from the corresponding author upon reasonable request.

Keywords

alloy development, chromium, high-temperature oxidation, molybdenum,

refractory metal alloys

References

[1] H. Harada, "High Temperature Materials for Gas Turbines: The Present and Future," in Congress, Proceedings of the International Gas Turbine IGTC2003Tokyo KS-2, Tokyo, 2003.

[2] J. H. Perepezko, "The Hotter the Engine, the Better," Science, vol. 326, pp. 1068-1069, 2009.

[3] J. Wadsworth, T. G. Nieh and J. J. Stephens, "Recent advances in aerospace refractory metal alloys," International Materials Reviews, vol. 33, no. 3, p. 131, 1988.

[4] Y. F. Gu, H. Harada and Y. Ro, "Chromium and Chromium-Based Alloys: Problems and Possibilities for High-Temperature Service," The Journal of The Minerals, Metals & Materials Society, vol. 56, pp. 28-33, 2004.

[5] E. M. Savitskii and G. S. Burkhanov, Physical Metallurgy of Refractory Metals and Alloys, New York: Consultants Bureau, 1970, pp. 16-22; 193-199.

[6] T. M. Pollock and S. Tin, "Nickel-Based Superalloys for Advanced Turbine Engines: Chemistry, Microstructure, and Properties," Journal of Propulsion and Power, vol. 22, no. 2, pp. 361-374, 2006.

[7] DERA, "Raw Material Price Monitor," Federal Institute for Geosciences and Natural Resources, 2023.

[8] I. Murris, Y. P. Jacob, V. A. C. Haanappel and M. F. Stroosnijder, "High-Temperature Oxidation Behavior of Chromium: Effect of Different Batches," Oxidation of Metals, vol. 55, no. 3/4, 2001.

[9] S. Mathieu, „On the Oxidation and Nitridation of Chromium at 1300 °C,“ Oxidation of Metals, Nr. 74, p. 79–92, 2010.

[10] A. Solimani-Dorcheh and M. C. Galetz, "Challenges in Developing Oxidation-Resistant Chromium-Based Alloys for Applications Above 900°C," The Journal of Minerals, Metals & Materials Society, vol. 68, p. 2793–2802, 2016.

[11] H. Johanse and G. Asai, "Room-Temperature Ductile Chromium," Journal of The Electrochemical Society, vol. 101, no. 12, pp. 604-612, 1954.

[12] O. N. Carlson, L. L. Sherwood and F. A. Schmidt, "The effect of low percentage alloying additions on the ductility of iodide chromium," Journal of the less-common metals, vol. 6, pp. 439-450, 1964.

[13] K. Ioroi, Y. Aono, X. Xu, T. Omori and R. Kainuma, "Melting point of pure Cr and phase Equilibria in the Cr-Si binary system," Journal of Phase Equilibria and Diffusion, vol. 43, pp. 229-242, 2022.

[14] A. Solimani-Dorcheh and M. C. Galetz, "Oxidation and Nitridation Behavior of Cr–Si Alloys in Air at 1473 K," Oxidations of Metals, vol. 84, pp. 73-90, 2015.

[15] Y. Aono, T. Omori and R. Kainuma, "Microstructure and high-temperature strength in Cr–Si binary alloys," Intermetallics, vol. 112, p. 106526, 2019.

[16] P. Pfizenmaier, A. S. Ulrich, U. Glatzel and M. C. Galetz, "Tensile Creep Properties of Cr-Si Alloys at 980 °C in Air - Influence of Ge and Mo Addition," Metals, vol. 11, no. 7, pp. 1072-1080, 2021.

[17] A. Solimani, T. Nguyen, J. Zhang, D. J. Young and M. Schütze, "Morphology of oxide scales formed on chromium-silicon alloys at high temperatures," Corrosion Science, vol. 176, p. 109023, 2020.

[18] S. V. Raj, "An evaluation of the properties of Cr,Si alloyed with Mo," Materials Science and Engineering A, vol. 201, pp. 229-241, 1995.

[19] W. Trzebiatowski, H. Ploszek and J. Lobzowski, "X-ray Analysis of Chromium-Molybdenum and Chromium-Tungsten Alloys," Analytical Chemistry, vol. 19, no. 2, pp. 93-95, 1947.

[20] A. S. Ulrich, P. Pfizenmaier, A. Solimani, U. Glatzel and M. C. Galetz, "Improving the oxidation resistance of Cr-Si-based alloys by ternary alloying," Corrosion Science, vol. 165, p. 108376, 2020.

[21] F. Hinrichs, A. Kauffmann, A. S. Tirunilai, D. Schliephake, B. Beichert, G. Winkens, K. Beck, A. S. Ulrich, M. C. Galetz, Z. Long, H. Thota, Y. Eggeler, A. Pundt and M. Heilmaier, "A novel nitridation- and pesting-resistant Cr-Si-Mo alloy," Corrosion Science, vol. 207, p. 110566, 2022.

[22] L. Pandelaers and R. Schmid-Fetzer, Landolt-Börnstein: Ternary Alloy Systems, Subvolume E, Refractory Metal Systems, Springer, 2010, pp. 182-191.

[23] H. Wu, C. Li, C. Guo und Z. Du, „Experimental determination of the isothermal sections and the liquidus surface projection of the Mo-Si-Cr ternary system," Journal of Alloys and Compounds, Nr. 922, p. 166164, 2022.

[24] H. Wu, C. Li, C. Guo and Z. Du, "Thermodynamic assessment of the Cr-Mo-Si ternary system," Calphad, no. 83, p. 102631, 2023.

[25] E. Rudy and H. Nowotny, "A σ-phase in the chromium-molybdenum-silicon system," Chemical Monthly, vol. 105, pp. 156-168, 1974.

[26] M. Venkatraman and J. P. Neumann, "The Cr-Mo (Chromium-Molybdenum) System," Bulletin of Alloy Phase Diagrams, vol. 8, no. 3, pp. 216-220, 1987.

[27] H. Nowotny, H. Schroth, R. Kieffer and F. Benesovsky, "Der Aufbau einiger Silizidsysteme von Übergangsmetallen," Monatshefte für Chemie, vol. 84, pp. 579-584, 1953.

[28] A. S. Ulrich, P. Pfizenmaier, A. Solemani, U. Glatzel and M. C. Galetz, "Strengthened Cr-Si-base alloys for high temperature applications," International Journal of Refractory Metals & Hard Materials, vol. 76, pp. 72-81, 2018.

[29] M. Guerain, F. Rakotovao, S. Y. Brou, G. Bonnet, B. Panicaud, J. L. Grosseau-Poussard and P. Goudeau, "Stress release in a-Cr 2 O 3 oxide thin films formed on Ni30-Cr and Fe47-Cr alloys," Journal of Alloys and Compounds, vol. 718, pp. 223-230, 2017.

[30] P. Kofstad and K. P. Lillerud, "On High Temperature Oxidation of Chromium: II . Properties of Cr2O3 and the Oxidation Mechanism of Chromium," Journal of The Electrochemical Society, vol. 127, no. 11, pp. 2410-2419, 1980.

[31] E. Polman, T. Fransen and P. J. Gelings, "Oxidation Kinetics of Chromium and Morphological Phenomena," Oxidation of Metals, vol. 32, no. 5-6, pp. 433-447, 1989.

[32] L. Latu-Romain, Y. Parsa and Y. Wouters, "Spallation study of chromia scales thermally grown on pure chromium in synthetic air," Material Characterization, vol. 152, pp. 58-66, 2019.

[33] L. Latu-Romain, Y. Parsa, S. Mathieu, M. Vilasi, M. Ollivier, A. Galerie and Y. Wouters, "Duplex n- and p-Type Chromia Grown on Pure Chromium: A Photoelectrochemical and Microscopic Study," Oxidation of Metals, vol. 86, pp. 497-509, 2016.

[34] A. S. Ulrich, U. Glatzel and M. C. Galetz, "Discontinuities in Oxidation Kinetics: A New Model and its Application to Cr–Si Base Alloys," Oxidation of Metals, vol. 95, pp. 445-465, 2021.

[35] W. Hagel, "Factors Controlling the High-Temperature Oxidation of Chromium," Transactions of American Society for Metals, vol. 56, pp. 583-599, 1963.

[36] C. A. Barrett and A. F. Presler, "Corest: A fortran computer program to analyze paralinear oxidation behavior and its application to chromic oxide forming alloys," National Aeronautics and space administration, Washington D.C., 1976.

[37] J. L. Smialek, "Simplified Paralinear Oxidation Analyses," High Temperature Corrosion of Materials, vol. 99, pp. 431-457, 2023.

[38] J. B. Nelson and D. P. Riley, "An experimental investigation of extrapolation methods in the derivation of accurate unit-cell dimensions of crystals," Proceedings of the Physical Society, vol. 57, pp. 160-177, 1945.

[39] A. B. Gokhale and G. J. Abbaschlan, "The Mo-Si (Molybdenum-Silicon) System," Journal of Phase Equilibria, vol. 12, no. 4, pp. 493-498, 1991.

3.4 Cr-Based High Temperature Alloys – The Strengthening Effect of Molybdenum on Chromium-Silicon Alloys

Published in International Journal of Refractory Metals and Hard Materials, 132 (2025), 107287.
DOI: 10.1016/j.ijrmhm.2025.107287

Authors
Lisa Zander[1], Michael Kerbstadt[1], Emma M. H. White[1], Mathias C. Galetz[1]

[1] DECHEMA Research Institute, Theodor-Heuss-Allee 25, 60486 Frankfurt a.M., GER.

Abstract
This study investigates the effect of molybdenum in novel Cr-xMo-8Si alloys regarding hardness, fracture toughness and specific strength. With increasing Mo content in Cr-xMo-8Si alloys the hardness at room temperature (RT) linearly increases, with the dominant effect being solid solution hardening. Compression tests at temperatures between 23 and 900 °C show that the strength of Cr-xMo-8Si alloys also increases with increasing Mo content. The strength of Cr-25Mo-8Si (with a maximum specific strength of 170±24 $N \cdot m \cdot g^{-1}$) is comparable to IN718 for temperatures up to 700 °C, but remains stronger up to the maximum tested temperature of 900 °C. However with Mo additions, the ductile to brittle transition (DBTT) regime is shifted to higher temperatures when compared to the reference material. The fracture toughness at RT ranges between 4 to 10 $MPa \cdot m^{0.5}$. While it initially drops with increasing Mo content, it starts to increase for Mo ≥ 25 at.%, which can be explained by a grain refining effect of Mo benefitting the fracture toughness. From the results, strategies for increasing the low fracture toughness at RT of this class of novel alloys are derived, providing a path forward to enabling applications making use of their outstanding high temperature properties.

1. Introduction

New alloy systems for high-temperature applications must surpass the current standard of nickel-based superalloys. Such alloys require a balanced property profile featuring high mechanical strength, creep, and corrosion resistance

beyond 1100 °C, along with reasonable ductility at lower temperatures for good workability and fracture toughness.

One approach for developing new high-temperature (HT) alloys focuses on refractory metal-based systems, which are attractive due to their high strength at elevated temperatures resulting primarily from their high melting points. Notably, Mo- and Nb-based systems have been extensively investigated, as they exhibit excellent mechanical strength at high temperatures [1, 2, 3, 4, 5, 6, 7, 8]. However, these materials often suffer from insufficient oxidation resistance, primarily due to the formation of volatile oxides for Mo or catastrophically fast growing oxides for Nb, leading to an imbalanced property profile [1, 9, 10, 11].

In the last ten years, chromium-based alloys have drawn more attention as they offer a more balanced property profile, offering an adequate mechanical strength for service temperatures above 1100 °C, while also ensuring an acceptable oxidation behavior that is intrinsic to the base alloy up to about 1200 °C [12, 13, 14]. Cr provides several advantages, including low density, high melting point (Figure 1), high thermal conductivity, availability, and cost-effectiveness [15, 16]. Alloying strategies have already helped to manage some of the challenges of Cr-based alloys, such as the formation of volatile species and nitrides at elevated temperatures [12, 13, 14, 17, 18, 19, 20]. Silicon contents up to 15 at.% have been shown to play a critical role in reducing nitridation, oxidation and volatilization rates of Cr-based alloys and promoting precipitation hardening by forming the intermetallic phase Cr_3Si with the A15 structure [21, 22]. While increasing the amount of intermetallic phase in the Cr solid solution matrix generally improves oxidation resistance and specific strength, excessive amounts can lead to increased brittleness, [22, 23, 24, 25] diminishing the overall benefits. Therefore, to maintain reasonable workability and toughness, the quantity and distribution of the intermetallic phase must be controlled. Molybdenum has also been identified as a vital alloying element that can further enhance the high-temperature mechanical properties of Cr by solid solution hardening and mitigating the nitridation of the chromium matrix [26, 27, 12, 13, 14]. Partial substitution of Cr with Mo decreases the Si solubility in the solid solution [14] and up to 3wt.% Mo in Cr has been shown to lower the DBTT, which is known to be a major challenge for Cr-based alloys [28].

An earlier study demonstrated that the addition of Mo improves the oxidation behavior of Cr-xMo-8Si alloys in air at 1200 °C, with the most promising results at a maximum concentration of 25 at.% Mo in Cr-xMo-8Si [14]. The current study investigated the mechanical properties as a function of the Mo content and temperature. For this purpose the Vickers hardness of several Cr-Mo-Si alloys was measured and the fracture toughness was determined. The aim was to

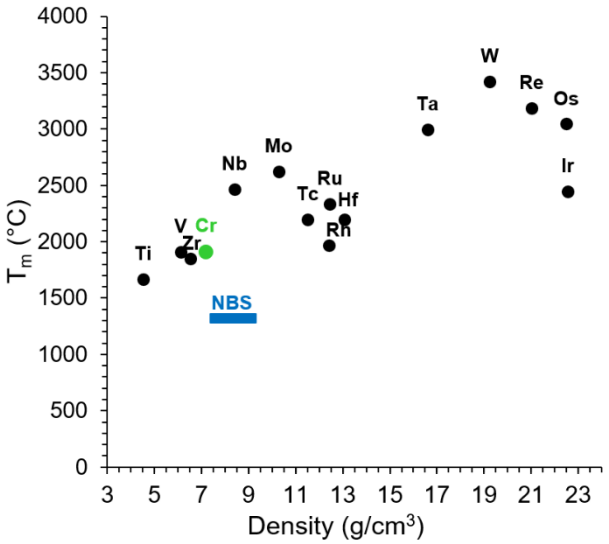

Figure 1: Melting temperature vs. density of refractory metals compared to Ni-based superalloys (NBS) [48, 50]

understand which of the multiple Mo effects impacts the hardness and toughness the most. The specific strength at low and high temperatures was determined by compression tests and compared to other relevant alloy systems.

2. Experimental methods and analytics

2.1 Synthesis of the alloys

All investigated alloys were produced via arc-melting using pure elements as initial materials: chromium (Cr > 99.95 wt.%, PLANSEE), silicon (Si >99.999 wt.%, GfE) and molybdenum (Mo > 99.97 wt.%, PLANSEE). Buttons with a mass of 7 g were produced using the mini arc-melting system MAM-1 (Edmund Buehler GmbH). Larger buttons (150 g) were produced using the arc melter AM 200 (Edmund Buehler GmbH). A high precision balance (Mettler Toledo XP205DR/M) was used to weigh the pure elements. Cr was added in 1 wt.% excess to compensate for Cr loss during the melting process. The melting

took place in an inert Ar atmosphere on a water-cooled Cu plate. A piece of Zr was melted as an oxygen getter to remove any residual oxygen in the melting chamber before melting the sample. All buttons were remelted five times and flipped over each time to establish homogeneity. Unless stated otherwise atomic percent compositions are used throughout this research article.

2.2 Annealing

All arc-melted samples were heated in a tube furnace (Carbolite type STF 14/450) in a flowing Ar/5 vol.%H_2 atmosphere to homogenize concentration gradients and anneal the microstructure. Ti chips were placed next to the samples, facing the gas flow to getter residual oxygen during the anneal. Small 7 g buttons initially produced for the hardness tests were annealed for 100 h at 1200 °C and manually quenched in water after the anneal. Larger buttons (150 g) produced for compression tests underwent optimized annealing conditions, as derived from [14], with the goal of optimizing the distribution and size of the intermetallic A15 phase in the A2 solid solution matrix. Compositions with Mo contents < 25 at.% were annealed at 1450 °C for 20 h in a first step, while samples containing ≥ 25 at.% Mo were annealed at 1350 °C for 100 h (to avoid stabilization of the σ phase in this step the annealing temperature was lowered). All compositions were then annealed at 1200 °C for 100 h in a second step. Due to the size of the ingots, manual water quenching was not possible and the samples were furnace cooled to RT.

2.3 Microstructural analysis

For microstructural analysis of the annealed and compression-tested samples and for hardness tests, samples were embedded in a graphite-filled phenolic mounting compound using a hot press (25 kN, 180 °C, 7 min). The embedded samples were ground using P320, P500, P800, P1200, and P2400 grit SiC paper with water before polishing with 3 µm and 1 µm diamond suspensions and a lubricant consisting of ethylene glycol, ethanol, and isopropyl alcohol. For electron backscatter diffraction (EBSD) measurements, a final 0.02 µm SiO2 suspension was used for polishing. The compression-tested samples were embedded and ground so that the longitudinal cross-section at the middle of the cylinder was observable. Macroscopic images were recorded with a

stereomicroscope (Leica MZ16 A) for the compressed samples. Scanning electron microscopy (SEM, Hitachi FlexSEM 1000II) was used to produce back-scattered electron (BSE) images to observe elemental contrast in the microstructures. Identification of phases was performed via X-ray diffraction (XRD) “Bruker D8 Advance“ and quantitative elemental compositions were checked with a JEOL JXA-8100 electron probe microanalyzer using quantitative wavelength dispersive X-ray spectroscopy (EPMA/WDS) as described in [14]. EBSD analysis was performed with a “SU5000” SEM from Hitachi equipped with the “Velocity” EBSD system from EDAX. A sample tilt angle of 70° was used. The software used to identify the crystal orientation was “OIM v8” from EDAX applying a standard cleanup (Grain CI Standardization, tolerance 5.0, min size 3, Multi Row 1). For phase assignment during EBSD analysis the lattice parameters of Cr (A2) and Cr_3Si (A15) phase as a function of Mo content were taken from [14].

2.4 RT Hardness testing

The RT hardness of the samples was determined using a LEICA VMHT MOT hardness tester using the Vickers method. The diamond pyramid was pressed into the sample using a load of 1 kg (HV1) with an indentation speed of 50 µm/s and a maximum load duration of 15 s. The diameter (d) of the pyramid tip imprint for the samples ranged from 50-75 µm with a minimum distance of 400 µm between indentations. To determine the hardness values of the A2 and A15 phases, a nanoindentation tester TTX NHT2 (Anton Paar Germany GmbH), equipped with a Berkovich tip, was used. An optimum testing force of 25 mN was determined and used for both phases with a loading speed of 50 mN/min (staying at the maximum load for 5 s) and unloading the sample with 100 mN/min. All measurements were performed on annealed, embedded and polished samples. Hardness values were determined by averaging at least ten measurements. To compare the fracture behavior of the alloy series additional Vickers tests were performed at much higher loads (HV30, HV50 and HV100) using hardness tester KB250 from “KB Prüftechnik”. Where applicable, the fracture toughness was estimated as K_I based on the formula given in [29]:

$$\mathrm{K}_I = \frac{F}{(\pi \cdot c)^{3/2} \tan(\alpha)} \quad (1)$$

with F = test load (kg), c = crack length + half of the indentation diagonal length (mm), and α = opening angle of the Vickers pyramid (136°). Units were converted using: $MPa \cdot m^{0.5} = 0.3101\ kg/mm^{1.5}$.

2.5 Compression testing

For compression tests cylinders of 4 mm diameter and 6 mm length were manufactured by electric discharge machining (EDM). Since some compositions did not fail with the maximum load of the testing device (25 kN), additional cylinders of 3 mm diameter and a length of 4.5 mm were manufactured to determine stress-strain curves for each material. Stress-strain plots from both sample types were comparable. Only the full curves are included here. The two end faces of the cylinders were ground with P500 grit SiC paper. The circumferential surface was ground only for the 4 mm cylinders. The initial diameter and length of every sample was determined using a digital caliper. For the compression tests, an “Inspekt 50” (“Hegewald & Peschke Meß- und Prüftechnik GmbH”) compression rig with alumina pushrods was used. A vertical clam shell-type furnace was used to heat the cylinders during the compression. A thermocouple was placed near the surface of the sample to track the real temperature (given values ± 5 °C). All compositions were tested at 23, 300, 500, 700 and 900°C. Random measurements were repeated to ensure reproducibility. The cylinders were placed in the center of the lower pushrod and a preload of 10 N was applied by moving the upper rod downwards. The furnace was closed around the sample and pushrods. During the heating period, the preload was kept constant. At 15 min after the set temperature had reached a constant value, a compressive strain rate of $2.5 \cdot 10^{-4}\ s^{-1}$ was applied. All samples were either compressed until breakage (sudden loss of > 80% load) or the test was aborted at a travel distance of half the sample length. A calibration data set was generated for all tested temperatures by determining the force-length variation for the testing device without a sample. This data was used to correct the travel distance values from the experiments containing a specimen. The engineering stress and strain values were calculated using formulas (2) and (3) [30]. Additionally, the densities of various Cr-xMo-8Si samples were determined by the Archimedes method using a high precision balance (Mettler Toledo XP205DR/M) in order to calculate

the temperature-dependent specific strength using the 0.2% proof stress of the alloys and dividing it by the density.

$$\text{Stress: } \sigma = \frac{F}{A_0} \tag{2}$$

$$\text{Strain: } \varepsilon = \frac{\Delta L}{L_0} \cdot 100 \tag{3}$$

3. Results + Discussion

3.1 Microstructure

The initial microstructure of the alloys is shown in Figure 2, using EBSD including a) the orientation of the grains and b) the average grain size. Increasing Mo in Cr-xMo-8Si decreases the overall grain size by one order of magnitude, ranging from an average of about 450 µm for Cr-8Si to about 50 µm for Cr-25Mo-8Si. It should be noted that Cr-25Mo-8Si was exposed to a lower initial annealing temperature (see 2.2 Annealing section: 1350 °C vs. 1450 °C) to prevent entering the stability regime of the σ phase field [14], so the grain size of Cr-25Mo-8Si is not directly comparable with the other three compositions. On the other hand, a shorter annealing time (20 h vs. 100 h) in the first annealing step may have partially compensated for the effect of a higher temperature for Cr-8Si in terms of grain growth.

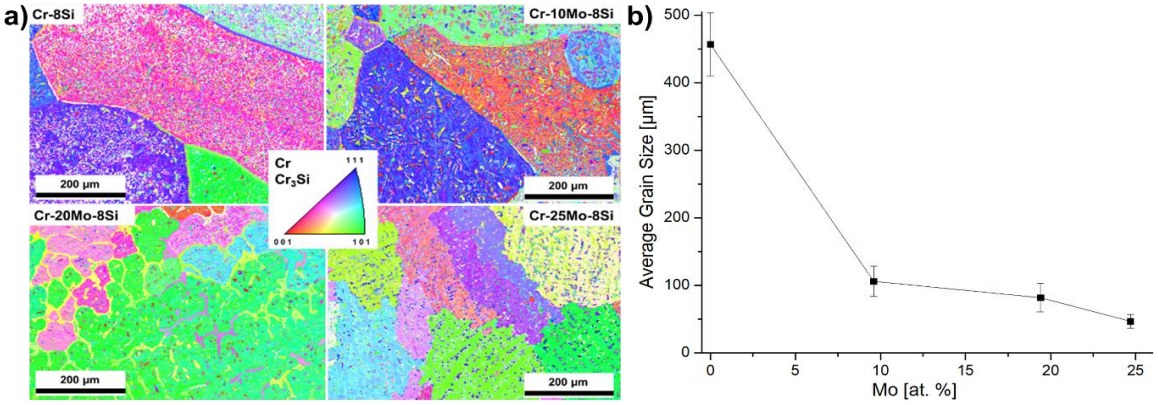

Figure 2: Initial microstructure of the Cr-xMo-8Si series depicted with EBSD imaging showing a) the crystallographic orientation of the grains and b) Grain size depending on Mo content in Cr-xMo-8Si

Apart from the increasing melting temperature of the Cr-xMo-8Si alloy series with increasing Mo content [31], the grain refining effect of Mo on Cr during annealing can also be ascribed to an increasingly non-homogeneous matrix phase in the arc-melted state [14]. A higher density of lattice defects like dislocations and

vacancies is typical in regions of concentration gradients. These defects can act as favorable sites for grain nucleation during annealing at the expense of grain growth. Another aspect that can contribute to grain refinement is the increased amount of A15 phase [14] with higher Mo contents, which also can lead to an increased amount of grain nucleation sites (as also observed in section 3.3 Fracture toughness). For lower Mo contents, grain growth is more dominant during annealing. Not only the size but also the morphology of the grains changed. Interestingly, Cr-8Si and Cr-10Mo-8Si show rather equiaxed grains, while alloys with Mo contents ≥ 20 at.% resulted in microstructures that were more columnar.

In Figure 3 the EBSD rotation angle within one grain of the Cr solid solution matrix (A2) is shown for each composition. It is striking that there are relatively high rotation angles (5-15°) within the A2 matrix of the Cr-8Si alloy, which can be indicative of a higher stress in the matrix and subgrain formation [32]. Along these subgrains, slip can occur during deformation. Mo-containing alloys showing fewer and lower rotation angles (1-5°) indicate deformation would be more difficult for the Mo-strengthened Cr solid solution.

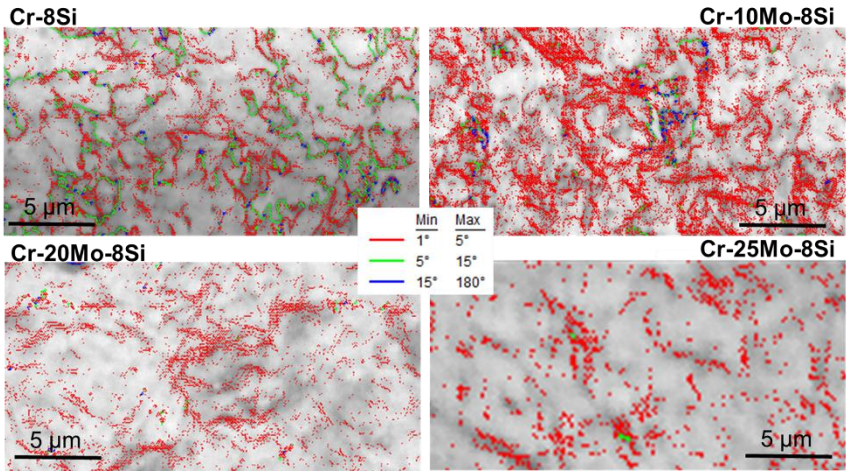

Figure 3: EBSD boundary rotation angle within one grain of the Cr solid solution matrix (A2)

3.2 Hardness

To investigate the influence of Mo on the RT hardness of the Cr-xMo-8Si system, an alloy series with x = 0, 10, 20, 25, 40 at.% was produced. The annealed alloys formed a Cr solid solution matrix (A2) and an intermetallic phase (A15). RT hardness of the overall microstructure versus the individual phases was determined via the Vickers method (HV1) and nanohardness testing with a

Berkovich tip (Figure 4). An additional comparison between different annealing types was added to investigate the influence of A15 distribution on the overall hardness. To better distinguish the different effects of Mo on the overall hardness

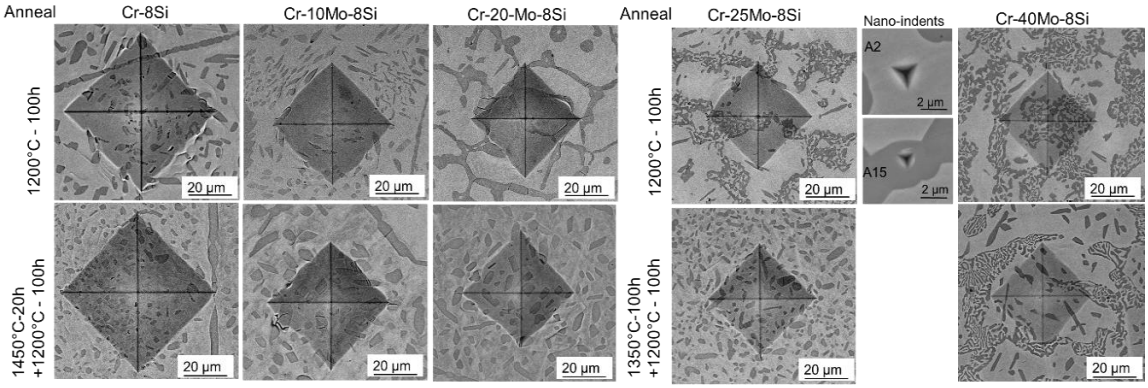

Figure 4: BSE pictures of Vickers imprints of the Cr-xMo-8Si alloy series and an example of nano-indentations. The bright matrix is A2, while darker precipitates are the intermetallic A15 phase. Top row: non-optimized anneal; bottom row: optimized two step anneal with improved number density of A15.

of the alloy, Cr-25Mo-8Si was chosen to be compared with the single-phase (A2) alloys: Cr-26Mo-3Si (composition of A2 in Cr-25Mo-8Si [14]), Cr-3Si and pure Cr. All of the additional materials were also arc-melted and annealed at 1200 °C prior to hardness testing.

Before discussing the influence of Mo on the hardness of Cr-based Cr-Mo-Si alloys it is important to recognize the complexity of superimposed effects that can lead to hardening or softening in this system. In [14] the influence of Mo content on the Mo distribution, Si solubility and the amount of A15 phase was extensively analyzed. It was observed that Mo substitutes Cr in the A2 and A15 phases. The higher the overall Mo content, the more Mo enrichment occurred in the A2 phase as compared to A15. The addition of Mo decreases the Si solubility in both phases and leads to an increased amount of A15. Thus, for the investigated alloy series, it can be expected to see an increased hardness with increasing Mo content due to solid solution hardening of the A2 phase and an increased amount of the intermetallic phase. At the same time the decreased solubility of Si, especially in the solid solution matrix, can theoretically improve ductility and fracture toughness [25, 33].

In Figure 5 the RT hardness of the bulk material and the respective individual A2 and A15 hardness values of the Cr-xMo-8Si alloy series is plotted versus the Mo

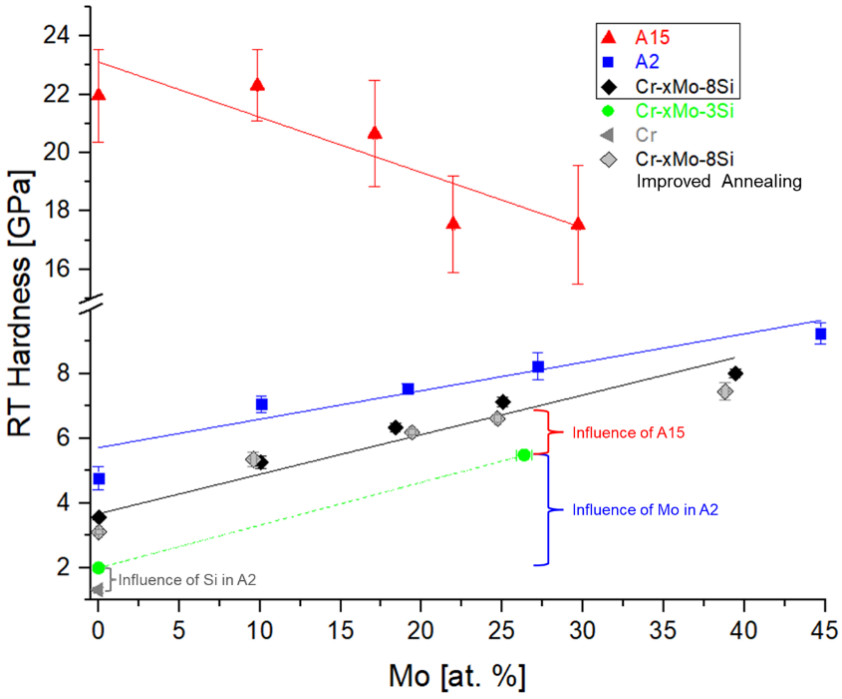

Figure 5: RT hardness (micro and nano hardness) vs. overall Mo content and Mo content per phase (A2 or A15)

content. The overall hardness of the Cr-xMo-8Si alloy increases with increasing Mo content. Hardness values vary between 3.6(1) GPa for Cr-8Si and 8.0(1) GPa for Cr-40Mo-8Si. The comparison of pure Cr and Cr-3Si gives information on the solid solution hardening effect of Si dissolved in the A2 matrix. An increase in hardness of 51±6% was achieved by the addition of 3 at.% Si to Cr. The strengthening effect of Si in Cr was extensively studied by Aono et al. [22], who showed that the proof stress increases almost proportionally with the Si content in the Cr solid solution. Similar observations have been made for the Mo-Si system [34]. Comparing Cr-3Si with the single-phase Cr-26-Mo-3Si alloy gives information on the solid solution hardening effect of Mo in the Cr system. Here, a hardness increase of 174±10% was determined. Comparison of the single-phase Cr-26Mo-3Si and the two-phase material Cr-25Mo-8Si (containing 28±1 area % of A15 phase [14]) showed an increase in hardness of 30±1% due to the A15 phase. This suggests that the dominant hardening mechanism is solid solution hardening of the matrix phase (A2), while precipitation hardening via the A15

phase has a relatively minor contribution. This behavior may drastically change for higher Si contents that are closer to the regime of a eutectic microstructure as described in [22]. Using an improved two step anneal, as derived from the data of [14], to alter the size and distribution of the intermetallic phase (see Figure 4), did not lead to a significant difference in the precipitation hardening effect (see Figure 5), which confirms that the matrix phase dominates the hardness. No cracks were initiated in the A2 matrix phase during Vickers testing with loads of 1 kg. However, larger area fractions of A15 phase did show isolated cracking, while finer A15 precipitates were more resistant to cracking. This suggests that optimized annealing could have a beneficial influence on the fracture behavior of the A15 phase. Evaluation of the individual phases as determined using nanohardness showed that A15 hardness values are up to ≈4.5 times higher than the A2 phase for each composition. With increasing Mo content, the difference in hardness between the A15 and A2 is lowered to around 2 times higher. The more substantial enrichment of Mo in the A2 with increasing overall Mo content, as observed in ref. [14], leads to an increased hardening effect in the A2. Meanwhile, the intermetallic phase decreases in hardness with increasing Mo content. Due to the small size of the A15 precipitates, the hardness values show a rather large deviation, and a linear trend can only be roughly estimated. Nevertheless, a decrease in hardness of the A15 phase with increased Mo content is clear and can be explained by the decreased Si amount (which is observed in both phases) with increasing Mo content, as described in [14]. According to the binary Cr-Si and Mo-Si phase diagrams [35, 36] Mo should favor a more stoichiometric, and thus higher, Si content in the A15 phase. That suggests that the presence of Mo either induces antisite defects (substitution of Si by Cr) or constitutional vacancies, which both can explain lower hardness. The finding in ref. [33] stating that the substitution of Cr with Mo can increase the fracture toughness of Cr_3Si correlates with the observations of a lower hardness. In A2 the effect of solid solution hardening by Mo has a stronger influence on hardness than the reduced Si solubility. Thus, the trend shows a linear increase in hardness for the solid solution phase. Note that due to differing evaluation methods, the results from nanohardness can be 10 to 30% larger than that of micro-hardness [37], explaining the difference of roughly 30 % between the hardness of Cr-26Mo-3Si

as determined by micro-hardness versus the respective phase hardness of A2 as determined by nanohardness.

3.3 Fracture toughness

In order to get an impression of the fracture toughness, Vickers tests at higher loads were performed (HV30) with the samples that underwent an optimized two step anneal. The tests resulted partly in cracking of the A2 matrix, from which an estimation of the fracture toughness as described in [29] was possible. Figure 6 depicts an overview of some of the generated cracks. No cracks were observed in the Cr-8Si reference sample, while the alloys containing Mo in the Cr-xMo-8Si series showed cracks emerging from the corners of the Vickers imprint as described in [29]. A single-phase material Cr-26Mo-3Si (the composition of A2 in the Cr-25Mo-8Si alloy) was included to measure the influence of Mo on fracture toughness of the A2 matrix. Similarly to Cr-8Si no cracks were observed in the Cr-26Mo-3Si material. The fracture toughness was determined as KI as described in the experimental section. Where no cracks were observed the method was labeled as not useful for fracture toughness determination and the K_I value can be expected to be >10 MPa·m$^{0.5}$ (the largest value determined from the test). Formula (1) allows inserting a crack length of 0 mm so that c is just half of the indentation diagonal length, which theoretically gives vales for K_I of 13 and

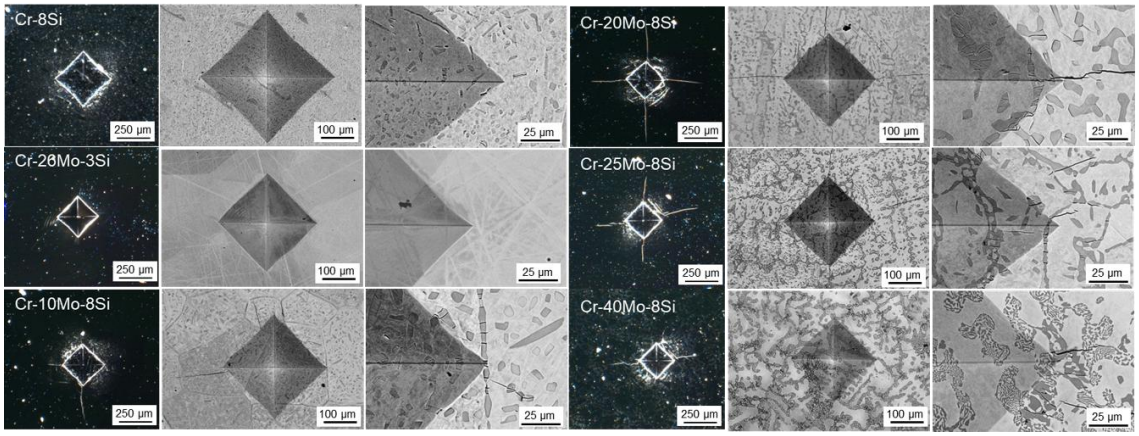

Figure 6: HV30 Vickers imprints using stereomicroscope and SEM images (material contrast mode - bright matrix = A2, darker precipitates = intermetallic A15 phase)

19 MPa·m$^{0.5}$ for Cr-8Si and Cr-26Mo-3Si, respectively. This would suggest an increase in toughness by adding Mo to the A2 matrix. All determined K_I values (Table 1) are also plotted in Figure 7 for a better comparison. Also literature data

from refs. [25, 33] were included for comparison, showing that fracture toughness for Cr-Si alloys decreases with increasing A15 content. In this work, the fracture toughness in the Cr-xMo-8Si system decreases from >10 to ≈4 MPa·m$^{0.5}$ for Cr-20Mo-8Si but starts to increase again to 10 MPa·m$^{0.5}$ for higher Mo contents. This implies that not only does the Mo content in the A2 and A15 phases influence the fracture toughness, but the overall microstructure changes it also. While Mo refines the grain size (Figure 2 (b)), also the size and distribution of the A15 phase is altered. For Mo contents ≥ 25 at.% the A15 phase partly evolves out of a σ

Table 1: K_I values determined via Vickers testing including literature data from [25, 33]

This work				Literature (Cruse et al.)		
Material (at.%)	A15 %	$K_{I\,(}$MPa·m$^{0.5}$)	c (mm) HV30	Material (at.%)	A15 %	$K_{I\,(}$MPa·m$^{0.5}$)
Cr-8Si	19 ± 1	> 10	no cracks	Cr*	0	12.6 ± 1.4
Cr-10Mo-8Si	23 ± 1	5.2 ± 0.7	0.39 ± 0.12	Cr-7Si*	25	7.1 ± 3.4
Cr-20Mo-8Si	26 ± 2	3.7 ± 0.3	0.49 ± 0.09	Cr-15.5Si	50	7.4 ± 0.2
Cr-25Mo-8Si	28 ± 1	6.1 ± 0.4	0.36 ± 0.05	Cr-17Si	60	6.6 ± 0.8
Cr-40Mo-8Si	35 ± 2	10.1 ± 1.2	0.25 ± 0.07	Cr-18.6Si	75	5.9 ± 0.9
Cr-26Mo-3Si	0 ± 0	> 10	no cracks	Cr-25Si	100	2.8 ± 1
*Via three point bending/no cracks with Vickers				Cr-32.2-25Si	100	3.0 ± 0.3

phase (present in the as-cast state [14]), which decomposes to A2 and A15 in the annealing step and leads to a fine local eutectoid microstructure, especially predominant for Cr-40Mo-8Si (see Figure 6). Both of these features seem to be beneficial for fracture toughness. The single-phase material Cr-26Mo-3Si had superior fracture toughness as compared to the respective two-phase material Cr-25Mo-8Si, showing that the intermetallic A15 phase limits and decreases the fracture toughness overall. Thus, the desired minimum of 15 MPa·m0.5 cannot be reached with the two-phase Mo-containing alloys of the current study. Finer grain sizes may, however, provide a path to reaching 15 MPa·m$^{0.5}$ with further optimization.

Some compositions were chosen to be tested at even higher Vickers loads of HV50 and 100. In Figure 8 the Vickers imprints of a) Cr-8Si (A2+A15), b) Cr-25Mo-8Si (A2+A15) and c) Cr-26Mo-3Si (single-phase A2) are compared using SEM images. In some images, BSE mode was used to highlight A2 (bright matrix) versus A15 (darker precipitate). Reference alloy Cr-8Si (Figure 8 a) still showed no crack formation inside the BCC matrix. Higher magnification of the edge of the imprint shows that the A15 precipitates of the Cr-8Si sample all show crack

formation within and near the imprint. The cracks do not propagate from the intermetallic phase across the interface and into BCC matrix showing that the A2

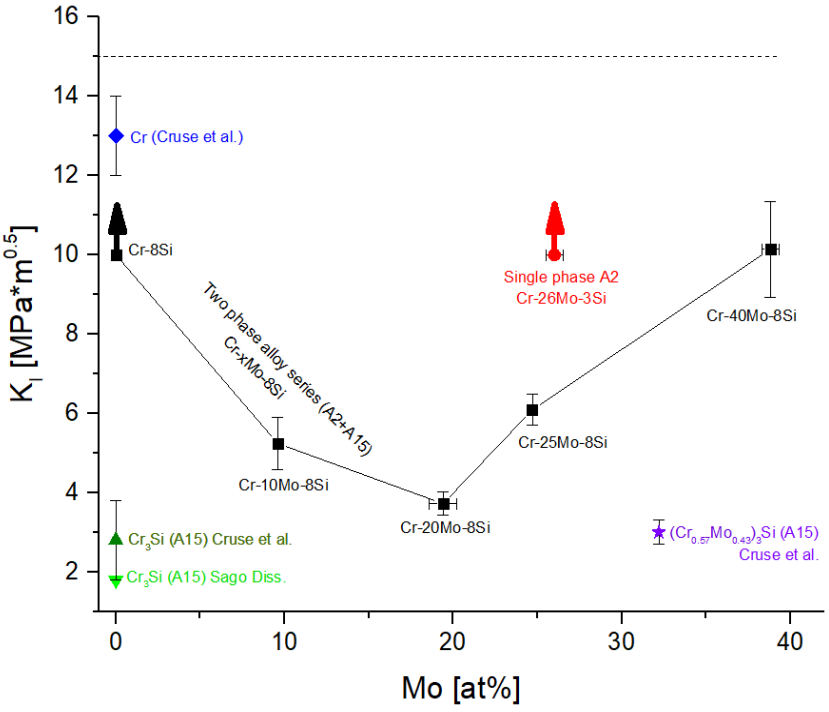

Figure 7: Fracture toughness determined from hardness testing in dependance of composition; including literature data from [25, 33, 51]; Cr-8Si and Cr-26Mo-3Si did not show cracking

matrix itself provides reasonable fracture toughness even at low temperatures. The Cr-25Mo-8Si alloy does show severe crack formation in the A2 matrix when tested with HV50. Differing crack formation and propagation in Cr-25Mo-8Si was observed as depicted in Figure 8 b). Some cracks were isolated inside the A15 phase, while others cut through both phases. Using testing loads of 100 kg resulted in cracks running parallel to each other within the A2 matrix. This is

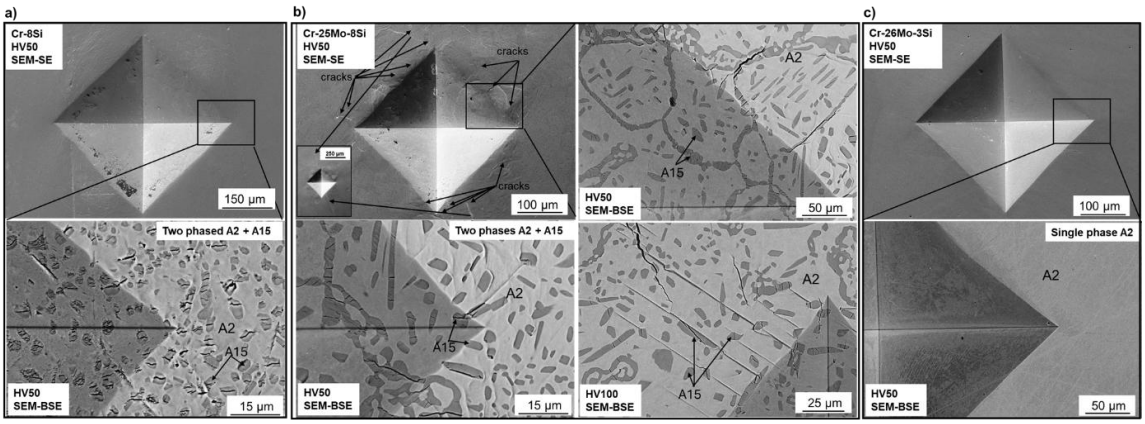

Figure 8: SE- and BSE-SEM images of Vickers imprints of a) Cr-8Si, b) Cr-25Mo-8Si and c) Cr-26Mo-3Si alloys.

typical for cracks moving along screw dislocations. When encountering an A15 precipitate, the cracks are partly deflected towards the weak A2-A15 interface, but the 'brittle' intermetallic cannot stop the propagation of cracks in the matrix at RT. In comparison to Cr-8Si, Cr-25Mo-8Si showed fewer cracks within the A15 phase. However, for Cr-25Mo-8Si some larger A15 precipitates showed cracks, while smaller A15 precipitates seemed unaffected by the indentation. Meanwhile, in Cr-8Si, almost all of the A15 precipitates showed isolated cracking. This is in line with the observation in [33], of an improved toughness of Cr_3Si when Mo is incorporated.

The Cr-26Mo-3Si alloy (Figure 8 c)) is a single BCC (A2) phase material and is the same composition of the A2 phase of the Cr-25Mo-8Si alloy (Figure 8 b)). This helps to distinguish between the effect of Mo addition to the Cr solid solution and the influence of the intermetallic phase. In Figure 8 c) the single-phase material is depicted. No cracks were produced during Vickers testing, confirming that substituting Cr with Mo in A2 does not lower the fracture toughness to critical values at RT in the Vickers test set-up used here. So while the Mo-enriched BCC matrix showed reasonable toughness in the single-phase material (no cracks), it showed failure (cracking in the matrix) when the intermetallic $(Cr,Mo)_3Si$ phase is present. Also, the difference in grain size and morphology likely has a crucial influence on the deformation behavior of the alloys. Figure 9 shows EBSD images of the crystallographic grain orientation for the annealed two-phase alloy Cr-25Mo-8Si and single-phase material Cr-26Mo-3Si. The grain size and structure differ greatly although the same annealing procedure was used for both alloys. The single-phase material had much larger grains, above 200 µm and some larger than 500 µm, while the two-phase alloy had grain sizes in the 50 – 200 µm

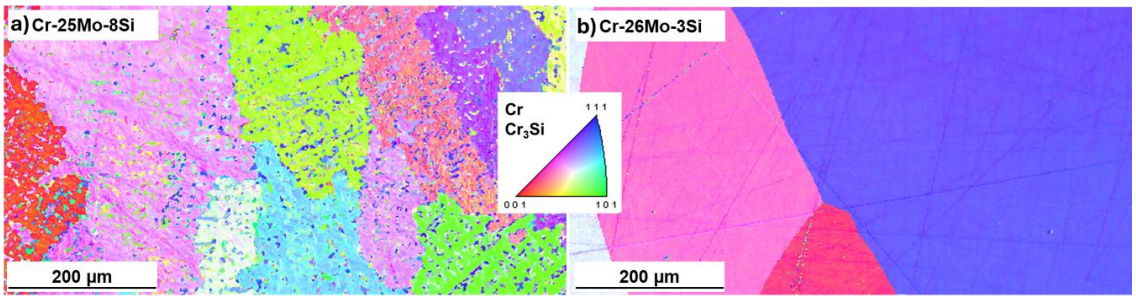

Figure 9: EBSD images of crystallographic grain orientation for identically annealed a) Cr-25Mo-8Si (A2 matrix + A15 precipitates) and b) single-phase (A2) Cr-26Mo-3Si alloy.

range. As explained earlier (section 3.1 Microstructure) the formation of A15 phase precipitates creates grain nucleation sites during annealing. Additionally, it has to be taken into account that for Cr-25Mo-8Si σ phase is present in the as-cast state and decomposes into A2 and A15 phase during annealing [14], which also contributes to grain refinement. So, despite the same composition of the A2 phase for both materials, the grain size and shape vary widely, showing that the formation of the A15 phase affects the grain morphology and the overall fracture toughness.

3.4 Strength and deformation in compression

To investigate the influence of Mo and the corresponding change in microstructure on the compression behavior of Cr-xMo-8Si alloys, Mo contents of x = 0, 10, 20, 25 at.% were tested and compared. Higher Mo contents, as well as single-phase alloys, were not included, since it was previously demonstrated that they have undesirable properties during high-temperature oxidation at T >1100 °C (strong MoO_3 evaporation) [14, 38]. It is worth noting that the materials tested in this work can only give a preliminary impression of the mechanical properties of the newly developed Cr-xMo-8Si alloys produced via arc melting. Alternative manufacturing methods like a powder manufacturing route will produce a more homogeneous microstructure at lower annealing temperatures. This will result in smaller and more reasonable grain sizes and can increase the strength and toughness of the alloys further.

In Figure 10 a)-e) the stress-strain curves of compressively tested Cr-xMo-8Si alloys at various temperatures are depicted. From this data, the strain at maximum stress was extracted to assess the ductile-to-brittle transition temperature (DBTT) range of the tested alloys (see Figure 10 f). From this data it is clear that a transition between rather brittle failure and ductile deformation for Cr-8Si is located between 500 and 700 °C. This is already a massive increase of DBTT compared to pure Cr, which can show a DBTT of -25°C to -45°C for ultra-pure Cr [39, 28], 130-140 °C for rolled Cr [40, 41] and up to 230°C for as-sintered material [41]. Figure 10 f) shows that an increased amount of Mo shifts the DBTT to even higher temperatures, between 700°C and 900°C for 10 at.% Mo and above 900°C for 20-25 at.% Mo. Despite the facts that: a) substituting Cr with Mo in the solid solution leads to decreased Si solubility [14], b) pure Mo has a low

DBTT (-136°C) [15], and c) additions of Mo up to 3wt.% were shown to lower the DBTT of Cr [28], the statement of Ault in 1967 is also confirmed for Mo that “solid solution alloying additions to improve strength generally raise the DBTT” [42].

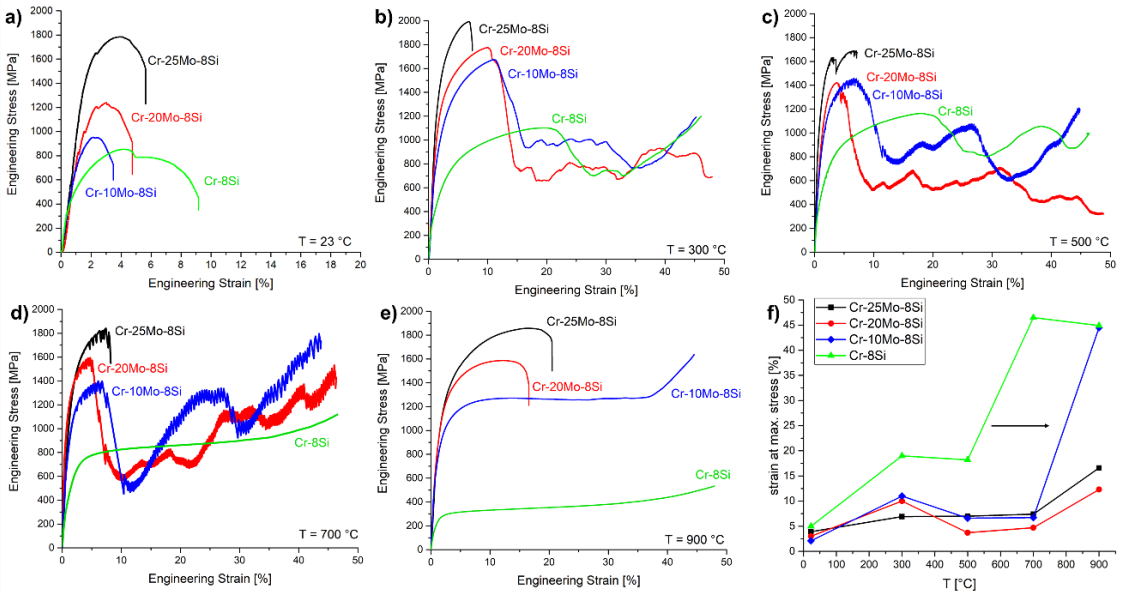

Figure 10: Stress-strain curves for compressive testing (with strain rate 2.5 x 10-4 s-1) of Cr-xMo-8 at%Si alloys at a) 23, b) 300, c) 500, d) 700 and e) 900 °C; f) Strain at max. stress vs. temperature

However, from the stress-strain curves (Figure 10 a-e) a certain compressive ductility before total failure is visible at RT for all of the investigated alloys. In Figure 11 the compression testing setup, the initial cylindrical sample types, and the appearance of all samples after the compression test are depicted. Note that the compression tests were either stopped due to detected failure (sudden loss

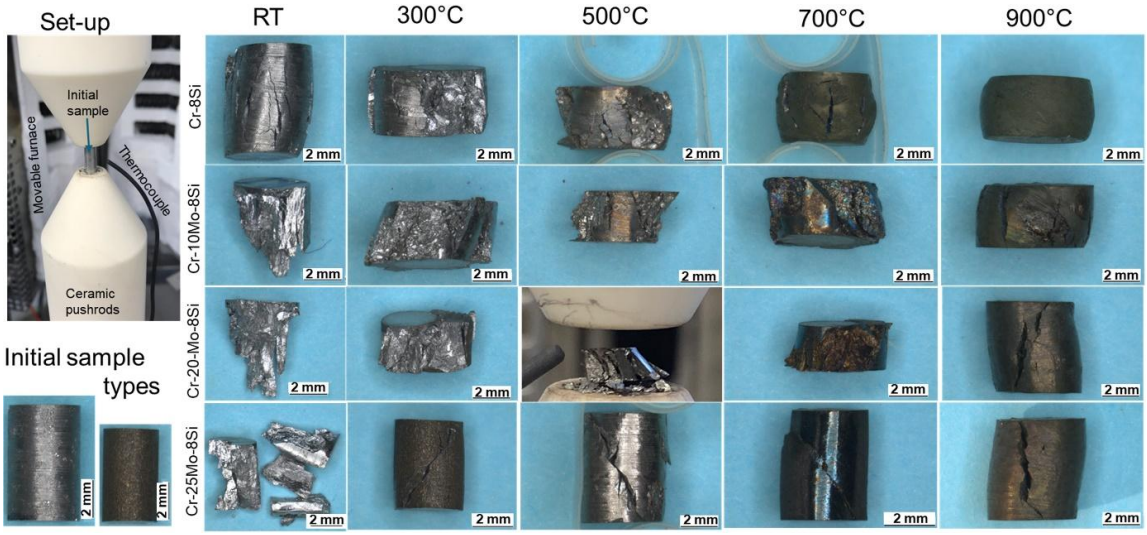

Figure 11: Samples after compression testing either until ≈ 50% compression or after breakage

of >80% load) or the test was aborted at a travel distance of half of the sample length.

While the reference alloy Cr-8Si at RT showed failure by cracking at an engineering strain of ca. 9%, for all other temperatures investigated, the test ran until ≈50% engineering strain. The sample tested at 900 °C shows no visual surface cracks and relatively homogenous ductile deformation behavior. The other samples of 10, 20 and 25 at.% Mo deformed rather non-homogeneously in a mixed state of brittle-ductile behavior. This effect was more potent with increasing Mo content. All Mo-containing samples (10-25 at.%) were tested at room temperature until breakage, whereupon they usually broke into several pieces. At temperatures between 300 and 900 °C for Mo contents of 10-20 at.% the compression tests ran until ≈50% engineering strain but showed strongly non-homogeneous deformation behavior. At a content of 25 at.% Mo and temperatures between 300-900 °C, the cylinders failed with a fracture running along the sample at 45°, the plane of maximum shear stress, at an engineering strain of 5% (RT) and 20% (900°C).

To determine the specific strength of the alloys, the proof stress at 0.2% strain (used as the approximated yield stress) was determined and divided by the material density. For Cr-xMo-8Si with x=0, 10, 20, 25 at.% Mo the determined densities are 6.96, 7.18, 7.43, and 7.62 g/cm^3, respectively. The specific strength of the materials versus their Mo content is plotted in Figure 12 a) for all of the tested temperatures.

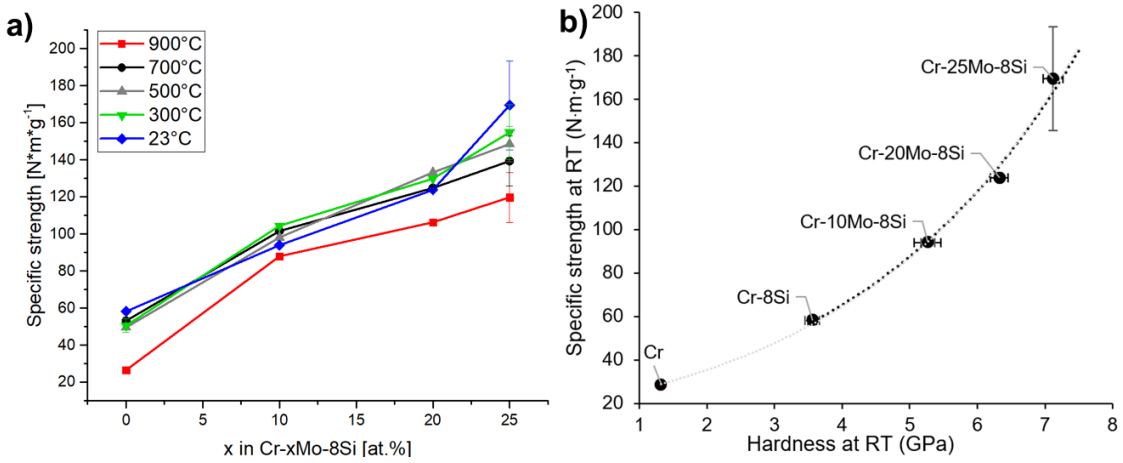

Figure 12: Calculated a) specific strength vs. Mo content and b) vs. RT hardness (literature data for Cr from [43])

The overall trend shows that the specific strength of the Cr-xMo-8Si alloys increases with increasing Mo content for all of the investigated temperatures. Between 23 and 900°C for Cr-8Si, the specific strength values ranged from 27 to 58 $N \cdot m \cdot g^{-1}$, for Cr-10Mo-8Si between 88 and 104 $N \cdot m \cdot g^{-1}$, for Cr-20Mo-8Si from 106 to 133 $N \cdot m \cdot g^{-1}$, and for Cr-25Mo-8Si between 120 and 170 $N \cdot m \cdot g^{-1}$. While the alloys with 0 to 20 at.% Mo content had a rather stable specific strength from RT to 700 °C, the beginning of a decrease in strength could be noted for the compression at 900 °C (red curve of Figure 12 a)). The material with 25 at.% Mo showed decreasing specific strength from RT to 300 °C, a rather constant plateau between 500 and 700 °C, and again the onset of a decrease in strength at 900 °C. Figure 12 b) shows the specific strength of the alloy series plotted against the determined hardness values at RT. For comparison, the value for pure Cr [43] from literature was added. An exponential fit best describes the correlation between the hardness and specific strength within this system.

Figure 13 a) depicts the cross-sections of cylindrical samples (Cr-8Si, Cr-10Mo-8Si) compressed until ≈50% strain at 300 °C (more brittle regime) and 900 °C (more ductile regime) in stereographic overview. Electron microscopic images of the observed crack formation near the centers of the samples are included in Figure 13 b). For the Cr-8Si cylinder compressed at 300 °C, macroscopically, a fracture runs vertically at one side along the cylinder. In contrast, the rest of the

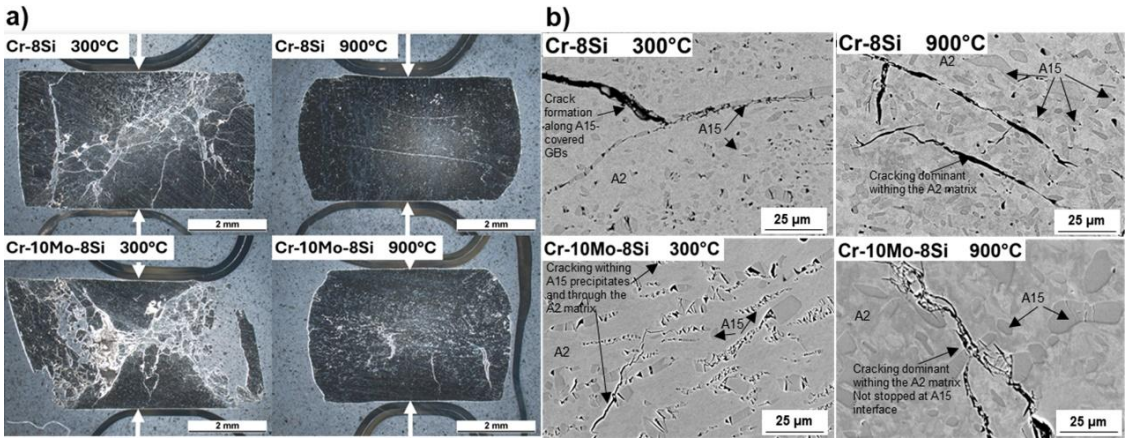

Figure 13: Cross-sections of cylindrical samples (Cr-8Si, Cr-10Mo-8Si) compressed until ca. 50% strain at 300 and 900°C a) in stereographic overview (arrows showing the compression direction) and b) BSE images near the middle of the samples

fractures predominantly run diagonally along the planes of maximum shear stress at 45°. Microscopically (see Figure 13 b)), cracks run along grain boundaries

decorated with the A15 phase. Isolated cracking within the A15 phase precipitates and along the A2-A15 interface was observed, while the solid solution matrix could deform significantly before cracking occurred. At 900 °C for the same Cr-8Si material, the behavior was reversed. Macroscopically visible fractures do not accompany the overall deformation. On a microscopic scale, it is clear that initial cracking occurred in the solid solution. The cracks in the solid solution were often stopped by the A15 intermetallic, but some also propagated through the intermetallic phase. The A15 phase was not greatly affected by compression at 900 °C for Cr-8Si. So, while at 300 °C the A2 phase is the more ductile phase inhibiting crack propagation (cracks which had been initiated in the A15 phase), at 900 °C the intermetallic A15 phase provides additional strength and can limit crack propagation inside the A2 solid solution.

By adding Mo to the alloy (Cr-10Mo-8Si), the resulting macroscopic fracture pattern after compression up to 50% strain is more pronounced at both temperatures (Figure 13 lower row). At 300 °C, the main fractures run diagonally at a 45° angle in both directions of the cylinder, forming an overall X-shaped fracture and leaving an hourglass-shaped region of less deformed material at the top and the bottom of the cylinder. The slanted shape of the cylinder points towards a misalignment during compression, explaining the slightly higher value for yield stress observed for this sample (Figure 12 a)). For 900 °C, three vertical but isolated fractures are visible. Microscopically, cracking occurred mainly within the A15 phase at 300 °C, but some regions with cracks inside the A2 matrix were also observed. For 900 °C, there is much less crack formation within the A15 phase, and the dominant crack formation and propagation was inside the A2 phase. When encountering an A15 phase, the intermetallic also starts to show crack formation and partly manages to deflect the crack. Overall, the crack formation and propagation mechanisms are similar for both compositions (Cr-8Si vs. Cr-10Mo-8Si). Still, the strengthening effect of Mo at high temperatures leads to an overall decreased ductility, in-line with the reduced fracture toughness observed in the Vickers testing.

Figure 14 shows the alloy composition with the highest Mo content (Cr-25Mo-8Si) compressed at 300 and 900 °C up to breakage. Both of these temperatures are still in the brittle regime of the alloy. The high strengthening effect of Mo in this

alloy inhibited strong deformation and thus led to fracture before compression to 50% strain. For 300 °C the cylinder failed at ca. 7.5% strain and at 900 °C a strain level of 20% was reached before failure. In the 300 °C sample, the fracture ran along a 45° degree plane through the cylinder. This is similar to the sample compressed at 900 °C, though here the fracture seemed to be partly deflected, as it is not running along the full length of the diagonal. Microscopic cracks can

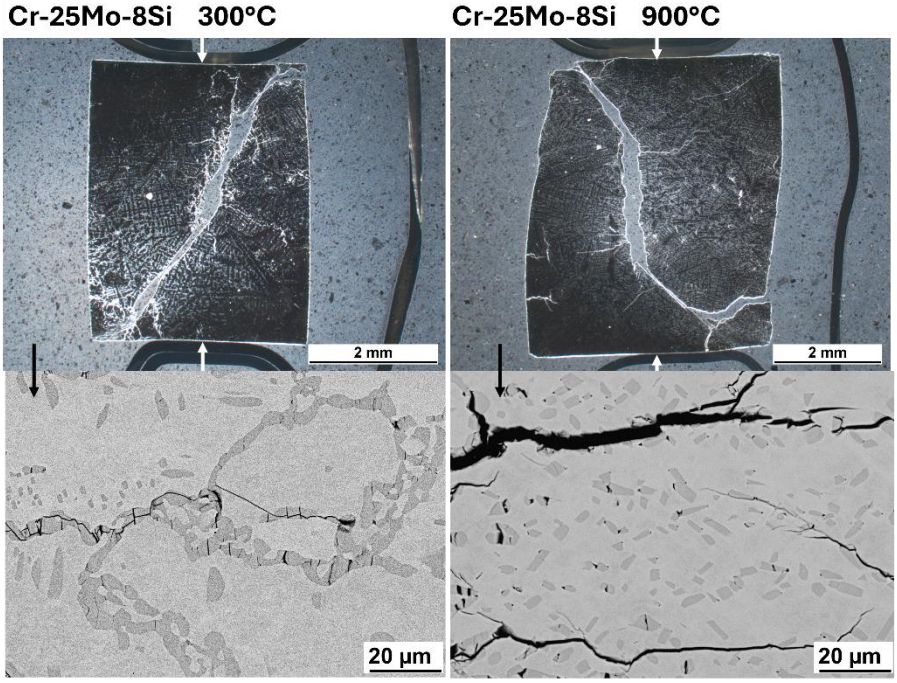

Figure 14: Cross-sections of Cr-25Mo-8Si compressed until breakage (at ca. 7.5% strain at 300 and 20% at 900°C) in stereographic overview (arrows showing the compression direction) (top) and SEM images (bottom)

be observed near the middle of the sample and next to the primary fracture. Again, for low temperatures, the cracks were within the intermetallic phase, while at 900 °C the A2 matrix failed first. The cracks through the A2 phase are partly deflected to the A2-A15 interface when encountering an intermetallic precipitate. To compare the strength of the alloy series, the yield stress determined from 0.2% proof stress is depicted in Figure 15 with the addition of data from the literature. Data for a commercial Ni-based alloy IN718 (compressive [44] and tensile tests [45]), compressive test data of a Mo-based alloy [7], two recently investigated Cr-based alloys [38, 46], Cr-8Si [22], and pure Cr [43] are included with the applied strain rates when available. The Cr-25Mo-8Si (density 7.6 g/cm^3) alloy, showing the highest yield stress at room temperature, is comparable with IN718 (density 8.2 g/cm^3 [47]). Above 700°C, it does not show the sharp drop of IN 718. This

generally suggests that Cr-based alloys can be used for higher service temperatures as compared to Ni-based alloys due to their superior high-temperature mechanical stability.

Comparing the two-phase alloy Cr-25Mo-8Si with a recently investigated single-phase Cr-Mo-Si alloy, Cr-36.1Mo-3Si from Hinrichs et al. [38], shows that despite the higher amount of Mo in the A2 phase the determined strength is lower for the

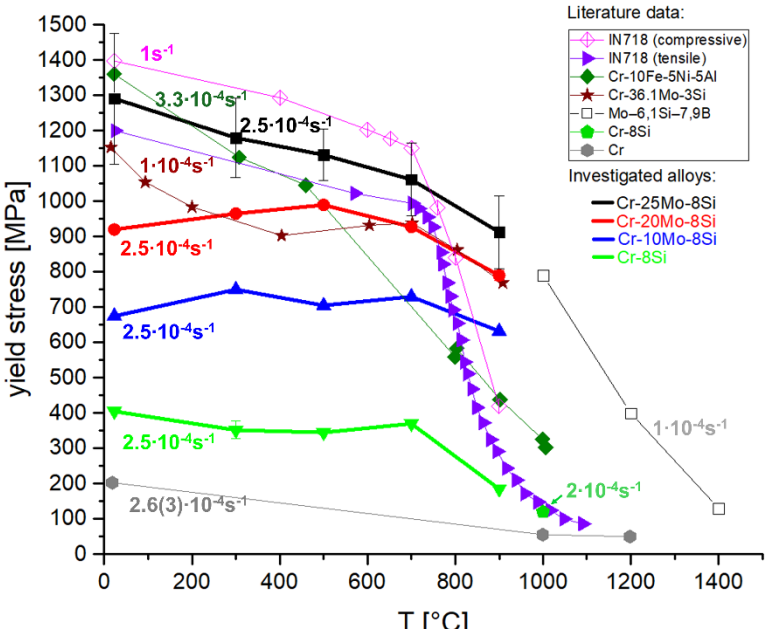

Figure 15: Yield stress (determined from proof stress at 0.2%) of investigated Cr-xMo-8Si alloys vs. temperature determined from compression tests with addition of literature data for comparison (IN718 [44, 45], Cr-10Fe-5Ni-5Al [46], Cr-36.1Mo-3Si [38], Mo–6.1Si–7.9B [7], Cr8Si [22], Cr [43]).

single-phase alloy. Thus, the A15 phase does noticeably improve the overall strength of the alloy. This effect should even be more pronounced in creep testing at very high temperatures. The incorporation of the A15 phase for the Cr-Mo-Si system enables alloy designs with reasonable Mo contents for high-temperature applications (Mo contents above 25 at.% lead to excessive MoO_3 formation during high-temperature oxidation in Cr-xMo-8Si alloys [14] and are thus not desirable). Notably above 700°C, the trend of the temperature-dependent yield stress in the single-phase alloy Cr-36.1Mo-3Si [38] and Cr-25Mo-8Si are very comparable, suggesting that despite lifting the overall strength to higher levels, the A15 phase does not strongly contribute to preserving strength at higher temperatures. An alternative alloy design recently developed by Ma et al. [46], which used Fe as an alloying element in a Cr-based alloy combined with NiAl

particles for precipitation hardening, achieved a similar maximum strength at room temperature for Cr-10Fe-5Ni-5Al [46] as Cr-25Mo-8Si. But above 500 °C the strength of Cr-10Fe-5Ni-5Al [46] drops drastically and thus the alloy is likely not usable at higher service temperatures >1100°C. The comparison with these two alternative Cr-based alloy systems shows that both mechanisms, the implementation of the A15 phase and the strengthening of Cr solid solution by Mo, are relevant for achieving an attractive strength profile at high temperatures.

4. Conclusions and Outlook

Increasing the Mo content in Cr-xMo-8Si alloys linearly increases the RT hardness. The dominant hardening mechanism is the solid solution hardening of the A2 phase, while precipitation hardening via the A15 phase has a minor contribution at RT. Accordingly, the hardness was also not significantly affected by annealing conditions that changed the size and distribution of the A15 phase and released residual stresses. The hardness of the A15 phase decreases with addition of Mo and finer intermetallic precipitates improve the resistance against cracking.

The incorporation of Mo to Cr-xMo-8Si alloys leads to a change in grain size and morphology, with Mo having a grain refining effect in the alloy. The A15 phase also has an additional grain refining effect.

The fracture toughness of the arc-melted Mo-containing two-phase Cr-xMo-8Si alloys of this study is not high enough for structural applications (<15 $MPa \cdot m^{0.5}$). However, the Cr-8Si (A2+A15 phase) reference sample and the Mo-reinforced single-phase material Cr-25Mo-3Si do not show crack formation during the tests, so both can be assumed to have K_I >10 $MPa \cdot m^{0.5}$. Increasing the Mo content in Cr-xMo-8Si alloys leads to a reduction of the fracture toughness to ≈4 $MPa \cdot m^{0.5}$ which then increases up to 10 $MPa \cdot m^{0.5}$ for higher Mo contents, suggesting that the influence of Mo on the grain size and morphology also plays a crucial role on the fracture behavior.

Compression tests reveal that the DBTT regime is shifted to higher temperatures with increasing Mo content in the Cr-xMo-8Si system. The overall strength of the Cr-xMo-8Si alloys increases with increasing Mo content. A certain compressive ductility before total failure, even at RT, is visible for all of the investigated alloys, but the failure mechanism for Mo-containing alloys is clearly brittle at RT. The Cr-

25Mo-8Si (density 7.6 g/cm^3) composition shows the highest yield stress and is comparable with IN718 (density 8.2 g/cm^3 [47]), but shows a more stable high temperature strength at 900 °C. Comparing the strength vs. temperature profile of two-phase alloy Cr-25Mo-8Si with the recently investigated single-phase alloy Cr-36.1Mo-3Si, from Hinrichs et al. [38], implies that the A15 phase does improve the high-temperature strength value noticeably. Additionally, at 300 °C the A2 phase is the more ductile phase, inhibiting crack propagation, while at 900 °C the intermetallic phase provides additional strength and can limit crack propagation inside the solid solution.

The investigated alloy system is an interesting candidate for the next generation of high-temperature materials. Future studies should explore alternative processing routes to manufacture samples with much smaller grain sizes. This will likely affect the fracture toughness positively and may help to lift these alloys beyond the 15 MPa·m$^{0.5}$ threshold. The results show a finer A15 distribution is beneficial not only from a mechanical point of view but also regarding the high temperature oxidation behavior of Cr-Mo-Si alloys [14].

Acknowledgements

The authors gratefully acknowledge the German Federal Ministry for Economic Affairs and Climate Action (BMWK) for the financial support of the project under grant no. 20E2125 based on a decision of the German Bundestag. The authors thank Alexander Kauffmann from Karlsruhe Institute of technology (KIT) for arc melting the larger alloy buttons in the AM 200 system. For the possibility to perform high load Vickers tests (at Staatliche Materialprüfungsanstalt) the authors thank Jurica Filipovic, Fabrizio Windhaus, Robert Kopp and Gerwin van den Dungen from the technical university of Darmstadt. Also the authors are thankful for the support of Melanie Thalheimer from DECHEMA Research Institute (DFI) for EBSD measurements, Pelle Wolf for assisting in nanohardness testing and the members of the DFI workshop Heinrich Kopietz, Yvonne Hohmann, and Jano Bender for electrical discharge machining of the samples.

Declaration of competing Interest

The authors declare that they have no known competing financial interests or personal relationships that could have appeared to influence the work reported in this paper.

Funding

This project is granted and financed under grant no. 20E2125 by German Federal Ministry for Economic Affairs and Climate Action (BMWK) based on a decision of the German Bundestag.

References

[1] O. Senkov, M. D. B. and K. J. Chaput, "Development and exploration of refractory high entropy alloys—A review," Journal of Materials Research, vol. 33, no. 19, pp. 3092-3128, 2018.

[2] J. Tian, W. Zhou, Q. Tan, M. Wu, S. Qiao, G. D. A. Zhu, D. Shu and S. B., "A review of refractory high-entropy alloys," Transactions of Nonferrous Metals Society of China, vol. 32, pp. 3487-3515, 2022.

[3] P. Tsakiropoulos, "Alloys for application at ultra-high temperatures: Nb-silicide in situ composites Challenges, breakthroughs and opportunities," Progress in Materials Science, vol. 123, p. 100714, 2022.

[4] P. Tsakiropoulos, "Beyond Nickel-Based Superalloys," Encyclopedia of Aerospace Engineering, 2010.

[5] J. Wadsworth, T. G. Nieh and J. J. Stephens, "Recent advances in aerospace refractory metal alloys," International Materials Reviews, vol. 33, no. 3, p. 131, 1988.

[6] K. Yakang, C. Wang, X. Chen, Y. Qu, J. Yu, H. Ju and Y. X., "Review of Research Progress on Mo–Si–B Alloys," Materials, vol. 16, no. 15, p. 5495, 2023.

[7] A. P. Alur, N. Chollacoop and K. S. Kumar, "High-temperature compression behavior of Mo–Si–B alloys," Acta Materialia, vol. 52, pp. 5571-5587, 2004.

[8] R. Su, L. L. and J. H. Perepezko, "Alloy Designs for High Temperature Mo-Base Systems," International Journal of Refractory Metals and Hard Materials, vol. 113, p. 106199, 2023.

[9] H. Harada, "High Temperature Materials for Gas Turbines: The Present and Future," in Congress, Proceedings of the International Gas Turbine IGTC2003Tokyo KS-2, Tokyo, 2003.

[10] L. Liu, L. F. Wood, P. Nelaturu, T. Duan, C. Zhang, F. Zhang, D. J. Thoma und J. H. Perepezko, „Oxidation of a Mo Si B Ti Alloy,“ High Temperature Corrosion of Materials, 2024.

[11] J. Yang, G. Zhuo, K. Jiang, X. Zhu and L. Su, "The Oxidation Resistance of Nb-Si-Based Alloys at Intermediate and High Temperatures," Materials, vol. 13, 2020.

[12] A. S. Ulrich, P. Pfizenmaier, A. Solimani, U. Glatzel and M. C. Galetz, "Improving the oxidation resistance of Cr-Si-based alloys by ternary alloying," Corrosion Science, vol. 165, p. 108376, 2020.

[13] F. Hinrichs, A. Kauffmann, A. S. Tirunilai, D. Schliephake, B. Beichert, G. Winkens, K. Beck, A. S. Ulrich, M. C. Galetz, Z. Long, H. Thota, Y. Eggeler, A. Pundt and M. Heilmaier, "A novel nitridation- and pesting-resistant Cr-Si-Mo alloy," Corrosion Science, vol. 207, p. 110566, 2022.

[14] L. Koliotassis, E. M. H. White and M. C. Galetz, "The Influence of Mo Content and Annealing on the Oxidation Behavior of Arc-Melted Cr–xMo–8Si Alloys," Advanced Engineering Materials, p. 2301906, March 2024.

[15] E. M. Savitskii and G. S. Burkhanov, Physical Metallurgy of Refractory Metals and Alloys, New York: Consultants Bureau, 1970, p. 53.

[16] DERA, "Raw Material Price Monitor," Federal Institute for Geosciences and Natural Resources, 2023.

[17] A. Solimani-Dorcheh and M. C. Galetz, "Challenges in Developing Oxidation-Resistant Chromium-Based Alloys for Applications Above 900°C," The Journal of Minerals, Metals & Materials Society, vol. 68, p. 2793–2802, 2016.

[18] W. Hagel, "Factors Controlling the High-Temperature Oxidation of Chromium," Transactions of American Society for Metals, vol. 56, pp. 583-599, 1963.

[19] W. D. Klopp, "Recent Developments in Chromium and Chromium Alloys," Journal of Metals, vol. 21, pp. 24-32, 1969.

[20] Y. F. Gu, H. Harada and Y. Ro, "Chromium and Chromium-Based Alloys: Problems and Possibilities for High-Temperature Service," The Journal of The Minerals, Metals & Materials Society, vol. 56, pp. 28-33, 2004.

[21] A. Solimani-Dorcheh and M. C. Galetz, "Oxidation and Nitridation Behavior of Cr–Si Alloys in Air at 1473 K," Oxidations of Metals, vol. 84, pp. 73-90, 2015.

[22] Y. Aono, T. Omori and R. Kainuma, "Microstructure and high-temperature strength in Cr–Si binary alloys," Intermetallics, vol. 112, p. 106526, 2019.

[23] S. V. Raj, "An evaluation of the properties of Cr,Si alloyed with Mo," Materials Science and Engineering A, vol. 201, pp. 229-241, 1995.

[24] J. W. Newkirk and J. A. Sago, "Ductile-Phase Toughening if Cr_3Si with Chromium," Intermetallic Matrix Composites, vol. 194, pp. 183-189, 1990.

[25] T. A. Cruse and J. W. Newkirk, "Tailoring Alloys Using Hot Pressing and Mechanical Alloying," in Proceedings of the 1st International Non-Ferrous Processing and Technology Conference, St.Louis, Missouri, 1997.

[26] P. Pfizenmaier, A. S. Ulrich, U. Glatzel and M. C. Galetz, "Tensile Creep Properties of Cr-Si Alloys at 980 °C in Air - Influence of Ge and Mo Addition," Metals, vol. 11, no. 7, pp. 1072-1080, 2021.

[27] A. S. Ulrich, P. Pfizenmaier, A. Solemani, U. Glatzel and M. C. Galetz, "Strengthened Cr-Si-base alloys for high temperature applications," International Journal of Refractory Metals & Hard Materials, vol. 76, pp. 72-81, 2018.

[28] O. N. Carlson, L. L. Sherwood and F. A. Schmidt, "The effect of low percentage alloying additions on the ductility of iodide chromium," Journal of the less-common metals, vol. 6, pp. 439-450, 1964.

[29] H. Blumenauer and G. Pusch, Technical fracture mechanics, Leipzig: Deutscher Verlag Für Grundstoffindustrie, 1993, p. 101.

[30] DIN German Institute for Standardization, DIN 50106 Testing of metallic materials – Compression test at room temperature (ICS 77.040.10), Berlin: Beuth Verlag GmbH, 2016.

[31] W. Trzebiatowski, H. Ploszek and J. Lobzowski, "X-ray Analysis of Chromium-Molybdenum and Chromium-Tungsten Alloys," Analytical Chemistry, vol. 19, no. 2, pp. 93-95, 1947.

[32] F. Sun, "Integrated TEM/transmission-EBSD for recrystallization analysis in nickel-based disc superalloy," Progress in Natural Science: Materials International, vol. 31, pp. 63-67, 2021.

[33] T. Cruse and J. W. Newkirk, "Evaluation of methods to produce tough Cr_3Si based composites," Materials Science and Engineering, vol. A239, no. 240, p. 410–418, 1997.

[34] J. A. Lemberg and R. O. Ritchie, "Mo-Si-B Alloys for Ultrahigh-Temperature Structural Applications," Advanced Materials, vol. 24, pp. 3445-3480, 2012.

[35] K. Ioroi, Y. Aono, X. Xu, T. Omori and R. Kainuma, "Melting point of pure Cr and phase Equilibria in the Cr-Si binary system," Journal of Phase Equilibria and Diffusion, vol. 43, pp. 229-242, 2022.

[36] A. B. Gokhale and G. J. Abbaschlan, "The Mo-Si (Molybdenum-Silicon) System," Journal of Phase Equilibria, vol. 12, no. 4, pp. 493-498, 1991.

[37] L. Qian, M. Li, Z. Zhou, H. Yang and X. Shi, "Comparison of nano-indentation hardness to microhardness," Surface & Coatings Technology, vol. 195, pp. 264-271, 2005.

[38] F. Hinrichs, G. Winkens, Kramer, L. K., D. Schliephake, G. Falcão, M. C. Galetz, I. H., A. Kauffmann and M. Heilmaier, "Overcoming barriers for high temperature alloys: oxidation and," 2024.

[39] D. J. Maykuth, W. Klopp, R. I. Jaffee and H. B. Goodwin, "A Metallurgical Evaluation of Iodide Chromium," Journal of The Electrochemical Society, vol. 102, no. 6, pp. 316-331, 1955.

[40] B. A. Wilcox, N. D. Veigel and A. H. Clauer, "Ductile-Brittle Transition of Thoriated Chromium," METALLURGICAL TRANSACTIONS, vol. 3, pp. 273-283, 1972.

[41] Y. Harada and M. Ohmori, "Ductile–brittle transition behavior of rolled chromium," Journal of Materials Processing Technology, Vols. 153-154, p. 93–99, 2004.

[42] G. M. Ault, "Alloying principles and strengthening mechanisms," Work of the US Gov. Public Use Permitted, Sandefjord, Norway, 1967.

[43] Y. Ro, Y. Koizumi, S. Nakazawa and T. Kobayashi, "Development of Cr-base alloys and their compressive properties," Scripta Materialia, vol. 46, pp. 331-335, 2002.

[44] A. Iturbe, E. Giraud, E. Hormaetxe, A. Garay, G. Germain, K. Ostolaza and P. J. Arrazola, "Mechanical characterization and modelling of Inconel 718 material behavior for machining process assessment," Materials Science & Engineering A, vol. A 682, pp. 441-453, 2017.

[45] J. R. Davis, Nickel, Cobalt, and Their Alloys, ASM international, 2000.

[46] K. Ma, T. Blackburn, J. P. Magnussen, M. Kerbstadt, P. A. Ferreirós, T. Pinomaa, C. Hofer, D. G. Hopkinson, S. J. Day, P. A. J. Bagot, M. P. Moody, M. Galetz und A. J. Knowles, „Chromium-based bcc-superalloys strengthened by iron supplements,“ Acta Materialia, Bd. 257, p. 119183, 2023.

[47] ErproGroup, „https://erpro-group.com,“ 04 2019. [Online]. Available: https://erpro-group.com/wp-content/uploads/2019/04/Ni_IN718.pdf. [Zugriff am 22 10 2024].

[48] E. M. Savitskii and G. S. Burkhanov, Physical Metallurgy of Refractory Metals and Alloys, New York: Consultants Bureau, 1970, pp. 16-22; 193-199.

[49] Y. Ro, Y. Koizumi, S. Nakazawa, T. Kobayashi, E. Bannai and H. Harada, "Development of Cr-base alloys and their compressive properties," Scripta Materialia, vol. 46, pp. 331-335, 2002.

[50] T. M. Pollock and S. Tin, "Nickel-Based Superalloys for Advanced Turbine Engines: Chemistry, Microstructure, and Properties," Journal of Propulsion and Power, vol. 22, no. 2, pp. 361-374, 2006.

[51] J. A. Sago, "Study of Ductile Second Phase Toughening of Chromium-Silicon Alloys for High Temperature Aerospace Application," Missouri-Rolla, 1996.

3.5 Advanced Cr-Based BCC Superalloys - A2-B2 Strengthening in the Cr-Mo-Si-(NiAl) System

Published in JOM, The Minerals, Metals & Materials Society, Ultra-High Temperature Refractory Metals and Alloys for Complex Environments, 77, (2025), 9608–9622.
DOI: 10.1007/s11837-025-07915-w

Authors

Lisa Zander[1], Julian Peter Zander[1], Thomas Blackburn[2], Emma M. H. White[1], Alexander J. Knowles[2], Mathias C. Galetz[1]

[1] DECHEMA Research Institute, Theodor-Heuss-Allee 25, 60486 Frankfurt a.M., GER.

[2] School of Metallurgy and Materials, University of Birmingham, UK.

Abstract

The Cr-Mo-Si-Ni-Al alloy system was investigated with the goal of combining recent advances in the two-phase Cr-Mo-Si system [(Cr,Mo)-A2 matrix + $(Cr,Mo)_3Si$-A15 precipitates], with the approach of strengthening the Cr matrix with the low misfit precipitate NiAl (B2). The role of Mo and Si in the system was investigated in alloys that were arc-melted, annealed and characterized for microstructure, hardness, fracture toughness and compressive strength at various temperatures (21 – 1000°C). Unlike the A15 phase, the B2 phase does not reduce the fracture toughness of the Cr solid solution matrix. The yield stress of the A2-B2 system is comparable to that of the A2-A15 system, but retains its strength up to higher temperatures (tested up to 1000°C). The addition of Ni and Al to the Cr-Mo-Si system shifts the stability regime of the σ phase in the system to lower Mo and Si contents and lower temperatures. Since Ni shows high solubility in the σ phase, reducing the Ni/Al ratio reduces the amount of the σ phase. The implementation of NiAl precipitates to the Mo- and Si-strengthened Cr matrix has a beneficial effect on the high temperature strength and low-temperature fracture toughness of the Cr-based alloys.

Introduction

Among the refractory metals, chromium (Cr) is a favorable base material for a new class of high temperature alloys to compete against the state-of-the-art nickel (Ni)-based superalloys. Due to beneficial features such as a lower density, lower cost, and higher melting temperature than Ni (1907°C vs. 1455°C) [1, 2], Cr has recently gained significantly more attention [3, 4, 5, 6, 7, 8, 9, 10, 11, 12] [13, 14]. However, the application of Cr-based alloys as high temperature structural materials remains limited due, in part, to three major challenges that must be addressed: (1) the ductile-to-brittle-transition temperature has to be reduced to guarantee an adequate fracture toughness and processability at low temperatures [15, 16, 17, 18]; (2) the high-temperature creep strength must be improved; and (3) oxidation/nitridation resistance above 1000°C has to be enhanced to ensure suitable performance at high service temperatures [4, 6, 19, 20, 21].

Alloying measures have already addressed some of these challenges. Especially, the incorporation of silicon (Si) and molybdenum (Mo) has been found to enhance the properties of Cr-based alloys [5, 7, 8, 10, 11, 12, 3]. Mo acts as a solid-solution strengthener and helps to prevent the nitridation of the Cr-A2 matrix [8, 11, 12]. Si contributes by forming an intermetallic strengthening compound (Cr_3Si with an A15 structure), while promoting the development of a protective SiO_2 scale during high-temperature oxidation [3, 5, 11].

Recent developments in Cr-Mo-Si two-phase alloys (A2+A15) resulted in excellent oxidation resistance at 1200°C [11] and mechanical strength (compression) comparable to the Ni-based superalloy, IN718 [12]. However, their low-temperature fracture toughness remains limited, likely due to the brittle and coarse A15 precipitates [12]. While Cr-based single-phase A2 alloys strengthened by Mo offer reasonable low-temperature toughness, they lack sufficient creep resistance at high temperatures [12]. To address this, Ni and aluminum (Al) have been proposed as an addition to the Cr-Mo-Si system to replace the A15 phase with low lattice misfit [9] NiAl-B2 precipitates. The general idea behind the A2-B2 microstructure is to transfer the known strengthening y-y' microstructure used in Ni-based superalloys to the β-β' microstructure of BCC refractory based alloys [22, 23]. Recent thermodynamic calculations by Kube et

al. [24] predicted the Cr-Mo matrix phase as a good candidate for forming an A2-B2 microstructure when incorporated with the B2-NiAl strengthening phase. Therefore, the Cr-Mo-Si system can be seen as an ideal system to incorporate the B2-NiAl strengthening phase. The goal of this study is to adopt an A2-B2 architecture (as presented in the Cr(Fe)-Ni-Al system [9, 25, 26]) while maintaining the benefits of Mo and Si additions. This study builds on previous investigations of two-phase Cr-xMo-8 at.%Si alloys (A2+A15), in which Cr-20Mo-8 at.%Si and Cr-25Mo-8 at.%Si demonstrated good oxidation resistance at 1200°C in air [11]. Specifically, Cr-25Mo-8 at.%Si performs exceptionally well since it forms a protective duplex oxide scale (Cr2O3-SiO2). However, it forms a σ phase in the as-cast condition which is preferably avoided due to the brittleness and instability. The ternary tetragonal σ phase with a broad compositional range of $Cr_{0.39\text{-}0.57}Mo_{0.29\text{-}0.47}Si_{14}$ was first described in 1974 by Rudy et al. [27], and has subsequently been observed and further studied in other works [5, 11], but the full stability range is still under investigation [28]. In the Cr-Mo-Si system, the σ phase shows a eutectoid decomposition to A2 and A15 after annealing at 1200°C [5, 11, 27]. On the other hand, Cr-20Mo-8 at.%Si does not form a continuous duplex oxide scale but still offers good oxidation resistance and does not form a σ phase in the as-cast state [11]. Both alloys (Cr-20Mo-8 at.% and Cr-25Mo-8 at.%) show high yield stress (0.2%) at high temperatures (tested up to 900°C [12]) but a low fracture toughness at room temperature related to the A15 precipitates [12]. This makes it a perfect system to transform into a BCC superalloy by incorporating B2 strengthening precipitates.

Experimental methods and analytics

Synthesis of the alloys

The investigated Cr-Mo-Si-(Ni-Al) alloys were produced via arc-melting under an argon atmosphere. Pure raw elements, Cr (> 99.95%), Si (> 99.999%), Mo (> 99.97%), Ni (> 99.98%) and Al (> 99.999%) were used to produce ~ 7 g ingots for the microstructural and hardness studies. Selected compositions were further arc melted (~ 250 g) to machine cylinders for compression testing. The ingots were fabricated on a water-cooled copper plate using a non-consumable tungsten electrode. The chamber was purged with argon (Ar) five times, and

zirconium or titanium were pre-melted to minimize residual oxygen. The ingots were remelted and flipped at least five times with additional electromagnetic stirring applied during the production of 250 g ingots to ensure homogeneity.

Annealing

All the arc-melted samples were annealed in a tube furnace under an Ar/5 vol%H_2 gas mixture. The annealing process involved two steps: first, a homogenization step at 1400°C, with a heating rate of 5°C/min and a dwell time of 10 h, which was followed by an aging step at a lower temperature of 1200°C for an additional 100 h. All the samples were furnace-cooled. The furnace temperature was observed to drop below 800°C within 30 min, below which the diffusion kinetics are assumed to have a negligible impact on the coarsening of the precipitates, as suggested from the observations presented in ref. [9].

Microstructural analysis

The arc-melted and annealed samples were mounted, ground to P4000-grade SiC paper, and polished to 1 µm diamond for microstructural analysis and hardness testing. Final polishing to achieve the surface finish required for EBSD included a colloidal silica suspension. Optical and scanning electron microscopy (SEM; FlexSEM 1000II; Hitachi) was used for backscattered electron (BSE) imaging to generate elemental contrast. Phase identification was assisted via X-ray diffraction (XRD; D8 Advance; Bruker), using a Cu cathode (λ = 1.54 Å) and comparing the diffraction pattern to known phases within the ICDD/PDF-4 structure database. Synchrotron XRD (SXRD) was performed on selected alloy systems at beamline I11 at the Diamond Light Source using a wide-angle position sensitive detector with a 2θ step size of 4 millidegrees, λ = 0.824765 Å (calibrated using a NIST Si 640c standard), zero error = -0.00127, and a collection time of 180 s. Powders were prepared through mechanical grinding using an alumina pestle and mortar before being loaded into 0.5 mm Ø quartz capillaries. Prior to pattern collection, the powder was annealed in-situ (2 min at 500°C) to remove stress induced through the grinding procedure and to allow for sharper reflections to be observed. Patterns were analysed via Rietveld refinement within TOPAS-v5 to determine lattice parameters of the constituent phases. Additional diffraction

patterns were collected prior to annealing to eliminate peaks that may be induced through the annealing procedure.

Elemental compositions were measured using electron probe microanalysis (EPMA; JXA-8100; JEOL) using quantitative wavelength dispersive X-ray spectroscopy (EPMA/WDS) as described in ref. [11]. Electron backscatter diffraction (EBSD; SU5000; Hitachi) analysis was carried out with the “Velocity” EBSD system from EDAX with a sample tilt angle of 70°. Crystal orientation was determined with “OIM v8” software from EDAX applying a standard cleanup (Grain CI Standardization, tolerance 5.0, min size 3, Multi Row 1). For phase assignment, the lattice parameters of $(Cr,Mo)_{ss}$ (A2), $(Cr,Mo)_3Si$ (A15) and σ phase were taken from [11, 27, 28].

RT Hardness testing

Room-temperature Vickers hardness (HV1) was measured using a LEICA VMHT MOT hardness tester by applying a 1 kg load for 15 s at an indentation speed of 50 µm/s. The determined values represent the average of at least ten measurements. The conversion of HV1 (Vickers hardness with a 1 kgf test load) to GPa was done by multiplying the HV1 value by 0.009807. To evaluate fracture behavior, additional Vickers tests were conducted at a higher load (HV30) using a KB250 tester (KB Prüftechnik).

Compression testing

Cylindrical samples (d = 3 mm, l_o = 4.5 mm) were produced by electric discharge machining for compression tests at 21, 300, 500, 700, 900 and 1000°C. All the faces were ground to a P500-grade SiC finish. Dimensions were measured with a digital caliper for each sample before compression. For each temperature, three samples were tested to ensure reproducibility. Tests were conducted using an “Inspekt 50” rig with alumina pushrods and a vertical furnace with a thermocouple placed near the sample surface that monitored the temperature during the test. A preload of 10 N was applied and kept constant during heating to account for expansion. After reaching the target temperature, a strain rate of 2.5×10^{-4} s^{-1} was applied until fracture (> 80% load drop) or a travel distance of 50 % of l_o. Force-length variation for the testing set-up was corrected using calibration data

for each temperature. Obtained force displacement data was converted to engineering stress (σ, MPa) and strain (ε) using:

$$\sigma = \frac{F}{A} \tag{1}$$

where F is the measured force (N) and A is the initial cross-sectional area (mm^2).

$$\varepsilon = \frac{\Delta l}{l} \tag{2}$$

where Δl is the change in length (mm) and l is the original length (mm).

Results and Discussion

Microstructural characterization

Microstructural observations and characterization of the as-cast condition

First, the effect of additions of Ni and Al to the initial system of arc-melted Cr-xMo-8Si (x = 20, 25 at.% Mo) was investigated. The Cr/Mo ratio and the Si content were kept constant, with 5 at.% of Ni and 5 at.% of Al added to the alloy to form the NiAl-B2 precipitates, analogous to the amount used in ref. [9]. This

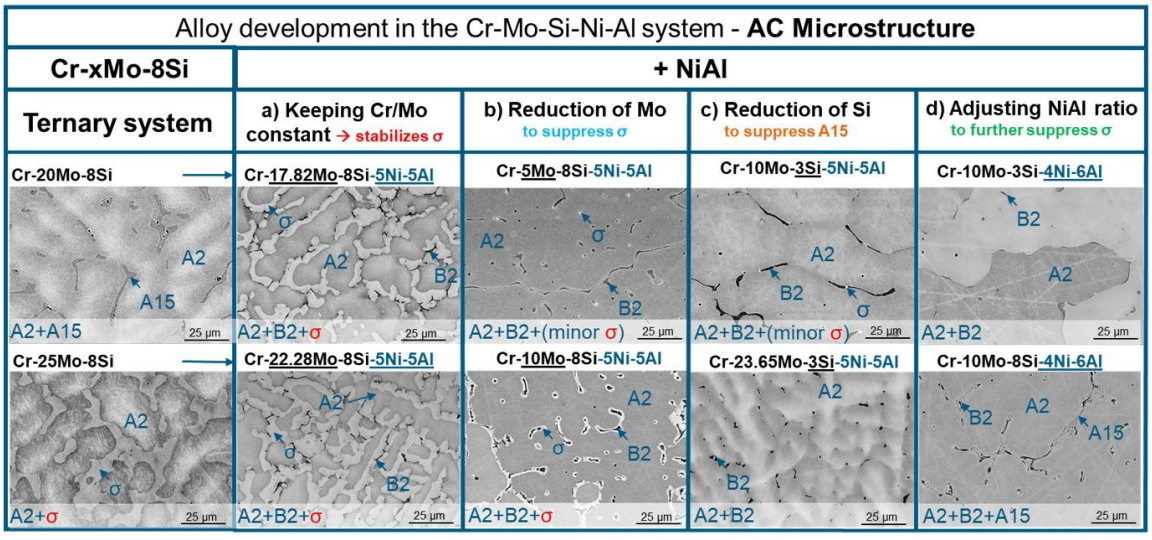

Fig. 1. SEM-BSE overview of as-cast (AC) microstructures in the Cr-Mo-Si+Ni-Al alloy system, ordered in terms of changes compared to the ternary system: (a) keeping Cr/Mo constant (b) reduction of Mo (c) reduction of Si (d) adjustment of Ni/Al ratio.

resulted in nominal compositions of Cr-17.82Mo-8Si-5Ni-5 at.%Al and Cr-22.28-Mo-8Si-5Ni-5 at.%Al (Fig. 1 (a). Second, (Fig. 1 (b)) the Mo content for the Ni and Al containing samples was reduced to 5 and 10 at.% resulting in Cr-5Mo-8Si-5Ni-5 at.%Al and Cr-10Mo-8Si-5Ni-5 at.%Al. Third, the reduction of Si content was investigated by using the compositions Cr-10Mo-3Si-5Ni-5 at.%Al and Cr-23.65Mo-3Si-5Ni-5 at.%Al (Fig. 1 (c). Finally, the Ni/Al ratio was adjusted and resulted in the as-cast microstructure presented in Fig. 1 (d) with a nominal composition of Cr-10Mo-3Si-4Ni-6 at.%Al and Cr-10Mo-8Si-4Ni-6 at.%Al. In addition to the microstructural observations (Fig. 1), XRD was performed to aid phase identification. The resulting diffractograms for the studied alloys are presented in the appendix in Fig. 11.

Comparing Cr-20Mo-8Si and Cr-17.82Mo-8Si-5Ni-5Al, both of which have a Cr/Mo ratio of 3.6 and the same Si content (Fig. 1), shows that the sample containing Ni and Al forms A2, B2, and σ phase, whereas the alloy without Ni and Al shows only A2 + A15 formation in the as-cast state. This shows a shift in the stability range of the σ phase field resulting from the addition of Ni and Al. Cr-22.28Mo-8Si-5Ni-5Al (Cr/Mo =2.68) also contains σ phase, as was also already shown for the respective ternary system Cr-25Mo-8Si in the as-cast condition [11]. In the Mo-rich alloys with 5 at.% Ni and Al, the B2 phase is also present in the as-cast state and preferentially formed along phase boundaries of the σ phase. No precipitates within the Cr-A2 matrix phase were observed in the as-cast state for the Mo-rich alloys with 5 at.% Ni and Al.

To reduce the amount of σ phase, while maintaining 5 at.% Ni and 5 at.% Al, the Mo content was reduced to 5 and 10 at.%. A minimum amount of 10 at.% of Mo was tested in the Cr-xMo-8 at.%Si ternary system [11] and was sufficient to fully inhibit nitridation of A2 in oxidation experiments up to 100 h at 1200°C. In Fig. 1 (b) it is clearly visible that a reduction in Mo leads to a reduction in σ phase, a correlation that was also observed for the initial ternary system [11]. The residual σ phase now forms around the NiAl phase, which is unevenly distributed in the Cr-A2 matrix.

To reduce the amount of Si-rich σ phase and to suppress the formation of A15 after annealing, the Si content was additionally reduced (Fig. 1 (c)), which proved successful, as can be observed when comparing Cr-10Mo-8Si-5Ni-5Al (Fig. 1 (b))

and Cr-10Mo-3Si-5Ni-5Al (Fig. 1 (c)). For high Mo contents, dendritic segregation occurs in the as-cast state, as is visible for Cr-23.65Mo-3Si-5Ni-5Al (Fig. 1 c), similar to what was observed in ref. [11].

In a final optimization step, the Ni/Al ratio was reduced from 1 to 0.67. From EPMA/WDS mappings (appendix Fig. 12) and spot measurements, Ni is not only present in the NiAl-B2 phase but also enriched in the σ phase. Thus, Ni is thought to shift and stabilize the σ phase field. Since NiAl has a wide stoichiometric stability range, the Ni/Al ratio was reduced to test the hypothesis that Ni is the σ-phase promoter. Fig. 1 d) confirms that after the Ni/Al ratio adjustment, the amount of σ phase is reduced. This is especially visible when comparing Cr-10Mo-8Si-5Ni-5Al (Fig. 1 (b)) and Cr-10Mo-8Si-4Ni-6Al (Fig. 1 (d)).

Microstructural observations and characterization of the annealed condition

Annealing strategies for both systems Cr-Mo-Si and Cr-Ni-Al, have been reported in the literature [9, 11] and used as a basis to perform a two-step heat treatment in an Ar/5 vol%H2 mixture: first, a homogenization step at 1400°C for 10 h, and second, an aging step at 1200°C for 100 h. The first step at 1400°C targets the solubility of Ni and Al in A2, to dissolve the intergranular NiAl from the as-cast state in the matrix to achieve a fully homogeneous microstructure and to homogenize any concentration gradients. This provides the basis for a controlled and even distribution of NiAl precipitates within the alloys following aging. Aging in the second stage at 1200°C, allows the nucleation and growth of NiAl-B2 due to the reduced solubility of Ni and Al within the A2 matrix at 1200°C. Additionally, for the Cr-Mo-Si system the second step of the annealing usually leads to eutectoid decomposition of the σ phase into the A2 and Cr_3Si-A15 phase [27]. Fig. 2 depicts the microstructure overview after the two-step annealing and confirms the σ phase decomposition for the Cr-25Mo-8Si ternary system (see also XRD patterns in appendix Fig. 13). In the Mo-rich alloys with Ni and Al (Fig. 2 (a), it is visible that the former intergranular NiAl from the as-cast state is now distributed as spherical[1] precipitates in the matrix phase as targeted. No full decomposition of σ-phase is observed after 1200°C annealing for Mo contents ≥

[1] The term *cuboida*l used in the original publication should read *spherical*. This correction does not affect the results or conclusion.

17.8 at.%, although small fractions of A15 remain visible near the σ phase. Thus, the σ phase stability is shifted to lower temperatures and lower Mo contents (comparing ternary Cr-Mo-Si with Mo rich Cr-Mo-Si-Ni-Al system in Fig. 2 (a)) by the addition of Ni and Al.

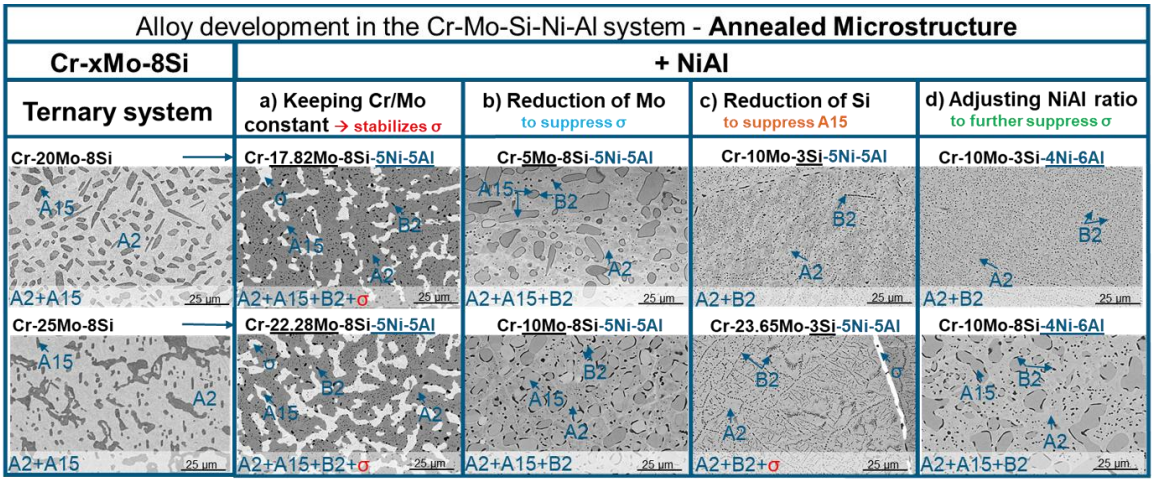

Fig. 2. SEM-BSE overview of microstructures in the Cr-Mo-Si +Ni-Al alloy system after heat treatment in Ar/5%H2 at 1400°C for 10 h and aging at 1200°C for 100 h followed by furnace cooling. Micrographs ordered in terms of changes compared to the ternary system: (a) keeping Cr/Mo constant-, (b) reduction of Mo-, (c) reduction of Si, and (d) adjustment of Ni/Al ratio.

Reducing the Mo content further (Fig. 2 (b)) destabilizes the σ phase. For Mo ≤ 10 at.%, the σ phase is fully decomposed after the two-step heat treatment and, accordingly, the A15 phase forms which was not present in the as-cast state. In this alloy system, the NiAl-B2 phase does not show a homogeneous distribution within the A2 matrix. Instead, it preferably decorates the A2-A15 interface, which provides the high-energy location to function as a nucleation site for B2. Another reason for B2 to nucleate at the interface of A2 and A15 could be to reduce the overall interfacial energy and strain of the alloy. This would be the case if the lattice misfit of B2 and A15 was lower than that of A2 and A15. However, A2 and B2 have a very similar lattice parameter [9, 11] and thus both should not be very compliant with the A15 lattice. In order to investigate the interfaces of A2-B2 and A2-B2-A15 in more detail, EBSD measurements were carried out and are shown in Fig. 3.

The crystallographic orientation maps of Cr-10Mo-8Si-5Ni-5Al presented in Fig. 3 (c) show a consistent orientation relationship between the B2 phase and the A2 matrix. No obvious reduction of misorientation can be observed at the location

where NiAl-B2 decorates the interface of Cr-A2 and Cr_3Si-A15. However, the 70° inclination of the sample (necessary for EBSD measurements) revealed a recession of NiAl phase after the grinding and polishing procedure, which likely influenced the measurement.

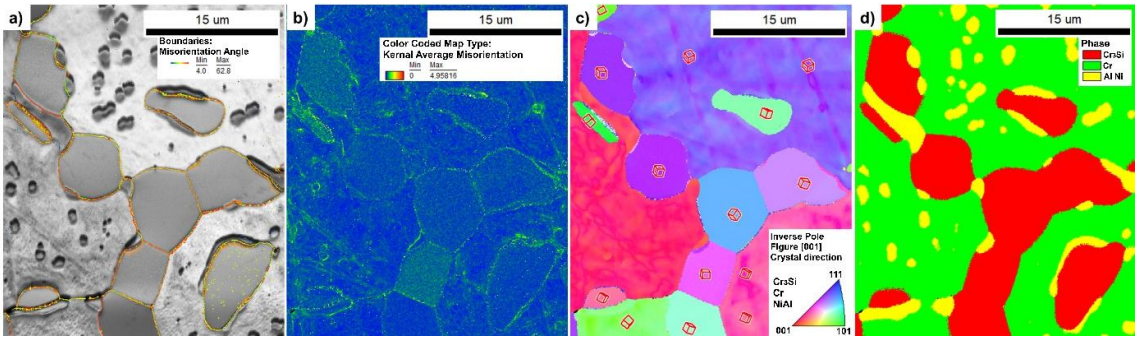

Fig. 3. EBSD images of Cr-10Mo-8Si-5Ni-5Al: (a) boundary misorientation angle, (b) KAM map, (c) crystal direction, and (d) the location of the three different phases (combined EBSD + EDS signals).

Interestingly, when the area fraction and morphology of the A15 phase (determined from cross-sectional analysis) in Cr-10Mo-8Si-5Ni-5Al (Table I) is

Table I. EPMA/WDS data of the averaged point measurements for phase and overall composition (as described in the experimental section) and phase fraction determined from BSE images of various annealed Cr-Mo-Si-Ni-Al alloys.

Nominal	Phase	Cr (at.%)	Mo (at.%)	Si (at.%)	Ni (at.%)	Al (at.%)	Area %
Cr-5Mo-8Si-5Ni-5Al	All	77.4 ± 0.5	5.1 ± 0.1	8.1 ± 0.1	4.7 ± 0.3	4.7 ± 0.3	100.0
	A2	86.1 ± 0.6	5.4 ± 0.1	4.2 ± 0.1	2.0 ± 0.3	2.3 ± 0.3	68 ± 5
	A15	71.6 ± 0.3	5.3 ± 0.1	19.9 ± 0.3	1.6 ± 0.1	1.5 ± 0.2	26 ± 5
	B2*	–	–	–	51.5 ± 1.1	48.5 ± 1.1	6 ± 1
Cr-10Mo-8Si-5Ni-5Al	All	71.5 ± 0.3	10.1 ± 0.1	8.2 ± 0.1	5.2 ± 0.2	5.1 ± 0.3	100.0
	A2	80.7 ± 0.3	10.7 ± 0.1	4.0 ± 0.1	2.2 ± 0.2	2.4 ± 0.2	65 ± 5
	A15	66.3 ± 0.2	10.9 ± 0.1	19.3 ± 0.2	1.8 ± 0.1	1.8 ± 0.3	29 ± 5
	B2*	–/–	–/–	–/–	51.9 ± 0.9	48.1 ± 0.8	6 ± 1
Cr-17.82Mo-8Si-5Ni-5Al	All	63.0 ± 0.5	17.9 ± 0.2	7.S ± 0.2	5.7 ± 0.4	5.6 ± 0.4	100.0
	A2	74.0 ± 0.6	17.2 ± 0.3	3.2 ± 0.2	2.1 ± 0.4	3.4 ± 0.4	52 ± 5
	A15	59.9 ± 0.3	18.1 ± 0.2	17.7 ± 0.4	1.7 ± 0.1	2.5 ± 0.2	24 ± 5
	B2*	–/–	–/–	–/–	50.6 ± 0.7	49.4 ± 0.7	5 ± 1
	σ	55.2 ± 0.6	24.7 ± 0.3	10.5 ± 0.2	7.2 ± 0.4	2.4 ± 0.4	19 ± 2
Cr-22.28Mo-8Si-5Ni-5Al	All	58.2 ± 0.3	22.0 ± 0.2	7.7 ± 0.2	6.0 ± 0.3	6.1 ± 0.3	100.0
	A2	70.6 ± 0.3	21.1 ± 0.2	2.8 ± 0.1	1.7 ± 0.2	3.9 ± 0.2	44 ± 5
	A15	55.7 ± 0.5	22.7 ± 0.2	16.7 ± 0.4	1.6 ± 0.4	3.4 ± 0.2	21 ± 5
	B2*	–/–	–/–	–/–	51.2 ± 1.2	48.8 ± 1.2	6 ± 1
	σ	53.0 ± 0.3	27.6 ± 0.3	10.3 ± 0.2	5.3 ± 0.3	2.3 ± 0.3	29 ± 1
Cr-10Mo-8Si-4Ni-6Al	All	71.7 ± 0.2	10.3 ± 0.1	7.7 ± 0.1	4.2 ± 0.1	6.1 ± 0.1	100.0
	A2	80.4 ± 0.2	10.9 ± 0.1	3.5 ± 0.1	1.4 ± 0.1	3.8 ± 0.1	65 ± 2
	A15	66.9 ± 0.3	11.0 ± 0.1	18.5 ± 0.3	1.2 ± 0.1	2.4 ± 0.1	29 ± 2
	B2*	–/–	–/–	–/–	49.2 ± 0.2	50.8 ± 0.2	5.9 ±0.5
Cr-10Mo-3Si-5Ni-5Al	All	76.6 ± 0.3	10.1 ± 0.1	3.0 ± 0.1	5.2 ± 0.2	5.0 ± 0.2	100.0
	A2	81.6 ± 0.4	10.7 ± 0.1	3.2 ± 0.1	2.2 ± 0.2	2.2 ± 0.2	94 ± 1
	B2*	–/–	–/–	–/–	51.6 ± 0.3	43.4 ± 0.3	6 ± 1
Cr-23.65Mo-3Si-5Ni-5Al	All	62.5 ± 0.3	23.5 ± 0.2	2.9 ± 0.1	4.7 ± 0.8	6.4 ± 0.8	100.0
	A2	66.7 ± 0.3	25.0 ± 0.2	3.0 ± 0.1	1.7 ± 0.1	3.6 ± 0.1	92 ± 1
	B2*	–/–	–/–	–/–	50.1 ± 0.8	49.9 ± 0.8	6 ± 1
	σ	51.6 ± 1.1	29.6 ± 0.4	10.1 ± 0.4	6.2 ± 0.3	2.5 ± 0.1	2 ± 1
Cr-10Mo-3Si-4Ni-6Al	All	76.4 ± 0.3	10.1 ± 0.1	2.9 ± 0.1	4.3 ± 0.2	6.3 ± 0.2	100.0
	A2	81.0 ± 0.3	10.7 ± 0.1	3.1 ± 0.1	1.6 ± 0.2	3.6 ± 0.2	94 ± 1
	B2*	–/–	–/–	–/–	49.3 ± 0.7	50.7 ± 0.7	5.7 ±0.5

–/–=>not measurable –=> not present*assuming no solubility for Mo, Si and Cr in B2

compared to that of Cr-10Mo-8Si from [11], it is about 10 % higher and the precipitates are less elongated for the NiAl-containing system and rather large (5-20 µm). Ni and Al additions thus have an influence on the shape of the A15 precipitates and thus likely on the interfacial energy. To understand the reason for the higher amount of A15, the compositions of A2 and A15 were compared in the Cr-xMo-8Si system [11] versus the Cr-xMo-8Si-5Ni-5Al system (Fig. 4 (a-c)). Fig. 4 (a) focuses on the influence of Mo content in A2 and A15 phase on the Si solubility in both phases and compares the ternary Cr-xMo-8Si system [11] and the quinary Cr-xMo-8Si-5Ni-5Al system. Fig. 4 (b) depicts the Ni, Al content in A2 and A15 versus their Mo content, in order to reveal if there is a similar dependency on Mo content for these elements (as observed for Si [11]). In Fig. 4 (c) the distribution coefficient, k, for Mo versus the overall Mo content in the ternary and quinary alloys is compared.

In Fig. 4 (a) the Si content in A2 and A15 as a function of the Mo content in the phases is depicted. The solubility of Si in A2 is comparable between both systems until a Mo threshold of 10 at.%. For higher Mo contents the Si content in A2 is reduced in the Cr-xMo-8Si-5Ni-5Al system compared to the ternary system, while at the same time the stability regime of the σ phase is reached. This suggests that the formation of the σ phase reduces the amount of Si retained in A2 (and A15), likely due to preferential partitioning of Si into σ.

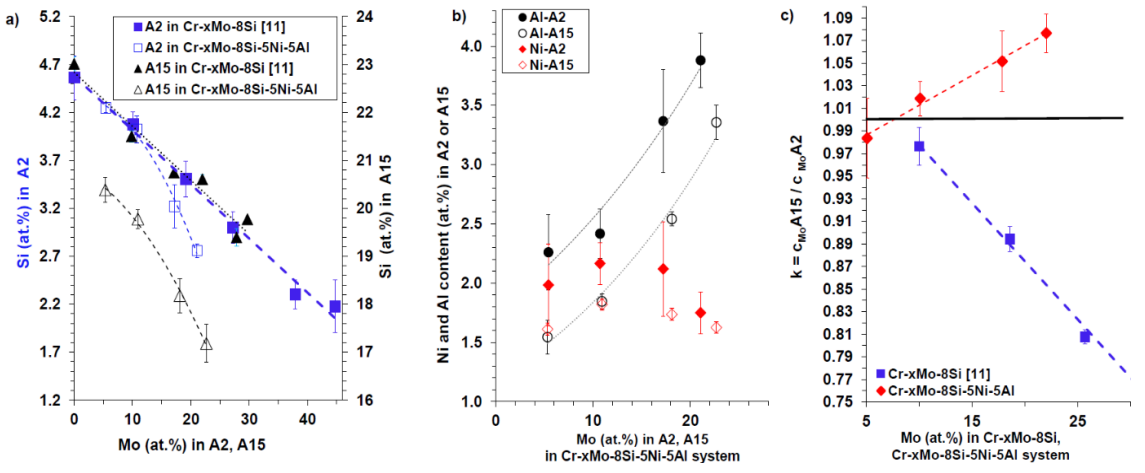

Fig. 4. Comparison of A2 and A15 phase compositions in Cr-xMo-8Si [11] versus Cr-xMo-8Si-5Ni-5Al [this work]; WDS measurements taken after heat treatment at 1400°C for 10 h followed by aging at 1200°C for 100 h showing: (a) Si solubility, (b) Al and Ni solubility, and (c) Mo distribution depending on the Mo content.

In the A15 phase, the Si content is also strongly reduced for the Ni- and Al-containing system for low Mo contents. The Cr-xMo-8Si-5Ni-5Al system shows additional solubility of Ni and Al (Fig. 4 (b)) in A15, which may correlate with the overall lower Si content compared to the ternary system. Fig. 4 (b) shows that Al solubility increases in A2 and A15 with increasing Mo content, whereas Ni solubility is unaffected and remains constant. For A2, these additional solutes do not affect Si solubility as much as in the A15 phase, but they do change the distribution of Mo between both phases. In Fig. 4 (c) the distribution coefficient, k, for Mo in A15 and A2 versus the overall Mo content is depicted, showing an increased amount of Mo in the A15 phase with increasing overall Mo content, while the reverse was observed in ref. [11] for the ternary Cr-xMo-8Si system.

These compositional studies can explain why there is more A15 formed in the Cr-xMo-8Si-5Ni-5Al system than in the ternary system. For the same overall Si content, less incorporation of Si into the A15 phase leads to an increase of A15 fraction to compensate for the reduced Si solubility. This relationship holds true at least for compositions without the σ phase. For the ternary system, it was observed that increasing the Mo content in the A15 phase leads to higher amount of A15 phase due to reduced Si solubility in A15, and thus shifts the phase boundary of the A2 and A2+A15 phase field, as presented in the pseudo binary Cr/Mo-Si diagram in ref. [11]. In the quinary system studied in this work, this effect is amplified by the presence of Ni and Al in A15, which further reduces Si solubility in A15.

To suppress A15 precipitates in the Cr-Mo-Si-Ni-Al system and fully replace them by the B2 intermetallic phase, the Si content in the alloys was reduced to 3 at.%, which is the maximum solubility for Si in A2 at 1200°C in Cr-25-Mo-8Si [11]. Fig. 2 (c) shows the two chosen compositions with 10 and 23.65 at.% Mo (in order to keep the Cr/Mo ratio of 2.68 as in Cr-25Mo-8Si). For Cr-10Mo-3Si-5Ni-5Al the goal of creating a two phase A2-B2 microstructure with fine spherical[2], sub micron (580 ± 280 nm) B2 particles was achieved. The sample with higher Mo content contains σ phase along the grain boundaries, despite the low overall amount of

[2] The term *cuboida*l used in the original publication should read *spherical*. This correction does not affect the results or conclusion.

Si, which can be explained by the reduced Si solubility for A2 depicted in Fig. 4 (a)). To inhibit σ phase formation in Cr-xMo-3Si-5-Ni-5Al, a maximum of 17 at.% Mo is allowed so that the 3 at.% Si remains fully soluble in the A2 matrix. Shifting the Ni/Al ratio to lower values can also help to destabilize σ phase formation as explained in section "*Microstructural observations and characterization of the as-cast condition"*. The EPMA/WDS measurements of the annealed alloys listed in Table I confirm that the σ phase consists of up to 7 at.% Ni.

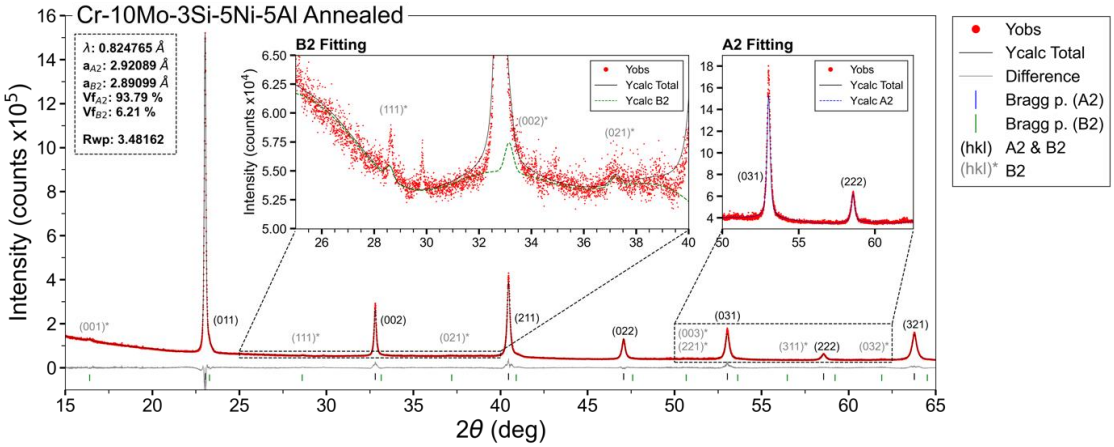

Fig. 5. Powder SXRD pattern for Cr-10Mo-3Si-5Ni-5Al after heat treatment at 1400°C for 10 h and aging at 1200°C for 100 h. Patterns were analyzed in TOPAS-v5 using Rietveld refinement to output lattice parameters and volume fractions of A2 and B2.

Powder SXRD was conducted after annealing of the A2-B2 alloy Cr-10Mo-3Si-5Ni-5Al and analyzed using Rietveld refinement within TOPAS-v5 (Fig. 5). The calculated intensities showed a good fit with a weighted profile R-factor (Rwp) ~ 3.48. Addition peaks can be identified to be caused by the presence of Al_2O_3 incorporated in the powder during the manufacturing process; such peaks will not influence the measurement of lattice parameter of the constituent phases. A2 and B2 lattice parameters were calculated based on the assumption of a (Cr,Mo) A2 matrix phase and B2-NiAl precipitate phase resulting in lattice parameters of 2.9209 and 2.8901 Å, respectively. The lattice parameter of the B2 phase appears very similar to that found in ref. [9] indicating a very low solubility of the Cr-Mo matrix within the B2-NiAl phase. The addition of Mo, which has a larger atomic radius than Cr, leads to an increase in the lattice parameter of the matrix phase, compared to undoped Cr (2.8854 Å) and Cr-10Fe (2.8829 Å) [9]. From SXRD alone, it is hard to deduce the partitioning of the Si within the alloy where

it is expected to be predominantly in the matrix phase; however, a slight increase in the lattice parameter of the B2 phase from 2.8895 Å in Cr-5Ni-5Al [9] to 2.8901 Å in Cr-10Mo-3Si-5Ni-5Al could indicate a slight effect of Si on the precipitate phase.

The lattice misfit (δ) between the A2 and B2 system can be calculated by:

$$\delta = \frac{2(a_{B2} - a_{A2})}{a_{B2} + a_{A2}} \quad (3)$$

Using Eq. (3), the lattice misfit between the A2 and B2 phases within Cr-10Mo-3Si-5Ni-5Al can be calculated to be -1.05 %. Naturally, the incorporation of Mo into the matrix and resulting larger lattice parameter has increased the misfit over alloys without Mo (Cr-5Ni-5Al δ = 0.14% [9]). From Ni-based alloys, it is known that this misfit is an important parameter when it comes to the microstructural stability and high temperature creep. It is also possible to obtain the volume fraction of each phase from Rietveld refinement with Vf_{A2} = 93.79% and Vf_{B2} = 6.21%, which is in line with measurements made via image analysis (Table I).
Crystallographic orientation maps of the A2-B2 alloy Cr-10Mo-3Si-5Ni-5Al (not shown here due to similarity to what is presented in Fig. 3 (c) also show a consistent orientation relationship between the B2 phase and the A2 matrix. While this does not provide sufficient evidence of interface coherency, such an orientation relationship, combined with the observed microstructural stability, suggests that the B2 phase forms stable precipitates that can contribute to mechanical strengthening at high service temperatures. The B2 precipitates maintain a spherical[3] morphology and sub-micron size even after aging at 1200°C for 100 h, indicating a high degree of thermal stability. Although the interfaces of the larger (>500 nm) precipitates studied here are most likely semi-coherent or incoherent, prior transmission electron microscopy (TEM) studies of Ma et al. [9] have shown smaller NiAl precipitates (25 ± 7 nm) can adopt coherent interfaces in a Cr-5 at.%Fe matrix. Such finer-scale features would not be detectable in the present SEM-based characterization. Therefore, while the current observations

[3] The term *cuboida*l used in the original publication should read *spherical*. This correction does not affect the results or conclusion.

demonstrate the stability of larger precipitates, future TEM investigations will be required to determine whether smaller coherent or semi-coherent precipitates are also present.

When compared to the CALPHAD predictions for the pseudo binary phase diagram Cr – Ni + Al and Cr(Fe) – Ni + Al presented in ref. [9], it is observed that, unlike Fe, Mo(+Si) addition to Cr, it does not increase the solubility for Ni + Al in the matrix but seems to decrease it. While 5.8 at.% Ni + Al are soluble in pure Cr, substituting 10 at.% of Cr with Fe can increase solubility of Ni + Al to 8.3 at.% [9] at 1200°C. In the investigated alloy Cr-10Mo-3Si-5Ni-5Al, developed in this work, the solubility of Ni + Al is limited to 4.4 at.% at 1200°C (Table I). When taking into account this shift in the A2 – A2+B2 phase field, an optimized heat-treatment procedure can be developed in future studies. However, the applied heat treatment resulted in the microstructure that was desired (A2 matrix with fine sub-micron B2 precipitates), and examining one representative composition Cr-10Mo-3Si-5Ni-5Al, after the 1400°C/10 h homogenization step (prior to aging), confirmed a single-phase microstructure proofing full solubility of 5 at.% Ni + 5 at.% Al in the Cr-10Mo-3Si matrix at 1400°C. The compositional data provided in this work can serve as a valuable dataset for future thermodynamic modeling efforts to design an optimized heat treatment and provide information on the full stability regime of the A2-B2 two-phase system.

Hardness and fracture toughness

Selected Cr-Mo-Si-Ni-Al compositions from Fig. 2 (a-c) were analyzed with HV1 Vickers hardness testing. In Fig. 6 (a) their hardness values are compared to the ternary system Cr-Mo-Si from [12]. In Fig. 6 (b) the respective HV1 imprints and the microstructures are shown. As expected at room temperature, the dominant influence on hardness in the Cr-Mo-Si system was determined to be the solid solution hardening [12]; thus, the hardness values for samples with the same Mo content are compared. Cr-10Mo-3Si-5Ni-5Al, composed of an A2 matrix and B2 precipitates, reaches a hardness value of 5.6(1) GPa, which is comparable with Cr-10Mo-8Si composed of an A2 matrix and A15 precipitates, showing a hardness of 5.1(1) GPa. Thus, ca. 22 area% of A15 in Cr-10Mo-8Si [11] show a similar but slightly lower effect on the overall hardness than the Cr-10Mo-3Si-5Ni-5Al alloy strengthened by ca. 6 area% (Table I) B2 phase. Cr-10Mo-8Si-5Ni-5Al

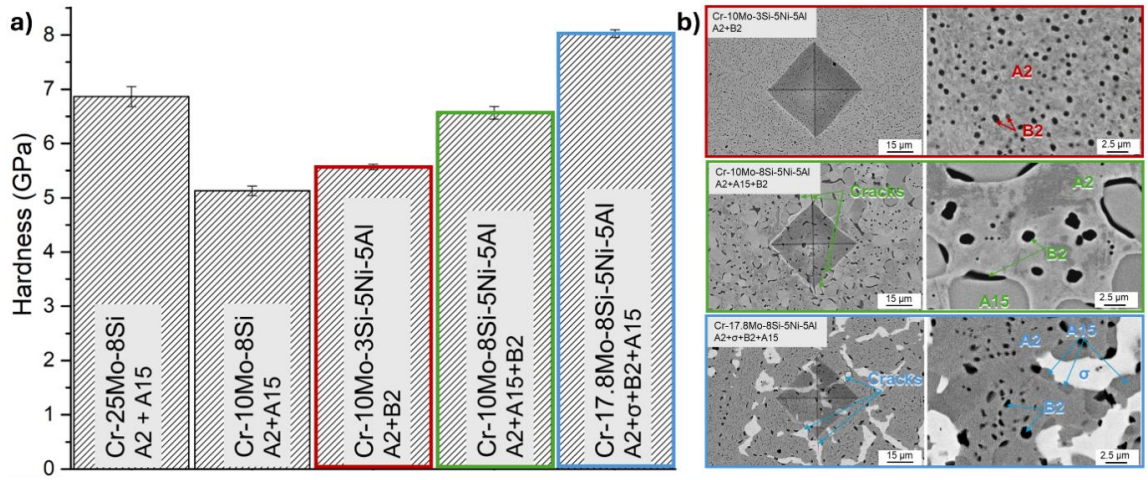

Fig. 6. (a) RT Hardness values of Cr-xMo-8Si samples from [12] versus investigated Cr-Mo-Si-Ni-Al alloys (b) HV1 Vickers imprints and microstructure of tested Cr-Mo-Si-Ni-Al alloys

contains both A15 and B2 precipitates in an A2 matrix and thus shows a higher hardness value of 6.6(1) GPa. Even though the Vickers load was as low as 1 kgf/mm² (circa 9.81 MPa), cracks are observed in the larger A15 phase (up to ~10 µm). Similar observations were reported in ref. [12] for the A15 phase in Cr-xMo-8Si for large A15 precipitates. No cracks were observed for the A2 + B2 system, which could be indicative of A15 being more brittle than the B2 phase or more simply related to the smaller size of the B2 precipitates compared to the A15 phase.

Cr-17.8Mo-8Si-5Ni-5Al, containing A15, B2 and the σ phase distributed in an A2 matrix, gives the highest hardness value of 8.0(1) GPa, but at the same time the σ phase shows strong cracking along the Vickers imprint, emphasizing its brittleness. The larger size of the A15 phases likely influences the larger standard deviations observed within A15 containing alloys where the indentation interacts with different amounts of A15 phase.

Vickers hardness tests at higher loads (HV30) were performed to see if replacing the A15 with B2 precipitates has a beneficial influence on the fracture toughness with optical imprints shown in Fig. 7. In the upper row, Cr-10Mo-3Si-5Ni-5Al (A2+B2) is compared to the A2+A15 system Cr-xMo-8Si (x = 10, 25) studied in ref. [12]. According to [29], the crack length formed at high Vickers loads can be correlated to the fracture toughness, K_I, by:

$$K_I = \frac{F}{(\pi \cdot c)^{3/2} \tan(\alpha)} \quad (4)$$

where F is the test load k(kg), c the crack length + half of the indentation diagonal length (mm), and α the opening angle of the Vickers pyramid (136°). Units were converted using: $MPa \cdot m^{0.5} = 0.3101\ kg/mm^{1.5}$.

For the A2 + A15 system, the maximum K_I measured was 10 $MPa \cdot m^{0.5}$ (Cr-40Mo-8Si) [12], which is lower than the accepted minimum of 15 $MPa \cdot m^{0.5}$ for structural materials [30]. Single-phase A2 systems solid-solution strengthened by Mo and Si do not show crack formation [12], and thus can be expected to be > 10 $MPa \cdot m^{0.5}$. However, with the addition of A15 to the Cr-Mo-Si system, the fracture toughness derived from Vickers HV30 tests decreases down to a minimum of 3.7 $MPa \cdot m^{0.5}$ (Cr-20Mo-8Si) [12]. Fig. 7 compares the A2 + B2 system developed in this work versus the Cr-xMo-8Si compositions studied in ref. [12]. No cracks were initiated during HV30 testing of Cr-10Mo-3Si-5Ni-5Al (A2 + B2) while Cr-10 and 25Mo-8Si (A2+A15) show low fracture toughness as indicated by cracking and discussed above. For comparison, also the A2 + A15 + B2 and A2 + A15 + B2 +

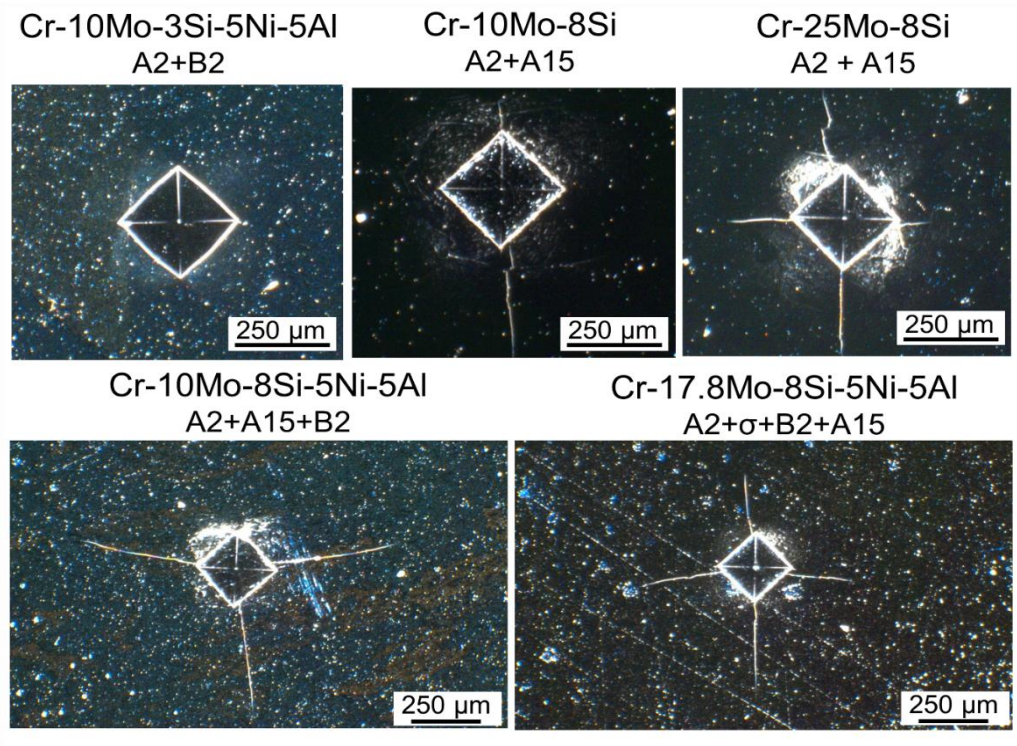

Fig. 7. Stereo micrographic images of HV30 Vickers imprints on Cr-Mo-Si(-Ni-Al) alloys. Cracking around the indents can be observed with the addition of the A15 phase to the microstructure.

σ alloys were tested, showing even stronger crack propagation (> 250 µm) and thus even worse fracture toughness when compared to the A2 + A15 system. These results confirm that replacing A15 with B2 leads to an enhanced fracture toughness at room temperature.

Compressive strength

The newly developed Cr-Mo-Si-Ni-Al alloys were compressively tested to get a first impression of their strength at various temperatures in comparison to Cr-xMo-8Si alloys in ref. [12]. In a first trial, the alloys showing low fracture toughness during the HV30 Vickers tests (Cr-10Mo-8Si-5Ni-5Al and Cr-17.8Mo-8Si-5Ni-5Al) were compressively tested at 21 and 500°C and compared to Cr-10Mo-3Si-5Ni-5Al (A2 + B2) vs. Cr-10Mo-8Si (A2 + A15) [12] (Fig. 8).

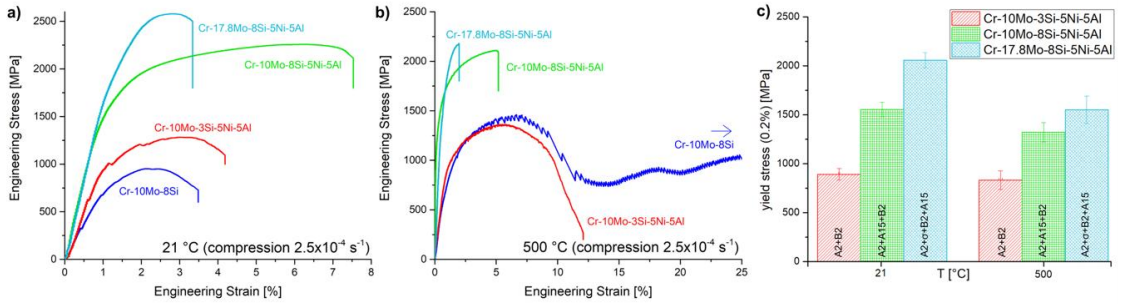

Fig. 8. Stress vs. strain curves for compressively tested Cr-Mo-Si-Ni-Al alloys compared to the Cr-10Mo-8Si (A2+A15) alloy from [12] at: (a) 21°C and (b) 500°C; and (c) determined yield stress (0.2% offset). Stress and strain values were obtained from Eqs. (1) and (2).

The A2 + A15 + B2 and σ systems show much higher yield stress due to the high content of strengthening intermetallic phases. Especially the σ phase-containing Cr-17.8Mo-8Si-5Ni-5Al has a high yield stress > 2000 MPa at 21°C, but a low strain at rupture of ca. 3.5%, comparable to the A2 + A15 Cr-10Mo-8Si alloy. Strain at rupture for the A2 + B2 system (Cr-10Mo-3Si-5Ni-5Al) sample increased but stayed below 5%. Surprisingly, the samples containing both forms of precipitates and performing badly in the fracture toughness test by Vickers show a strain at rupture up to 7.5%, comparable to Cr-25Mo-8Si (6%) and Cr-8Si (9%) [12]. It should be emphasized that the strain to rupture is improved for the A2 + B2 and A2 + A15 systems at 500°C, while it is lowered for the more complex microstructures containing multiple intermetallic phases. It should be noted that while compressive tests do not directly corelate to tensile properties, especially

for BCC systems, they provide a useful technique to screen for mechanical performance of novel alloy designs. Additionally, due to the Poisson's ratio and conservation of mass during compression, larger strain values will have a significantly different cross-sectional area which would influence the calculated stress. This is especially true for larger strain values, and therefore caution should be taken when interpreting results at high strain values. Nevertheless, the full stress-strain curve is provided for a clear indication of the actual fracture strain and better comparability with results on the ternary system presented in ref. [12]. Due to the promising behavior of the A2 + B2 system in the high-load Vickers tests, indicating suitable fracture toughness, further comparisons focused on Cr-10Mo-3Si-5Ni-5Al (A2 + B2) versus Cr-10Mo-8Si (A2 + A15) [12]. Cr-10Mo-3Si-5Ni-5Al was tested at 21, 300, 500, 700, 900, and 1000°C. Additionally, Cr-10Mo-8Si and Cr-25Mo-8Si investigated in ref. [12] were tested at 1000°C. The resulting stress-strain curves are plotted in Fig. 9. Strain at rupture in Cr-10Mo-3Si-5Ni-5Al increases with increasing temperature up to circa 17% at 700°C. No rupture was initiated for higher temperatures. For Cr-10Mo-8Si (A2 + A15) reported in ref. [12] no complete rupture occurred for temperatures ≥ 300°C, but a major stress drop

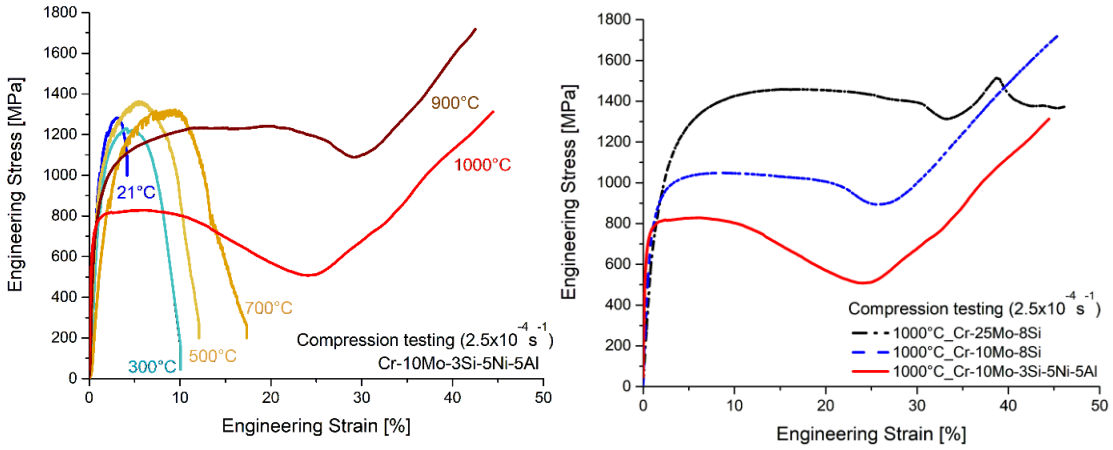

Fig. 9. Compressive stress-strain curves for the most promising Cr-Mo-Si-(Ni-Al) alloy focusing on: (a) stress-strain of Cr-10Mo-3Si-5Ni-5Al vs. temperature, and (b) stress-strain at 1000°C for A2-B2 (Cr-10Mo-3Si-5Ni-5Al) versus two A2+A15 alloys (Cr-10 and 25 at%Mo-8Si).

was observed (indicating cracking) at 8% strain at 700°C. The deformation mechanisms do seem to differ in both systems. In the A2 + A15 system, some stress relaxation by microcracking as observed in ref. [12] is possible and prevents full rupture, while the low misfit B2 particles in the A2 + B2 system are

stronger obstacles for dislocation motion, but, once the localized stresses are too high, full rupture occurs. Deformation in a single-phase Cr-36.1Mo-3Si system was intensively studied in ref. [31], describing both dislocation slip and deformation twinning as low-temperature deformation mechanisms. Combining these results with the HV30 tests indicates that the A2 + B2 system offers a higher strength and fracture toughness than the A2 + A15 system, but a lower extent of plastic deformation before failure (equivalent to ductility) in compressive testing. The Cr-10Mo-3Si-5Ni-5Al cylinders failed at a 45° angle during compressive testing, indicating shear failure.

The yield stress (0.2% offset) was plotted and compared to relevant literature data including strain rates (if available) in Fig. 10. Ni-based superalloys IN718 [32] and MAR-M247 [33] are included as a benchmark with the Cr-Fe-Ni-Al [9] system for comparison. The overall yield stress versus temperature is comparably high for the Cr-10Mo-3Si-5Ni-5Al (A2 + B2) and Cr-10Mo-8Si (A2 + A15) system. The yield stress below 600°C for both alloys is lower than that of

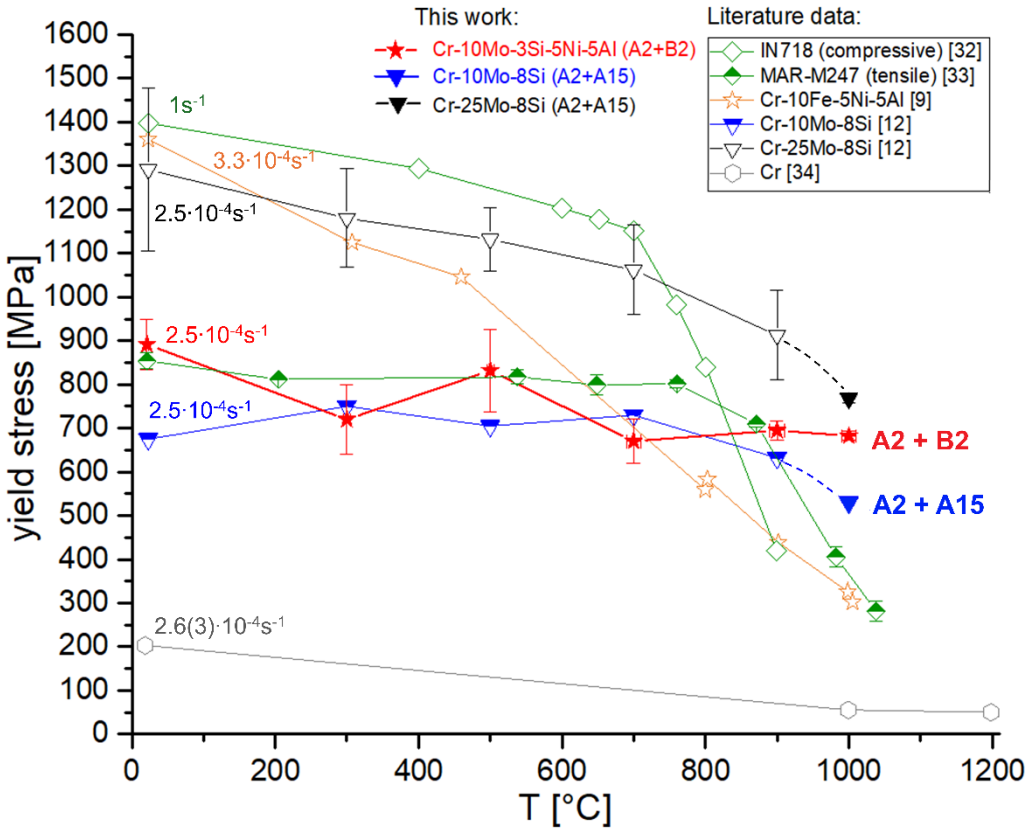

Fig. 10. Yield stress versus temperature from this work and literature data (IN718 [32], MAR-M247 [33], Cr-10, 25 at%Mo-8Si [12], Cr-10Fe-5Ni-5Al [9], Cr [34]).

the strongest Ni-based superalloy IN718 (with $T_{service}$ up to 650°C), but comparable to MAR-M247 used at service temperatures up to 1000°C [33]. Above 700°C IN718 [32] loses strength due to dissolution of its precipitates, while for MAR-M247 [33] this phenomenon is shifted to higher temperatures. Up to the highest tested temperature of 1000°C, the Mo-alloyed B2-strengthened alloy Cr-10Mo-3Si-5Ni-5Al does not show a significant strength loss, while the A2 + A15 system, as well as the B2-strengthened system with Fe [9], shows a reduction in yield stress, with the latter dropping beneath the MAR-M247 benchmark at 800°C. It was previously observed in ref. [12] that the single-phase Cr-36.1Mo-3Si material from [31] shows similar temperature dependence of the yield stress as the two-phase Cr-20Mo-8Si [12], indicating that the A15 phase distribution in such alloys does not effectively block dislocation motion. Even after improved heat treatment of Cr-10Mo-8Si, as proposed in ref. [12], the A15 precipitates range between 1 and 30 µm and their distribution remains non-homogeneous. Due to the fabrication method of arc-melting and their high lattice misfit with the matrix phase, A15 precipitates are too coarse and are too widely spaced, making them ineffective in decreasing dislocation mobility. In contrast, the low misfit B2 precipitates have a high precipitation-strengthening effect and are finely distributed within the matrix, with a size in the range of ~ 600 nm. This leads to the conclusion that the B2 precipitates, combined with the Mo solid solution strengthening, are responsible for retaining the yield stress up to 1000°C and possibly beyond in the A2-B2 alloy Cr-10Mo-3Si-5Ni-5Al.

Thus, it is concluded that a Mo and Si solid-solution-strengthened Cr-A2 matrix can strongly benefit further from precipitation strengthening via NiAl precipitates. The limits of beneficial Mo and Si alloying in this system were successfully identified. With NiAl as a suitable barrier for dislocation motion in the nitridation- and oxidation-resistant Cr-Mo-Si matrix, such BCC superalloys show a high potential as a novel high-temperature material.

Conclusions and Outlook

A2-B2 strengthening in the Cr-Mo-Si system was investigated by introducing Ni and Al. By the addition of Ni and Al to Cr-Mo-Si alloys the brittle σ phase is stabilized, which limits the compositional freedom and needs to be addressed

through alloy optimization, as demonstrated for the Mo, Si and Ni content in the Cr-Mo-Si-Ni-Al system. The compositional data provided in this work can serve as a valuable dataset for future thermodynamic modeling efforts in the system. The addition of Ni and Al reduces the Si content in the A15 phase, leads to Mo enrichment in A15 (opposite to what was observed for the Cr-Mo-Si system [11]) and also results in a higher volume fraction of A15 in Cr-10Mo-8Si-5Ni-5Al compared to Cr-10Mo-8Si for the same overall amount of Mo and Si.

A Mo and Si solid-solution-strengthened Cr-A2 matrix and NiAl-B2 precipitation-strengthened superalloy was demonstrated for the composition of Cr-10Mo-3Si-5Ni-5 at.%Al. Compression tests showed a superior precipitation strengthening effect for B2 compared to A15 at high temperatures. Remarkably, high-load Vickers tests (HV30) indicated that the B2 precipitates have no apparent detrimental effect on the low temperature fracture toughness, in contrast to the A15 phase.

The findings presented here describe a novel design strategy for next-generation Cr-based BCC superalloys. Future work in the field should investigate the fracture mechanisms of Cr-10Mo-3Si-5Ni-5Al in tensile tests, high temperature creep strength, and the high temperature oxidation resistance to compare the A2-B2 system to the inherently very oxidation-resistant A2-A15 system.

Acknowledgements

The authors gratefully acknowledge the German Federal Ministry for Economic Affairs and Climate Action (BMWK) for the financial support of the project under grant no. 20E2125 based on a decision of the German Bundestag, also the funding received from the European Union's Horizon 2020 research and innovation program under grant agreement No 958418 "COMPASsCO2" (https://www.compassco2.eu). The authors also acknowledge Kan Ma and the Diamond Light Source (United Kingdom) for receiving time on beamline I11 under proposal CY38725. For the possibility to perform high load Vickers tests (at Staatliche Materialprüfungsanstalt) the authors thank Jurica Filipovic, Fabrizio Windhaus, Robert Kopp and Gerwin van den Dungen from the technical university of Darmstadt. Also, the authors thank Dr. Gerald Schmidt from DECHEMA-Forschungsinstitut (DFI) for the EPMA/WDS measurements, Melanie Thalheimer for EBSD measurements, Pelle Wolf for assisting in hardness testing

and the members of the DFI workshop Heinrich Kopietz, Yvonne Hohmann, and Jano Bender for electrical discharge machining of the samples.

Conflicts of Interest

The authors declare that they have no known competing financial interests or personal relationships that could have appeared to influence the work reported in this paper.

Funding

This project is granted and financed under grant no. 20E2125 by German Federal Ministry for Economic Affairs and Climate Action (BMWK) based on a decision of the German Bundestag. This project has received funding from the European Union's Horizon 2020 research and innovation program under grant agreement No 958418 "COMPASsCO2" (https://www.compassco2.eu). The authors also acknowledge the Diamond Light Source (United Kingdom) for time on beamline I11 under proposal CY38725.

Data availability statement

The raw and processed data required to reproduce these findings are available on request (lisa.zander@dechema.de).

Appendix

See Appendix Figures 11, 12, 13.

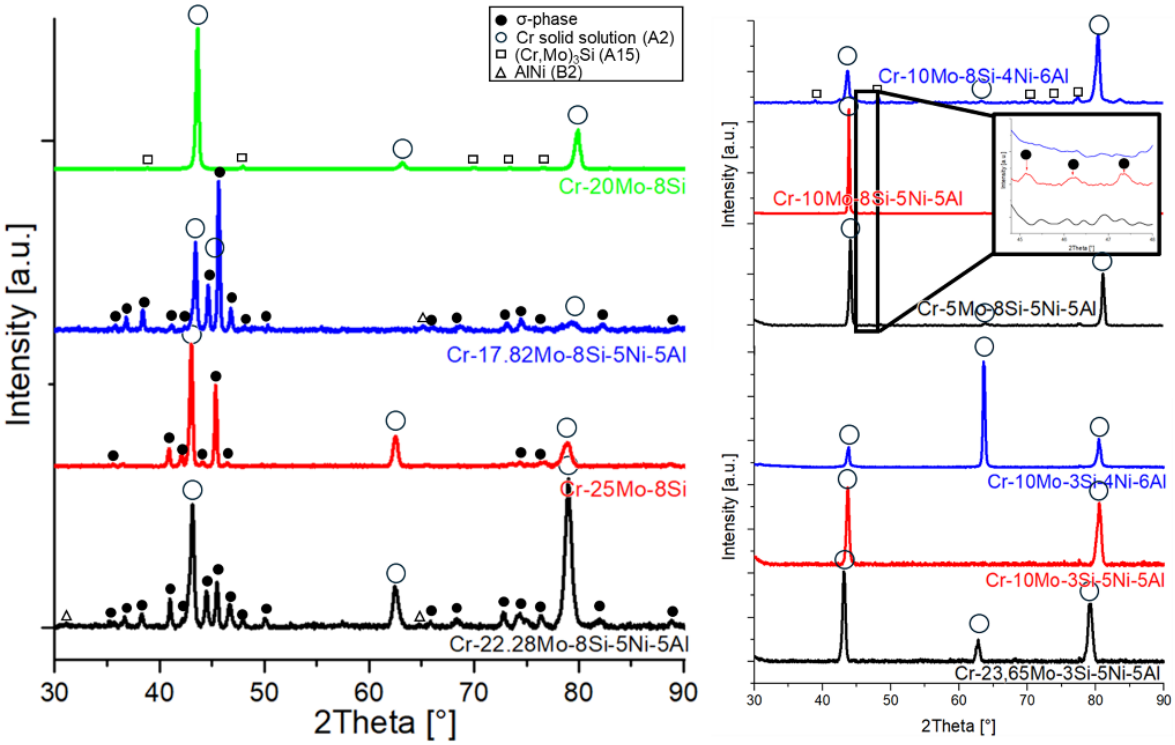

Fig. 11. XRD patterns of all investigated arc-melted alloys in the as-cast state. Identification of the presence of σ phase can be seen for Cr-17.82Mo-8Si-5Ni-5Al, Cr-25Mo-8Si, and Cr- 22.28Mo-8Si-5Ni-5Al which was successfully eliminated with a reduction in Mo and Si.

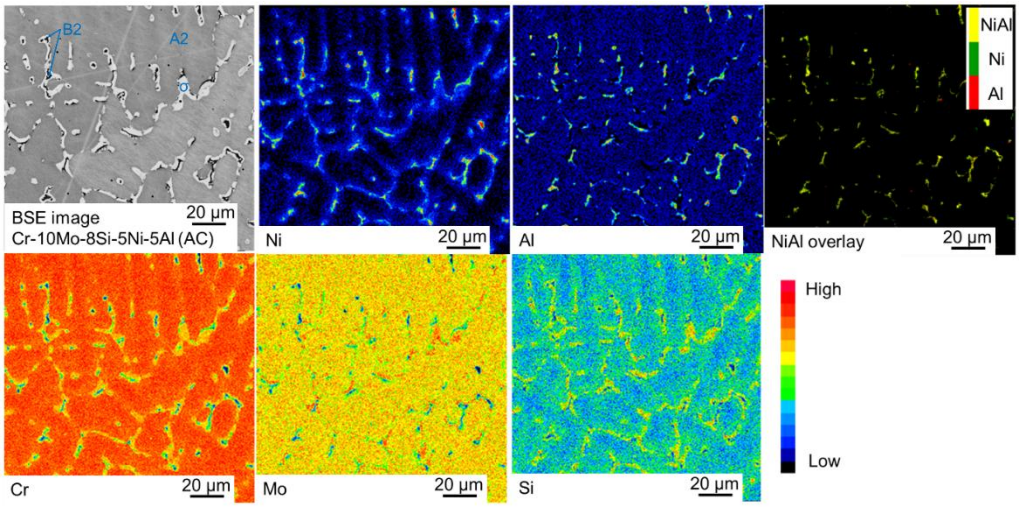

Fig. 12. Elemental EPMA/WDS-mapping of Cr-10Mo-8Si-5Ni-5Al in the as-cast (AC) state.

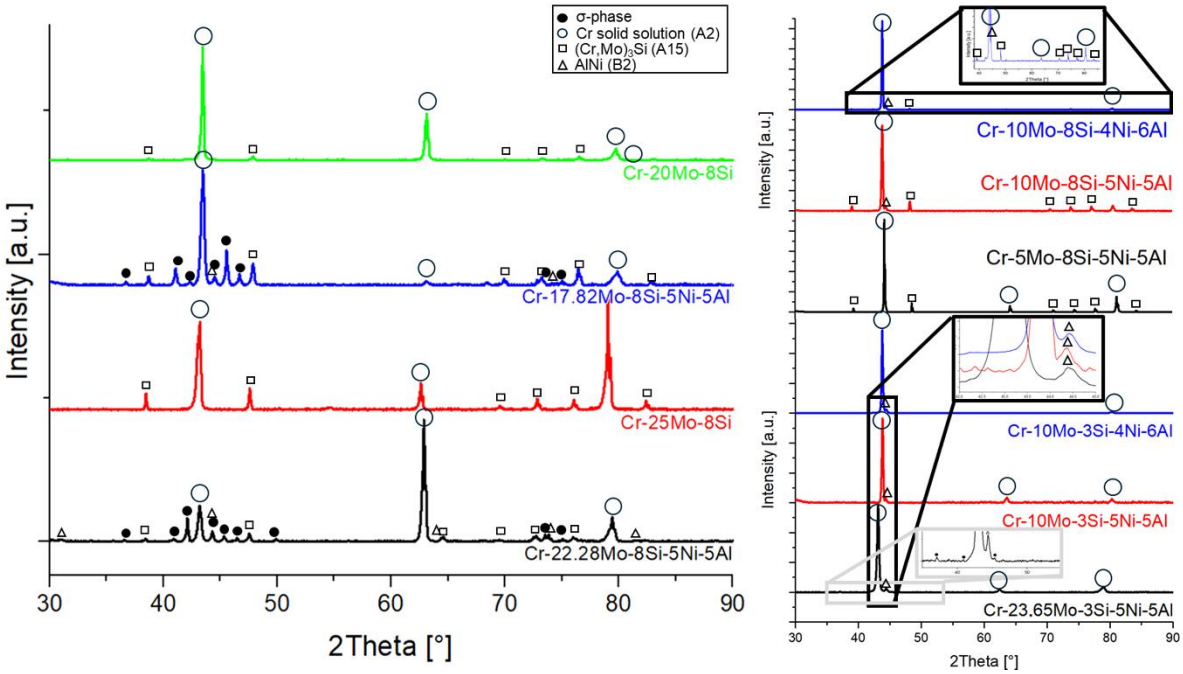

Fig. 13. XRD patterns of all investigated annealed alloys. Identification of the presence of σ phase can be seen for high Mo contents (Cr-17.82Mo-8Si-5Ni-5Al, Cr- 22.28Mo-8Si-5Ni-5Al, Cr-23.65Mo-3Si-5Ni-5Al), while B2 precipitates are confirmed for -Ni and -Al containing compositions.

References

[1] DERA, "Raw Material Price Monitor," Federal Institute for Geosciences and Natural Resources, 2024.

[2] E. M. Savitskii and G. S. Burkhanov, Physical Metallurgy of Refractory Metals and Alloys, New York: Consultants Bureau, 1970, p. 53.

[3] Y. Aono, T. Omori and R. Kainuma, "Microstructure and high-temperature strength in Cr–Si binary alloys," Intermetallics, vol. 112, p. 106526, 2019.

[4] Y. F. Gu, H. Harada and Y. Ro, "Chromium and Chromium-Based Alloys: Problems and Possibilities for High-Temperature Service," The Journal of The Minerals, Metals & Materials Society, vol. 56, pp. 28-33, 2004.

[5] F. Hinrichs, A. Kauffmann, A. S. S. D. Tirunilai, B. Beichert, G. Winkens, K. U. A. S. Beck, M. C. Galetz, Z. Long, H. Thota, Y. Eggeler, A. Pundt

and M. Heilmaier, "A novel nitridation- and pesting-resistant Cr-Si-Mo alloy," Corrosion Science, vol. 207, p. 110566, 2022.

[6] A. Solimani-Dorcheh and M. C. Galetz, "Challenges in Developing Oxidation-Resistant Chromium-Based Alloys for Applications Above 900°C," The Journal of Minerals, Metals & Materials Society, vol. 68, p. 2793–2802, 2016.

[7] P. Pfizenmaier, A. S. Ulrich, U. Glatzel and M. C. Galetz, "Tensile Creep Properties of Cr-Si Alloys at 980 °C in Air - Influence of Ge and Mo Addition," Metals, vol. 11, no. 7, pp. 1072-1080, 2021.

[8] A. S. Ulrich, P. Pfizenmaier, A. Solemani, U. Glatzel and M. C. Galetz, "Strengthened Cr-Si-base alloys for high temperature applications," International Journal of Refractory Metals & Hard Materials, vol. 76, pp. 72-81, 2018.

[9] K. Ma, T. Blackburn, J. P. Magnussen, M. Kerbstadt, P. A. Ferreirós, T. Pinomaa, C. Hofer, D. G. Hopkinson, S. J. Day, P. A. J. Bagot, M. P. Moody, M. Galetz and A. J. Knowles, "Chromium-based bcc-superalloys strengthened by iron supplements," Acta Materialia, vol. 257, p. 119183, 2023.

[10] S. V. Raj, "An evaluation of the properties of Cr,Si alloyed with Mo," Materials Science and Engineering A, vol. 201, pp. 229-241, 1995.

[11] L. Koliotassis, E. M. H. White and M. C. Galetz, "The Influence of Mo Content and Annealing on the Oxidation Behavior of Arc-Melted Cr–xMo–8Si Alloys," Advanced Engineering Materials, p. 2301906, March 2024.

[12] L. Zander, M. Kerbstadt, E. M. H. White and M. C. Galetz, "Cr-based high temperature alloys - The strengthening effect of molybdenum on chromium-silicon alloys," International Journal of Refractory Metals and Hard Materials, vol. 132, p. 107287, 2025.

[13] H. Wu, C. Li, C. Guo and Z. Du, "Experimental determination of the isothermal sections and the liquidus surface projection of the Mo-Si-Cr ternary system," Journal of Alloys and Compounds, no. 922, p. 166164, 2022.

[14] H. Wu, C. Li, C. Guo and Z. Du, "Thermodynamic assessment of the Cr-Mo-Si ternary system," Calphad, no. 83, p. 102631, 2023.

[15] W. D. Klopp, "Recent Developments in Chromium and Chromium Alloys," Journal of Metals, vol. 21, pp. 24-32, 1969.

[16] Y. Harada and M. Ohmori, "Ductile–brittle transition behavior of rolled chromium," Journal of Materials Processing Technology, Vols. 153-154, p. 93–99, 2004.

[17] H. Johanse and G. Asai, "Room-Temperature Ductile Chromium," Journal of The Electrochemical Society, vol. 101, no. 12, pp. 604-612, 1954.

[18] B. A. Wilcox, N. D. Veigel and A. H. Clauer, "Ductile-Brittle Transition of Thoriated Chromium," METALLURGICAL TRANSACTIONS, vol. 3, pp. 273-283, 1972.

[19] S. Mathieu, "On the Oxidation and Nitridation of Chromium at 1300 °C," Oxidation of Metals, no. 74, p. 79–92, 2010.

[20] L. Royer, X. Ledoux, S. Mathieu and ,. P. Steinmetz, "On the Oxidation and Nitridation of Chromium at 1300°C," Oxidation of Metals, vol. 74, pp. 79-92, 2010.

[21] A. Solimani-Dorcheh and M. C. Galetz, "Oxidation and Nitridation Behavior of Cr–Si Alloys in Air at 1473 K," Oxidations of Metals, vol. 84, pp. 73-90, 2015.

[22] D. B. Miracle, M.-H. Tsai, O. N. Senkov, V. Soni and R. Banerjee, "Refractory high entropy superalloys (RSAs)," Scripta Materialia, vol. 187, pp. 445-452, 2020.

[23] Ö. N. Dogan, X. Song, S. Chen and M. C. Gao, "Microstructural study of high-temperature Cr-Ni-Al-Ti alloys supported by first-principles calculations," Intermetallics, vol. 35, pp. 33-40, 2013.

[24] S. A. Kube, C. Frey, C. McMullin, B. Neuman and K. M. Mullin, "Navigating the BCC-B2 refractory alloy space: Stability and thermal processing with Ru-B2 precipitates," Acta Materialia, vol. 265, p. 119628, 2024.

[25] L. Royer, S. Mathieu, C. Liebaut and P. Steinmetz, "Study of the microstructure and oxidation behavior of chromium base alloys strengthened by NiAl precipitates," Materials Science Forum, Vols. 595-598, pp. 117-125, 2008.

[26] D. Locq, P. Caron, C. Ramusat and R. Mévrel, "Chromium-Based Alloys Strengthened by Ordered Phase Precipitation for Gas Turbine Applications," Advanced Materials Research Online, no. 278, pp. 569-574, 2011.

[27] E. Rudy and H. Nowotny, "A σ-phase in the chromium-molybdenum-silicon system," Chemical Monthly, vol. 105, pp. 156-168, 1974.

[28] L. Pandelaers and R. Schmid-Fetzer, Landolt-Börnstein: Ternary Alloy Systems, Subvolume E, Refractory Metal Systems, Springer, 2010, pp. 182-191.

[29] H. Blumenauer and G. Pusch, Technical fracture mechanics, Leipzig: Deutscher Verlag Für Grundstoffindustrie, 1993, p. 101.

[30] T. Cruse and J. W. Newkirk, "Evaluation of methods to produce tough Cr3Si based composites," Materials Science and Engineering, vol. A239, no. 240, p. 410–418, 1997.

[31] F. Hinrichs, G. Winkens, L. K. Kramer, G. Falcao, E. M. Hahn, D. Schliephake, M. K. Eusterholz, S. Sen, M. C. Galetz, H. Inui, A. Kauffmann, M. Heilmaier, “A ductile chromium–molybdenum alloy resistant to high-temperature oxidation”, Nature, 646, p. 331–337, 2025.

[32] A. Iturbe, E. Giraud, E. Hormaetxe, A. Garay, G. Germain, K. Ostolaza and P. J. Arrazola, "Mechanical characterization and modelling of Inconel 718 material behavior for machining process assessment," Materials Science & Engineering A, vol. A 682, pp. 441-453, 2017.

[33] M. Kaufman, "Properties of cast MAR-M-247 for Turbine Blisk Applications," in Proceedings of the Fifth International Symposium on Superalloys, Metallurgical Society of AIME, Warrendale, PA, 1984.

[34] Y. Ro, Y. Koizumi, S. Nakazawa and T. Kobayashi, "Development of Cr-base alloys and their compressive properties," Scripta Materialia, vol. 46, pp. 331-335, 2002.

4 Synopsis

4.1 The role of Mo in the A2 (Cr) + A15 (Cr_3Si) alloy concept

The effect of Mo on the microstructure in Cr-xMo-8 at.%Si alloys

Increasing the Mo content in Cr-xMo-8 at.%Si alloys had a pronounced and systematic effect on the grain size, phase distribution, phase stability and elemental distribution. Mo is soluble in the A2 solid solution matrix and, due to its larger atomic radius, caused a continuous increase in the lattice parameter of the A2 phase with increasing Mo content. At low Mo levels (≤10 at.%), the as-cast microstructure of the arc-melted material remained largely homogeneous and consisted predominantly of the A2 phase, with only minor A15-$(Cr,Mo)_3Si$ formation. At higher Mo contents, segregation within the A2 phase became evident. Two distinct A2 solid solutions were observed: a Mo-rich and Si-poor phase and a Mo-poor and Si-rich phase. For 20 at.% Mo some A15 intermetallic phase formed initially upon casting. With further Mo addition (25-40 at.%), strong dendritic solidification was observed in the as-cast condition, and the formation of the σ phase occurred instead of the A15 phase, indicating that increased Mo contents stabilize the metastable σ phase, which is in line with literature [83]. The described findings about the σ phase ($Cr_{0.39-0.57}Mo_{0.47-0.29}Si_{0.14}$) of Rudy et al. [86] were implemented into the Cr-Mo-Si phase diagram published in ref. [83] shown in Figure 13. From this data it is clear that at 1300 °C the σ phase should be stable at high Mo contents. The phase diagram however suggests 35 at.% Mo as boundary to stabilize the σ phase. It's occurrence in as-cast condition at already 25 at.% Mo might indicate a stability also for lower Mo contents at high temperatures.

Annealing at 1200 °C and 1350 °C significantly altered the microstructure. Both temperatures were able to homogenize the segregations from the as-cast state, leading to a chemically homogeneous A2 matrix phase. Heat treatment at 1200 °C led to the formation of the A15 phase, partly very localized to where the former Si-rich areas existed and thus some A15 phase was clustered, which was successfully improved by a two-step annealing. Annealing at 1200 °C resulted in

the eutectoid decomposition of the previously observed σ phase into A2 and A15, consistent with refs [86, 34]. Annealing at 1350 °C produced overall slightly lower amounts of the A15 phase due to increased Si solubility in A2 at higher temperatures. The σ phase partially remained stable in the alloy containing 40 at.% Mo during the 1350 °C anneal. Higher annealing temperatures (1450 °C) resulted in further reduction of the A15 phase fraction again due to increased Si solubility in A2 at higher temperatures. Also, at 1450 °C the σ phase was stabilized for Mo contents down to 25 at.%, showing that for increasing Mo content the σ phase stability range shifts to lower temperatures.

Mo partitioned preferentially to the A2 phase rather than to the A15 phase, and this partitioning increased with increasing Mo content and decreasing annealing temperature. This result deviates from the equal partitioning behavior observed in [79] for low amounts of Mo (2 at.%). Increasing the Mo content reduced the solubility of Si in both the A2 and A15 phases, which led to an increasing volume fraction of the A15 phase until formation was limited by the total fixed Si content. Grain boundary precipitation of the A15 phase is observed to be reduced with increasing Mo content and higher annealing temperature.

Also, increasing Mo content led to pronounced grain refinement, reducing the average grain size by approximately one order of magnitude, from several hundred micrometers in the reference alloy Cr-8 at.%Si to tens of micrometers at higher Mo contents. This grain-refining effect is attributed to increased chemical inhomogeneity in the as-cast state, enhancing defect density, and the presence of intermetallic phases acting as additional nucleation sites during annealing. The decomposition of σ phase further contributed to grain refinement and to a finer, more homogeneous distribution of the A15 phase. At Mo contents of 20 at.% and above, changes in grain morphology from predominantly equiaxed to more columnar grains were observed.

Overall, careful control of Mo concentration and annealing conditions is required to suppress σ phase formation and to achieve a uniform and thermodynamically stable A2 + A15 microstructure suitable for further property optimization.

Figure 17 shows ternary phase diagram sections of the Cr-Mo-Si system, including reference data at 1300 °C from literature [83] in red lines. Also, the phases observed in this work for the global alloy compositions were added in the

form of large dots and suggested phase boundaries as lines, coming from the compositional data of the single phases for as-cast and annealed conditions at 1200, 1350 and 1450 °C. From the data, it is clear that the stability of the σ phase field is shifting towards the Cr-rich side with increasing temperature. Also, it is visible for all temperatures that Si solubility in A2 rather linearly decreases with increasing Mo content, contradicting [83], where between 10 and 80 at.% of Mo a constant Si solubility in A2 was depicted at 1300 °C. The strongest deviation between the findings in this work and the literature data is visible in the lower

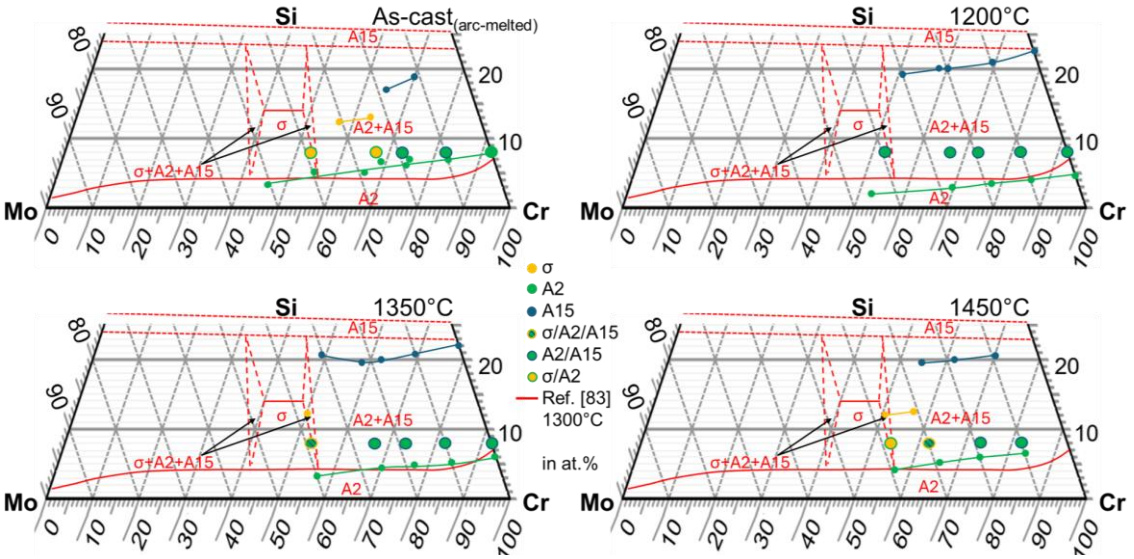

Figure 17: Ternary phase diagram section of the Cr-Mo-Si system including data at 1300 °C after [83] in red lines as reference and adding the observed phases as big dots and suggested phase boundaries from phase compositions of this work as lines for as-cast and annealed condition at 1200, 1350 and 1450 °C.

phase boundary of the A15 phase. In the reference data, the boundary is depicted as a dashed line, indicating uncertainty in the exact position. The compositional data of Cr-xMo-8 at.%Si alloys studied in this work give more precise information on the positioning of the single-phase field of the A15 phase and its dependence on Mo content. This A15 boundary clearly extends to lower Cr, higher Mo and lower Si contents than what has been previously depicted.

The temperature dependence of the Si solubility is less dominant in the A15 phase compared to the A2 phase. Similar to the A2 phase, a linearly decreasing Si solubility in the A15 phase is observed with increasing Mo content. This effect is not accounted for in the reference data [83], even implying a slight increase in Si solubility.

In Figure 18 a), experimentally determined Si solubilities in A2, depending on Mo content, are linearly extrapolated to the point where the full 8 at.% Si of the alloy are in theory soluble in A2. This data and data from Figure 17 are used in Figure 18 b), where an estimation of phase field stability in the Cr-xMo-8 at.%Si alloy system is depicted depending on Mo content and temperature. The overview provides a more intuitive understanding of the Cr-xMo-8 at.%Si alloy system and the stability regime of the σ phase depending on Mo content and temperature. Although avoidance of the σ phase is crucial for application purposes, limited initial amounts did not lead to issues during processing. During eutectoid

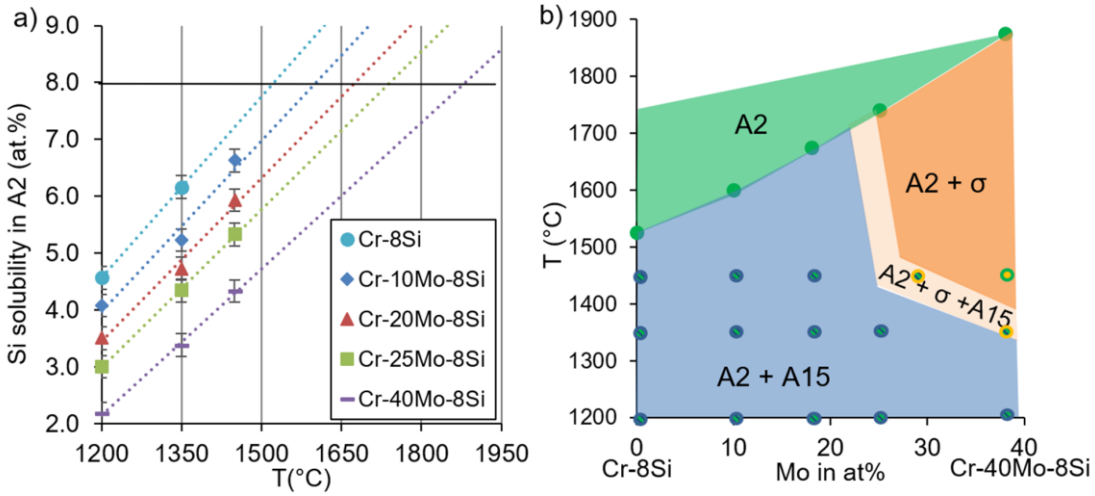

Figure 18: a) Si solubilities in the A2 matrix from this work vs. temperature, b) Estimated phase field stabilities in the Cr-xMo-8 at.%Si alloys depending on Mo content and temperature.

decomposition no cracks or visible defects were introduced, on the contrary, the decomposition of pre-existing fine σ phase from the as-cast state even led to a more homogenous distribution of A15 phase after annealing. With arc-melting, only limited success in optimizing the microstructure and phase distribution can be achieved, due to the very high temperatures that are necessary to reach full solubility of Si. However, the two step heat treatments developed in this work, showed a beneficial effect on A15 distribution.

The effect of Mo on the oxidation and nitridation in Cr-xMo-8 at.%Si alloys at 1200 °C

Oxidation experiments at 1200 °C in air demonstrated that increased Mo additions to Cr-xMo-8 at.%Si alloys improved oxide scale adhesion and strongly

influenced the corrosion mechanisms. Increasing Mo content reduced oxide spallation, with alloys containing ≥25 at.% Mo showing adherent chromia scales during isothermal exposure at 1200 °C. Thus, the addition of Mo alters the chromia scale growth mechanism, leading to lower scale stresses, which could be due to doping effects or the creation of free volume by Mo volatilization. Further studies are necessary to fully clarify this effect. All Mo-containing alloys showed fully inhibited nitridation of the A2 solid solution after 50 and 100 h of exposure, unlike the Mo-free reference alloy. Internal oxidation of the A15 phase occurred at low Mo contents but decreased with increasing Mo. Cr-25Mo-8Si exhibited particularly favorable oxidation behavior, forming a continuous SiO_2 subscale beneath the Cr_2O_3 layer that suppressed further internal oxidation. Not only was the amount of Mo decisive on the formation of a continuous SiO_2 subscale, but also the annealing prior to exposure.

Figure 19 shows the schematic representation of the oxidation behavior at 1200 °C of the Cr-25Mo-8 at.%Si alloys heat treated at a) 1350 °C and b) 1200 °C. The described SiO_2 subscale forms preferably at a Mo content of

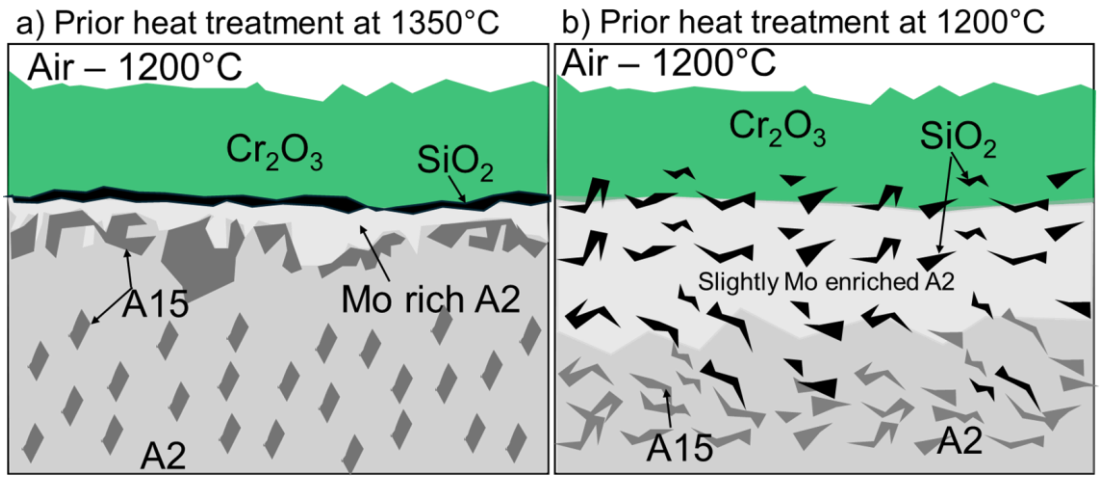

Figure 19: Schematic representation of oxidation behavior of Cr-25Mo-8 at%Si after exposure at 1200°C in air for alloys heat treated at a) 1350 °C and b) 1200 °C.

25 at.% and prior annealing at 1350 °C before oxidation in air at 1200 °C. Several factors affect SiO_2 formation. The more homogeneously distributed A15 phase and the Si-supersaturated A2 phase after the 1350 °C anneal enabled faster and more continuous SiO_2 formation initially. Mo does not participate in oxide scale formation due to MoO_3 volatilization and lower thermodynamic stability and thus

a Mo-enriched A2 zone forms beneath chromia. The compositional studies revealed that Si solubility in A2 is decreased with increasing Mo content, so even more Si is available to form SiO_2 at the oxide scale/alloy interface and A15 at the diffusion zone/alloy interface, as visible in Figure 19 a). When the same alloy is annealed at 1200 °C prior to oxidation, as visible in Figure 19 b), the A15 phase is less homogenously distributed, and the A2 phase is not supersaturated. In this case, the SiO_2 is mainly formed from the A15 phase, leading to discontinuous subscale formation. This opens up a path for further oxygen inward diffusion and leads to internal oxidation of the A15 phase to SiO_2. The remaining A2 beneath chromia is only slightly enriched in Mo, but is thicker overall for Figure 19 b). Also, the formation of A15 beneath the Mo-enriched zone is not observed in this case and thus it is likely also depending on the initial formation of continuous SiO_2. In both cases the formation of Kirkendall pores was not observed, which usually happens, when there is a large imbalance in intrinsic diffusion fluxes, causing a net vacancy flux and the accumulation of vacancies into pores [107]. Thus, the excess vacancies forming upon Cr outward diffusion are likely able to rapidly annihilate at sinks like grain boundaries, phase interfaces, and dislocations and are removed before they accumulate to pores. Also, the Mo enrichment beneath chromia increases the lattice parameter, thus distorting the lattice. An expanded lattice can accommodate vacancies elastically, lowering the need for vacancy condensation into voids [107].

Independent of the SiO_2 subscale formation, none of the Mo-containing alloys investigated in this work showed nitridation of the A2 matrix. From the literature, it was known that 32 at.% Mo added to a Cr-Si alloy inhibited nitridation of the A2 matrix fully [35], while for additions of 2 at.% Mo, some nitridation of A2 was still observed [32]. From the results of this work, it is now clear that Mo contents ≥10 at.% Mo inherently protect the A2 matrix from nitridation during exposure at 1200 °C in air. In Figure 20 the N solubility vs. temperature is depicted for Mo and Cr after [22]. This data explains the observed nitridation resistance, showing that Mo has an order of magnitude lower solubility for N at 1200 °C (ca. 0.02 vs. 0.2 at.%). The incorporation of Mo into A2 thus seems to reduce the solubility of N and prevent the formation of Cr_2N.

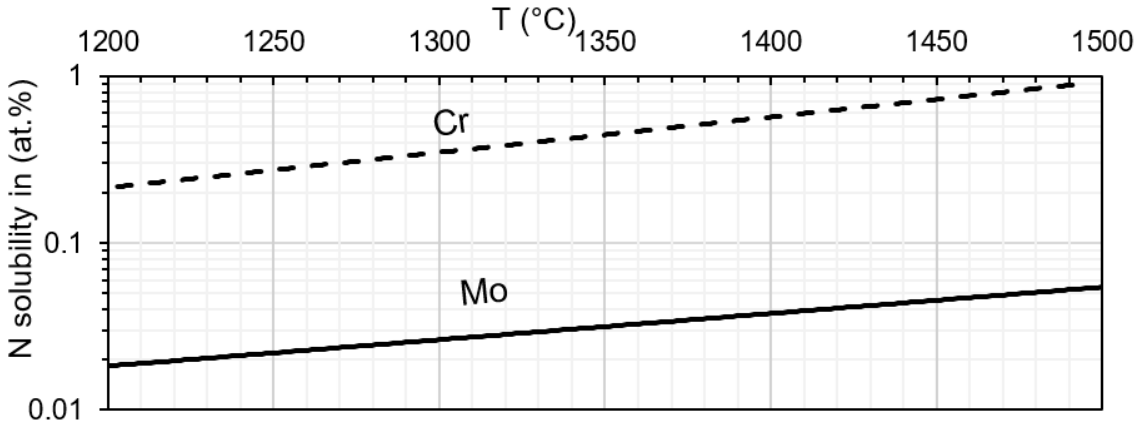

Figure 20: N solubility vs. temperature data for Mo and Cr after [22] (with kind permission of Springer Nature).

Thermogravimetric analysis showed that Mo additions up to 25 at.% reduced both the parabolic oxide growth rate and volatilization rate compared to Cr-8Si. However, the 10 at.% Mo alloy showed the lowest k_v, while it was slightly higher for 20 and 25 at.% of Mo, suggesting some influence of Mo volatilization. The Cr-25Mo-8Si alloy displayed the lowest mass gain and the most stable oxidation behavior, whereas Cr-40Mo-8Si suffered from dominant Mo volatilization due to MoO_3 formation. The initial parabolic growth rate k_p of the reference material Cr-8Si was determined to be $1.4 \cdot 10^{-10}$ g²cm^{-4}s^{-1} at 1200 °C and was reduced to $6.9 \cdot 10^{-11}$ g²cm^{-4}s^{-1} for the alloy containing 25 at.% Mo. This shifts the oxidation kinetics of the alloy more into the regime of alumina and silica formers when compared to Figure 1 b). Overall, Mo additions up to 25 at.% were concluded to beneficially modify microstructure, suppress nitridation, improve oxide adhesion, and stabilize oxidation behavior at 1200 °C, making Cr-25Mo-8Si a particularly promising composition for high-temperature applications.

Influence of Mo on the mechanical properties of Cr-xMo-8 at.%Si alloys

The addition of Mo had a distinct influence on the mechanical properties of Cr-xMo-8 at.%Si alloys, affecting hardness, strength, fracture toughness, deformation behavior and the ductile-to-brittle transition temperature (DBTT). Overall, increasing Mo content significantly enhanced strength and hardness over a wide temperature range, but this improvement was accompanied by reduced low-temperature toughness and a shift of the DBTT to higher temperatures, estimated from the strain at maximum stress in compression tests.

The mechanical response was governed by a combination of solid solution strengthening of the Cr-rich matrix (A2 phase), changes in the amount and characteristics of the intermetallic A15 phase $(Cr,Mo)_3Si$, and Mo-induced grain refinement.

Room-temperature hardness increased linearly with increasing Mo content. The dominant hardening mechanism was solid solution strengthening of the Cr-based A2 matrix by Mo, while precipitation hardening from the A15 phase played a secondary role. Comparisons between single-phase and two-phase alloys showed that Mo solid solution strengthening contributed far more to room temperature hardness than increasing the volume fraction of the intermetallic phase. Although the A15 phase is intrinsically much harder than the matrix, its contribution to bulk hardness was limited, and variations in A15 size and distribution caused by different annealing treatments had little to no effect on overall hardness at room-temperature. To demonstrate the impact and effectiveness of the A15 phase in the system, high-temperature creep tests must be conducted in the future. With increasing Mo content, the hardness of the A2 phase increased, whereas the hardness of the A15 phase decreased, which could relate to the reduced Si content and possible additional defect formation. During hardness testing, finer A15 precipitates were found to be less susceptible to cracking. This indicates that Mo indirectly enhances the local fracture toughness of the intermetallic phase, for example by promoting the formation of a eutectoid microstructure arising from the decomposition of the initial σ phase into fine lamellae of A15 and A2 in alloys with high Mo contents.

As stated previously, Mo additions also led to a pronounced grain-refining effect. These microstructural changes played a critical role in both fracture behavior and high-temperature strength.

Fracture toughness at room temperature showed a non-monotonic dependence on Mo content. While the Mo-free, two-phase alloy, Cr-8Si, and the Mo-rich, single-phase alloy, Cr-26Mo-3Si, exhibited relatively high apparent toughness (with no crack formation in high load Vickers indentation tests; implying fracture toughness ≥10 $MPa \cdot m^{0.5}$), the introduction of Mo into the two-phase Cr-xMo-8 at.%Si alloys initially reduced fracture toughness to values as low as ~4 $MPa \cdot m^{0.5}$. At the highest Mo content (40 at.%), fracture toughness increased

again up to 10 MPa·m$^{0.5}$. This behavior reflected competing effects. Intermediate Mo contents initially decrease the fracture toughness of the alloy due to a higher amount of A15 and partly coarse intermetallic phase. Even higher amounts of Mo lead to grain refinement, a decreased hardness of A15, together with the formation of local fine A15 phase lamellas. Nevertheless, the fracture toughness of the two-phase Mo-containing alloys remained below the level required for many structural applications (≥15 MPa·m$^{0.5}$), indicating that fracture toughness still needs to be addressed in further research. Microstructural optimization via powder metallurgy could promote a finer, more uniformly distributed A15 phase and enable improved grain size control, potentially enhancing fracture toughness. Furthermore, the decomposition of fine σ phase present in the as-cast condition results in a homogeneous and finely lamellar A15 structure after annealing. This mechanism could be deliberately exploited, for example by applying a Cr-25Mo-8 at.% Si composition in a powder metallurgical processing route.

Compression testing from room temperature up to 1000 °C demonstrated that Mo substantially increased strength across the entire temperature range. Yield stress and specific strength rose consistently with Mo content, with Cr-25Mo-8 at.%Si exhibiting the highest values. Due to the low oxidation resistance of Cr-40Mo-8 at.%Si, this alloy was excluded from compression testing. The maximum compressive specific strength of Cr-25Mo-8 at.%Si (~170 N·m·g^{-1}) was comparable to that of the Ni-based superalloys IN718 up to about 700 °C and remained superior at 1000 °C with ~100 N·m·g^{-1} compared to MAR-M-247 (~40 N·m·g^{-1}), highlighting the excellent high-temperature strength potential of the Cr-25Mo-8 at.%Si alloy. The A15 phase contributed to elevating the overall strength level (and will be especially necessary in terms of creep resistance), while Mo solid solution strengthening of the A2 matrix was the primary factor controlling the strength increase.

Despite the strength benefits, Mo additions shifted the DBTT to higher temperatures. Cr-8Si showed a DBTT between roughly 500 and 700 °C, whereas alloys with 10 at.% Mo transitioned between 700 and 900 °C, and alloys with 20-25 at.% Mo remained largely brittle or show mixed fracture up to 900 °C. This shift confirmed that strong solid solution strengthening by Mo, while beneficial for high-temperature strength, reduced the low-temperature ductility. Compression

tests nevertheless revealed limited, but measurable, compressive plasticity even at room temperature for all compositions, although the Mo-rich alloys failed in a clearly brittle manner. Likely twinning contributes to room-temperature plasticity as described in [35]. Especially at low temperatures, twinning stress in Cr-Mo-Si alloys can become lower or similar to dislocation slip stress [35], thus both processes can be active and result in some plasticity. This should be further investigated for the alloys of this work in future studies.

Deformation and fracture mechanisms evolved with temperature and Mo content. At lower temperatures, cracking tended to initiate in the brittle A15 phase or along A2-A15 interfaces, while the A2 matrix provided limited crack-arrest capability. At higher temperatures, the A2 matrix became more deformable, and the intermetallic phase contributed to load bearing and crack deflection. With increasing Mo content, higher matrix strength suppressed plastic deformation, promoting earlier fracture and brittle failure.

In summary, Mo is a highly effective alloying element for improving the hardness and high-temperature strength of Cr-xMo-8 at.%Si alloys, primarily through solid solution strengthening and microstructural refinement. These benefits came at the cost of increased brittleness and a higher DBTT. The results demonstrated that an optimal Mo content, around 20-25 at.%, provided a very high specific strength for high-temperature applications, while further improvements in fracture toughness would require additional microstructural optimization, particularly grain refinement and control of the A15 phase size and distribution.

Alternative production methods like powder metallurgy may be utilized in the future to see how much the fracture toughness could benefit from an optimized microstructure. Further alloying optimization is another way to make use of the already very attractive property portfolio of Cr-25Mo-8 at.%Si, as shown for the Cr-Mo-Si-Ni-Al system.

4.2 Combining the Cr-Mo-Si system with an A2 (Cr) + B2 (NiAl) concept

The Cr-Mo-Si-Ni-Al alloy system was systematically investigated to assess whether the established strengthening mechanisms of the Cr-Mo-Si system could be successfully combined with low-misfit NiAl-B2 precipitates. The results demonstrated that the incorporation of NiAl precipitates into a Mo- and Si-strengthened Cr-A2 matrix fundamentally altered phase stability and mechanical performance, particularly with respect to fracture toughness and high-temperature strength.

Compared to the ternary Cr-Mo-Si parent alloy, the introduction of Ni and Al promoted the formation of the σ phase at lower Mo contents. This behavior indicated that Ni strongly stabilized the σ phase, which was confirmed by EPMA-WDS measurements showing substantial Ni solubility within the σ phase. Reducing the Mo content effectively decreased the σ-phase fraction, consistent with trends previously observed in Cr-Mo-Si alloys. Additionally lowering the Ni/Al ratio from 1.0 to 0.67 significantly reduced σ-phase formation, confirming that Ni acted as the dominant σ phase promoter, while Al primarily participated in forming the B2-NiAl phase.

A two-step annealing treatment with a homogenization step at 1400 °C dissolved intergranular NiAl from the as-cast state into the A2 matrix, while subsequent aging at 1200 °C resulted in controlled precipitation of the B2 phase. In Mo-rich alloys, σ-phase decomposition was incomplete, demonstrating that Ni and Al additions stabilized the σ phase against eutectoid decomposition into A2 and A15; thus the σ phase is not only stabilized at lower Mo contents but also lower temperatures. Alloys with Mo content of ≤10 at.% showed complete σ-phase elimination after annealing. At high Si contents (8 at.%), the aged microstructures contained A15 precipitates in addition to B2, with B2 preferentially decorating A2-A15 interfaces. These alloys exhibited heterogeneous precipitate distributions and retained brittle intermetallic phases. Reducing the Si content to 3 at.% resulted in the overall composition of Cr-10Mo-3Si-5Ni-5 at.%Al and successfully suppressed A15 formation and enabled the development of a solely A2+B2 microstructure.

This optimized composition exhibited a homogeneous A2 matrix strengthened by finely distributed B2 precipitates with an average size of approximately 600 nm. These precipitates remained stable after prolonged aging at 1200 °C, indicating excellent thermal stability.

Synchrotron XRD and Rietveld refinement confirmed the presence of A2 and B2 phases in the optimized alloy, with lattice parameters of 2.9209 Å for A2 and 2.8901 Å for B2. The calculated lattice misfit of approximately −1.05% was larger than that reported for Mo-free Cr-Ni-Al alloys [96], confirming lattice expansion due to Mo alloying. Despite the increased misfit, the B2 precipitates maintained a stable morphology and EBSD revealed a consistent orientation relationship between the A2 matrix and B2 precipitates.

The measured B2 volume fraction of approximately 6% was sufficient to provide effective precipitation strengthening without degrading microstructural stability or toughness.

Room-temperature hardness measurements showed that B2 precipitation provided strengthening comparable to that achieved with significantly larger A15 phase fractions. The A2+B2 alloy Cr-10Mo-3Si-5Ni-5 at.%Al exhibited a hardness of approximately 5.6 GPa, similar to Cr-10Mo-8Si with A15 strengthening. Cr-Mo-Si-Ni-Al alloys containing multiple intermetallic phases (B2, A15 and σ phases) showed higher hardness but suffered from pronounced brittleness.

High-load Vickers indentation tests revealed a critical difference in fracture behavior. Alloys containing A15 and σ phases exhibited extensive crack formation, whereas the A2 + B2 alloy showed no cracking under HV30 loading. This result clearly demonstrated that B2 precipitates did not degrade fracture toughness, in contrast to the more brittle A15 and σ phases. The absence of indentation cracking indicated a substantial improvement in low-temperature fracture resistance when A15 was replaced by B2.

Compression tests demonstrated that the Cr-10Mo-3Si-5Ni-5Al A2 + B2 system achieved specific strength comparable to the Cr-10Mo-8Si A2 + A15 system at room temperature and intermediate temperatures, namely 95 $N \cdot m \cdot g^{-1}$. Importantly, the A2 + B2 alloy retained its strength up to the highest tested temperature of 1000 °C, whereas the A2 + A15 system exhibited a more

pronounced reduction in strength down to 74 $N \cdot m \cdot g^{-1}$. The superior high-temperature performance of the A2 + B2 alloy was attributed to the fine, low-misfit B2 precipitates, which effectively impeded dislocation motion even at high temperatures. In contrast, coarse and widely spaced A15 precipitates were less effective as obstacles to plastic deformation. However, the A2 + B2 alloy showed lower fracture strain in compressive testing compared to A2 + A15-containing alloys at intermediate temperatures.

The results demonstrated that combining the Cr-Mo-Si system with the A2 + B2 concept was advantageous when compositional constraints (phase formation) were carefully managed. Mo and Si provided solid-solution strengthening and are known to enhance oxidation and nitridation resistance, while NiAl-B2 precipitates supplied effective precipitation strengthening without compromising fracture toughness. The A15 phase, which limited the applicability of Cr-Mo-Si alloys at lower temperatures, was successfully replaced by low lattice mismatch B2 precipitates through alloy optimization.

Comparing the solubility of Ni+Al in Cr and Cr-10 at.% Fe as predicted in [96] to Cr-10Mo-3 at.% Si alloy in this work (Figure 21), shows that the B2-NiAl phase has lower solubility in Mo strengthened Cr alloys. Along with the high solubility at 1400 °C that provides a suitable heat treatment window, higher volume fraction

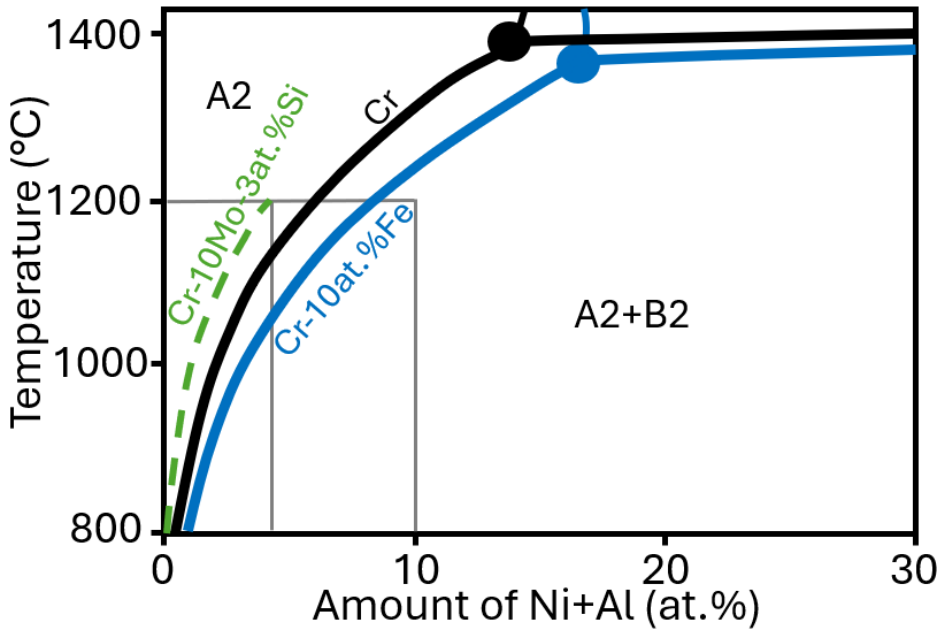

Figure 21: Ni+Al solubility in Cr and Cr-10at.% Fe alloy after [96] and for Cr-10Mo-3at.% Si alloy from this work.

of precipitates are possible and higher temperature stability for the strengthening particles e.g. for applications at 1200°C.

Overall, the A2 + B2 architecture in Cr-Mo-Si alloys delivered a unique combination of high-temperature strength up to 1000 °C and possibly beyond (indicated by Figure 21), improved low-temperature fracture toughness by retaining the matrix plasticity, and microstructural stability.

These results established the Cr-Mo-Si-Ni-Al system as a promising system for the development of next-generation Cr-based BCC superalloys. Future endeavors in this alloy system need to focus on investigation of the oxidation and nitridation resistance, which is inherently already very good in the A2 + A15 parent alloy.

5 Conclusions and Prospect

The overarching objective of this work was to advance precipitation-strengthened Cr-based alloys for high-temperature structural applications by addressing the key challenges historically associated with this material class: Insufficient oxidation and nitridation resistance, low-temperature fracture toughness and high-temperature strength.

Through a systematic investigation of the influence of Mo content in the Cr-xMo-8 at.%Si A2 + A15 alloy system and the subsequent development of an alternative A2 + B2 precipitation concept, significant progress toward a more balanced property profile has been achieved.

Mo was identified as a central alloying element influencing oxidation and nitridation resistance and mechanical performance. Increasing Mo content in Cr-xMo-8 at.%Si led to pronounced solid-solution strengthening of the A2 matrix, strong grain refinement and enhanced high-temperature strength.

The oxidation behavior of Cr-xMo-8 at.%Si alloys at 1200 °C in air was improved by addition of 10-25 at.% Mo, while at 40 at.% MoO_3 formation became dominant. Mo increased the chromia scale adhesion, fully suppressed nitridation of the A2 matrix (for Mo all contents ≥10 at.%) and - at optimized compositions and heat treatment - enabled the formation of a continuous, protective SiO_2 subscale. This effect was most pronounced for alloys containing 25 at.% Mo, which exhibited the most favorable oxidation kinetics by forming a duplex oxide scale with outer chromia and inner silica formation, limiting the internal oxidation of the A15 phase.

Microstructural investigations revealed that careful control of Mo content and heat-treatment conditions is essential to suppress the formation of the σ phase and to achieve a homogeneous and thermodynamically stable A2 + A15 microstructure. The results further refined existing ternary phase diagram data for the Cr-Mo-Si system, particularly regarding Si solubility limits and σ phase stability, thereby providing valuable guidance for future alloy design.

Mechanically, Mo additions substantially increased hardness and strength, resulting in specific strength partly exceeding those of established Ni-based superalloys at 1000 °C (100 $N \cdot m \cdot g^{-1}$ for Cr-25Mo-8Si with density of 7.62 $g \cdot cm^{-3}$). However, these benefits were accompanied by a reduction in

fracture toughness and a shift of the ductile-to-brittle transition temperature to higher temperatures. Despite partial mitigation via microstructural refinement, room-temperature fracture toughness remained the principal limitation of the A2 + A15 alloy concept.

To overcome this limitation, an alternative precipitation strategy based on low-misfit B2 (NiAl) precipitates was developed and Cr-Mo-Si-Ni-Al alloys were studied. Ni was shown to shift the σ phase field stability to lower Mo contents and lower temperatures. By carefully balancing Mo, Si, and Ni contents, a stable A2 + B2 microstructure was achieved for the composition Cr-10Mo-3Si-5Ni-5 at.%Al without the formation of A15 or brittle σ phase. This alloy concept retained high-temperature strength up to 1000 °C (95 $N \cdot m \cdot g^{-1}$ for Cr-10Mo-3Si-5Ni-5Al with a density of 7.25 gcm^{-3}), while exhibiting a markedly improved fracture resistance at room temperature, compared to the A2 + A15 parent system. The results clearly demonstrated that B2 precipitation can effectively replace A15 strengthening in Cr-based alloys, enabling a more favorable combination of strength and toughness.

In summary, this work demonstrates that Cr-based alloys can achieve a property profile that is highly attractive for high-temperature applications beyond the capability of current Ni-based superalloys by alloying and microstructural optimization. Both the A2 + A15 and A2 + B2 concepts provide viable pathways, with the latter offering a particularly promising route toward overcoming the long-standing fracture toughness limitations of Cr-based materials.

While this work establishes a solid foundation for the development of advanced Cr-based high-temperature alloys, several important research directions remain to be addressed before practical application can be realized.

Firstly, further improvements in fracture toughness are essential, particularly for the A2 + A15 system. Alternative production routes such as powder metallurgical processing offer significant potential to optimize grain size and precipitate size and distributions, beyond what is achievable by arc melting and subsequent heat treatment. Such approaches may enable an increased fracture toughness, while preserving high-temperature strength. Also, larger specimen sizes can be manufactured with an alternative production route, so that tensile testing as well

as Charpy impact testing become feasible, providing a more accurate estimate of strength and toughness.

Secondly, long-term creep behavior and fatigue resistance must be systematically investigated for both A2 + A15 and A2 + B2 alloys. While the present work demonstrates excellent short-term high-temperature strength, the suitability of these materials for turbine-relevant service conditions depends critically on their time-dependent deformation behavior and damage tolerance under cyclic loading.

Thirdly, the oxidation and nitridation behavior of the A2 + B2 Cr-Mo-Si-Ni-Al alloys requires further studies. Although the parent Cr-Mo-Si system exhibits inherently very good environmental resistance, the influence of Ni and Al additions on oxide scale formation, nitridation, and long-term stability must be clarified to fully assess the applicability of the A2 + B2 concept in high-temperature environments.

Finally, further alloy optimization to vary the precipitate volume fraction and lattice misfit in Cr-based A2 + B2 superalloys is of interest. For this purpose, alternative B2-forming systems could be explored. Minor alloying additions that can benefit the matrix phase ductility may open additional pathways toward application-specific alloy solutions.

Overall, this work highlights the considerable, yet still largely unexplored potential of Cr-based alloys as next-generation high-temperature structural materials. With continued research focused on toughness enhancement and long-term mechanical performance, Cr-based A2 + A15 and A2 + B2 alloys could become viable candidates for future aerospace propulsion systems and advanced energy conversion technologies.

References

[1] E. Newton Foote, "Circumstances affecting the heat of the Sun's rays," *American Journal of Science and Arts,* vol. 2nd Series, no. v. XXII/no. LXVI, pp. 382-383, 1856.

[2] H. R. Brannon Jr, A. C. Daughtry, D. Perry, W. W. Whitaker and M. Williams, "Radiocarbon evidence on the dilution of atmospheric and oceanic carbon by carbon from fossil fuels," *Eos, Transactions American Geophysical Union,* vol. 38, no. 5, pp. 643-650, 1957.

[3] E. Robinson and R. C. Robbins, "Sources, abundance, and fate of gaseous atmospheric pollutants. Final report and supplement.," Stanford Research Institute, Menlo Park, CA., 1968.

[4] S. Hauser, T. Vadén, M. Nagatsu, F. Obeng-Odoom and J. Eronen, "Early knowledge but delays in climate actions: An ecocide case against both transnational oil corporations and national governments," *Environmental Science & Policy,* vol. 161, p. 103880, 2025.

[5] "Our common future "Brundtland report"," The World Commission on Environment and Development, 1987.

[6] "European Commission, European Climate Law," 2025. [Online]. Available: https://climate.ec.europa.eu/eu-action/european-climate-law_en. [Accessed 16 09 2025].

[7] "Klimaschutz Portal," Bundesverband der Deutschen Luftverkehrswirtschaft (BDL), [Online]. Available: https://www.bdl.aero/wp-content/uploads/2024/07/2020-klimaschutzreport-bdl.pdf. [Accessed 16 09 2025].

[8] M. C. Galetz, E. M. H. White, M. Kerbstadt, C. Schlereth, X. Montero and D. Benitez, "Material Challenges and Alloy Selection for Particle/s-CO2 Heat Exchangers in Concentrated Solar Power Systems," *Advanced Engineering Materials,* vol. 27, p. 2402060, 2025.

[9] R. Altobelli Antunes, L. d. Oliveira and M. C., "Corrosion in biomass combustion: A materials selection analysis and its nteraction with corrosion mechanisms and mitigation strategies," *Corrosion Science,* vol. 76, pp. 6-26, 2013.

[10] J. H. Perepezko, "The Hotter the Engine, the Better," *Science,* vol. 326, pp. 1068-1069, 2009.

[11] J. R. Davis, "Metallurgy, Processing and Properties of Superalloys," in *Heat-Resistant Materials (ASM Speciality Handbook)*, ASM International, 1997, pp. 221-253.

[12] D. B. Miracle, M.-H. Tsai, O. N. Senkov, V. Soni and R. Banerjee, "Refractory high entropy superalloys (RSAs)," *Scripta Materialia,* vol. 187, pp. 445-452, 2020.

[13] B. Duana, Y. Yanga, S. Hea, Q. Fenga, L. Maoa, X. Zhanga and L. Jiaoa, "History and development of γ-TiAl alloys and the effect of alloying elements on their phase transformations," *Journal of Alloys and Compounds,* vol. 909, p. 164811, 2022.

[14] M. Galetz, Ulrich, A.S., C. Oskay, D. Fähsing, N. Laska, U. Schulz and M. Schütze, "Oxidation-induced microstructural changes of the TiAl TNM-B1 alloy after exposure at 900 °C in air," *Intermetallics 123 (2020) 106830,* vol. 123, p. 106830, 2020.

[15] G. Karadimas and K. Salonitis, "Ceramic Matrix Composites for Aero Engine Applications—A Review," *Applied Sciences,* vol. 13, p. 3017, 2023.

[16] T. G. Nieh and J. Wadsworth, "Recent advances and developments in refractory alloys," *Materials Research Society,* vol. 322, pp. 315-327, 1993.

[17] J. Yang, G. Zhuo, K. Jiang, X. Zhu and L. Su, "The Oxidation Resistance of Nb-Si-Based Alloys at Intermediate and High Temperatures," *Materials,* vol. 13, 2020.

[18] P. Tsakiropoulos, "Alloys for application at ultra-high temperatures: Nb-silicide in situ composites Challenges, breakthroughs and opportunities," *Progress in Materials Science,* vol. 123, p. 100714, 2022.

[19] R. Su, L. L. and J. H. Perepezko, "Alloy Designs for High Temperature Mo-Base Systems," *International Journal of Refractory Metals and Hard Materials,* vol. 113, p. 106199, 2023.

[20] J. A. Lemberg and R. O. Ritchie, "Mo-Si-B Alloys for Ultrahigh-Temperature Structural Applications," *Advanced Materials,* vol. 24, pp. 3445-3480, 2012.

[21] A. Lange, "Dissertation: Magnetrongesputterte Oxidationsschutzschichten für Mo-Si-B-Legierungen," 2014.

[22] W. D. Klopp, "Recent Developments in Chromium and Chromium Alloys," *Journal of Metals,* vol. 21, pp. 24-32, 1969.

[23] "Ductile chromium and its alloys," in *Proceedings of a conference under the auspices of Office of Ordnance Research - 1955 Metal Congress and Exposition of the American Society for Metals*, Cleveland, 1957.

[24] J. R. Davis, "Directionally Solidified and Single-Crystal Superalloys," in *ASM Speciality Handbook Heat-Resistant Materials*, ASM International, 1997, pp. 255-271.

[25] A. S. Dorcheh and M. C. Galetz, "Challenges in Developing Oxidation-Resistant Chromium-Based Alloys for Applications Above 900°C," *The Journal of Minerals, Metals & Materials Society,* vol. 68, p. 2793–2802, 2016.

[26] DERA, "Raw Material Price Monitor," Federal Institute for Geosciences and Natural Resources, 2024.

[27] "National minerals information center," [Online]. Available: https://www.usgs.gov/centers/national-minerals-information-center/commodity-statistics-and-information. [Accessed 20 05 2025].

[28] E. M. Savitskii and G. S. Burkhanov, Physical Metallurgy of Refractory Metals and Alloys, New York: Consultants Bureau, 1970, pp. 16-22; 193-199.

[29] S. V. Raj, "An evaluation of the properties of Cr,Si alloyed with Mo," *Materials Science and Engineering A,* vol. 201, pp. 229-241, 1995.

[30] A. Soleimani-Dorcheh and M. C. Galetz, "Oxidation and Nitridation Behavior of Cr–Si Alloys in Air at 1473 K," *Oxidations of Metals,* vol. 84, pp. 73-90, 2015.

[31] Y. Aono, T. Omori and R. Kainuma, "Microstructure and high-temperature strength in Cr–Si binary alloys," *Intermetallics,* vol. 112, p. 106526, 2019.

[32] A. S. Ulrich, P. Pfizenmaier, A. Solimani, U. Glatzel and M. C. Galetz, "Improving the oxidation resistance of Cr-Si-based alloys by ternary alloying," *Corrosion Science,* vol. 165, p. 108376, 2020.

[33] P. Pfizenmaier, A. S. Ulrich, U. Glatzel and M. C. Galetz, "Tensile Creep Properties of Cr-Si Alloys at 980 °C in Air - Influence of Ge and Mo Addition," *Metals,* vol. 11, no. 7, pp. 1072-1080, 2021.

[34] F. Hinrichs, A. Kauffmann, A. S. Tirunilai, D. Schliephake, B. Beichert, G. Winkens, K. Beck, A. S. Ulrich, M. C. Galetz, Z. Long, H. Thota, Y. Eggeler, A. Pundt and M. Heilmaier, "A novel nitridation- and pesting-resistant Cr-Si-Mo alloy," *Corrosion Science,* vol. 207, p. 110566, 2022.

[35] F. Hinrichs, G. Winkens, Kramer, L. K., D. Schliephake, G. Falcão, M. C. Galetz, H. Inui, A. Kauffmann and M. Heilmaier, "A ductile chromium–molybdenum alloy resistant to high-temperature oxidation," *Nature,* vol. 646, pp. 331-337, 2025.

[36] "Elements," [Online]. Available: https://www.americanelements.com/. [Accessed 14 11 2025].

[37] H. J. Maier, T. Niendorf and R. Bürgel, "Selection criteria for base elements and Overview of high-temperature material groups," in *Handbook of High-*

Temperature Materials Engineering, Wiesbaden, Springer Vieweg, 2015, p. 322.

[38] K. Ioroi, Y. Aono, X. Xu, T. Omori and R. Kainuma, "Melting point of pure Cr and phase Equilibria in the Cr-Si binary system," *Journal of Phase Equilibria and Diffusion,* vol. 43, pp. 229-242, 2022.

[39] D. Young, "The nature of high temperature oxidation," in *High temperature oxidation and corrosion of metals*, Elsevier corrosion series, 2008, pp. 12-26.

[40] G. Tammann, "Über Anlauffarben von Metallen," *Zeitschrift für anorganische und allgemeine Chemie,* vol. 111, no. 1, pp. 78-89, 1920.

[41] N. B. Pilling and R. E. Bedworth, "The oxidation of metals at high temperatures," *Journal of the Institute of Metals,* vol. 29, pp. 529-591, 1923.

[42] C. Wagner, "Oxidation of Alloys Involving Noble Metals," *Journal of the electrochemical society,* vol. 103, no. 10, pp. 571-580, 1956.

[43] C. S. Tedmon, "The effect of oxide volatilization on the oxidation kinetics of Cr and Fe-Cr alloys," *Journal of the electrochemical society,* vol. 113, no. 8, pp. 766-768, 1966.

[44] H. Taimatsu, "Kinetic Analysis of High-Temperature Oxidation of Metals Accompanied by Scale Volatilization," *Journal of The Electrochemical Society,* vol. 146, no. 10, pp. 3686-3689 , 1999.

[45] W. Hagel, "Factors Controlling the High-Temperature Oxidation of Chromium," *Transactions of American Society for Metals,* vol. 56, pp. 583-599, 1963.

[46] T. Mills, "Thermodynamic Relations in the chromium nitrogen system," *Journal of less common metals,* vol. 26, pp. 223-234, 1972.

[47] Z. Qi, B. Liu, Z. Wu, F. Zhu, Z. Wang and C. Wu, "A comparative study of the oxidation behavior of Cr2N and CrN coatings," *Thin Solid Films ,* vol. 544, p. 515–520, 2013.

[48] A. Solimani, M. Schütze, A. Stark and M. C. Galetz, "Nitrogen transport through thermally grown chromia scales," *Corrosion Science,* vol. 145, pp. 180-190, 2018.

[49] A. S. Ulrich, U. Glatzel and M. C. Galetz, "Discontinuities in Oxidation Kinetics: A New Model and its Application to Cr–Si-Base Alloys," *Oxidation of Metals,* vol. 95, pp. 445-465, 2021.

[50] A. Solimani, T. Nguyen, J. Zhang, D. J. Young and M. Schütze, "Morphology of oxide scales formed on chromium-silicon alloys at high temperatures," *Corrosion Science,* vol. 176, p. 109023, 2020.

[51] M. Guerain, F. Rakotovao, S. Y. Brou, G. Bonnet, B. Panicaud, J. L. Grosseau-Poussard and P. Goudeau, "Stress release in a-Cr 2 O 3 oxide thin films formed on Ni30-Cr and Fe47-Cr alloys," *Journal of Alloys and Compounds,* vol. 718, pp. 223-230, 2017.

[52] P. Kofstad and K. P. Lillerud, "On High Temperature Oxidation of Chromium: II . Properties of Cr2O3 and the Oxidation Mechanism of Chromium," *Journal of The Electrochemical Society,* vol. 127, no. 11, pp. 2410-2419, 1980.

[53] E. Polman, T. Fransen and P. J. Gelings, "Oxidation Kinetics of Chromium and Morphological Phenomena," *Oxidation of Metals,* vol. 32, no. 5-6, pp. 433-447, 1989.

[54] L. Latu-Romain, Y. Parsa, S. Mathieu, M. Vilasi, M. Ollivier, A. Galerie and Y. Wouters, "Duplex n- and p-Type Chromia Grown on Pure Chromium: A Photoelectrochemical and Microscopic Study," *Oxidation of Metals,* vol. 86, pp. 497-509, 2016.

[55] L. Latu-Romain, Y. Parsa and Y. Wouters, "Spallation study of chromia scales thermally grown on pure chromium in synthetic air," *Material Characterization,* vol. 152, pp. 58-66, 2019.

[56] A. S. Dorcheh, M. Schütze and M. Galetz, "Factors affecting isothermal oxidation of pure chromium in air," *Corrosion Science,* vol. 130, pp. 261-269, 2018.

[57] R. Bürgel, "Mechanismen des Deckschichtwachstums," in *Handbuch Hochtemperatur-Werkstofftechnik*, Wiesbaden, Vieweg und Sohn, 1998, pp. 272-277.

[58] R. Bürgel, "Hochtemperaturfestigkeit und -verformung," in *Handbuch Hochtemperatur-Werkstofftechnik*, Wiesbaden, Vieweg und Sohn , 2006, pp. 88-195.

[59] M. Heilmaier, *Presentation: Some fundamental topics in high temperature creep,* Manigod, 2023.

[60] D. Hull and D. Bacon, "Movement of Dislocations," in *Introduction to dislocations*, Elsevier, 2011, pp. 43-61.

[61] R. Bürgel, "Festigkeit und Verformung der Metalle," in *Festigkeitslehre und Werkstoffmechanik Band 2*, Wiesbaden, Vieweg, 2005, pp. 1-89.

[62] T. Katiyar and E. Van der Giesse, "Effective mobility of BCC dislocations in two-dimensional discrete dislocation plasticity," *Computational Materials Science,* vol. 187, p. 110129, 2021.

[63] Y. F. Gu, H. Harada and Y. Ro, "Chromium and Chromium-Based Alloys: Problems and Possibilities for High-Temperature Service," *The Journal of The Minerals, Metals & Materials Society,* vol. 56, pp. 28-33, 2004.

[64] O. N. Carlson, L. L. Sherwood and F. A. Schmidt, "The effect of low percentage alloying additions on the ductility of iodide chromium," *Journal of the less-common metals,* vol. 6, pp. 439-450, 1964.

[65] C. T. Sims, "The case for chromium," *Journal of Metals,* vol. 15, no. 2, pp. 127-132, 1963.

[66] R. E. Cairns and N. Grant, "The Effects of Carbon, Nitrogen, Oxygen, and Sulfur on the Ductile-Brittle Fracture Temperature of Chromium," *Transactions of AIME,* vol. 230, no. 5, pp. 1150-1159, 1964.

[67] H. L. Wain, F. Henderson and S. T. M. Johnstone, "A Study of the Room-Temperature Ductility of Chromium," *Journal of the,* vol. 83, pp. 133-142, 1954.

[68] H. Johanse and G. Asai, "Room-Temperature Ductile Chromium," *Journal of The Electrochemical Society,* vol. 101, no. 12, pp. 604-612, 1954.

[69] Y. Harada and M. Ohmori, "Ductile–brittle transition behavior of rolled chromium," *Journal of Materials Processing Technology,* Vols. 153-154, p. 93–99, 2004.

[70] A. Sully, Chromium, London: Butterworths Scientifi Publications, 1954.

[71] C. N. Reid and A. GIlbert, "Dislocation structure in chromium, chromium-rhenium and chromium-iron alloys," *Journal of the less-common metals,* vol. 10, pp. 77-90, 1965.

[72] J. Stephens and W. Klopp, "Ductility mechanisms and superplasticity in chromium alloys," NASA technical Note TN D-4346, Washington, D.C., 1968.

[73] W. Klopp, "Review of ductilizing of group VIA elements by rhenium and other solutes," NASA technical Note NASA TN D-4955, Washington, D.C., 1968.

[74] Y.-W. Kim, "Effects of microstructure on the deformation and fracture of y-TiAl alloys," *Materials Science and Engineering,* vol. A192, no. 193, pp. 519-533, 1995.

[75] T. Cruse and J. W. Newkirk, "Evaluation of methods to produce tough Cr3Si based composites," *Materials Science and Engineering,* vol. A239, no. 240, p. 410–418, 1997.

[76] D. M. Scruggs, "Modified chromium for unprotected structures," *American Rocket Society ,* vol. 31, no. 11, pp. 1527-1533, 1961.

[77] M. Brady, I. Anderson, M. L. Weaver, H. M. Meyer and L. Walker, "Nitrogen impurity gettering in oxide dispersion ductilized chromium," *Materials Science and Engineering A,* vol. 358, pp. 243-254, 2003.

[78] T. A. Cruse and J. W. Newkirk, "Tailoring Alloys Using Hot Pressing and Mechanical Alloying," in *Proceedings of the 1st International Non-Ferrous Processing and Technology Conference*, St.Louis, Missouri, 1997.

[79] A. S. Ulrich, P. Pfizenmaier, A. Solemani, U. Glatzel and M. C. Galetz, "Strengthened Cr-Si-base alloys for high temperature applications," *International Journal of Refractory Metals & Hard Materials,* vol. 76, pp. 72-81, 2018.

[80] R. Speiser, H. Johnston and P. Blackburn, "Vapor Pressure of Inorganic Substances III. Chromium between 1283 and 1561K," *Journal of the American Chemical Society,* vol. 72, no. 9, pp. 4142-4143, 1950.

[81] M. Venkatraman and J. P. Neumann, "The Cr-Mo (Chromium-Molybdenum) System," *Bulletin of Alloy Phase Diagrams,* vol. 8, no. 3, pp. 216-220, 1987.

[82] A. B. Gokhale and G. J. Abbaschian, "The Mo-Si (Molybdenum-Silicon) System," vol. 12, no. 4, pp. 493-498, 1991.

[83] L. Pandelaers and R. Schmid-Fetzer, Landolt-Börnstein: Ternary Alloy Systems, Subvolume E, Refractory Metal Systems, Springer, 2010, pp. 182-191.

[84] H. Wu, C. Li, C. Guo and Z. Du, "Experimental determination of the isothermal sections and the liquidus surface projection of the Mo-Si-Cr ternary system," *Journal of Alloys and Compounds,* no. 922, p. 166164, 2022.

[85] H. Wu, C. Li, C. Guo and Z. Du, "Thermodynamic assessment of the Cr-Mo-Si ternary system," *Calphad,* no. 83, p. 102631, 2023.

[86] E. Rudy and H. Nowotny, "A σ-phase in the chromium-molybdenum-silicon system," *Chemical Monthly,* vol. 105, pp. 156-168, 1974.

[87] E. R. Jett and F. Foote, "The Fe-Cr alloy system," *Metals and Alloys,* vol. 7, pp. 207-210, 1936.

[88] R. Bürgel, "Hochtemperaturlegierungen," in *Handbuch Hochtemperatur Werkstofftechnik*, Wiesbaden, Vieweg & Sohn Verlag, 2006, pp. 339-474.

[89] C.-C. Hsieh and W. Wu, "Overview of Intermetallic Sigma (σ) Phase Precipitation in Stainless Steels," *International Scholarly Research Network ISRN Metallurgy,* p. 732471, 2012.

[90] F. Long, Y. Yoo, C. Jo, S. Seo, H. Jeong, Y. Song, T. Jin and H. Z.Q., “Phase transformation of η and σ phases in an experimental nickel-based superalloy,” *Journal of Alloys and Compounds,* vol. 478, no. 1-2, pp. 181-187, 2009.

[91] E. Hornbogen and H. Warlimot, "Struktuelle Phasenumwandlungen," in *Metalle Struktur und Eigenschaftem der Metalle und Legierungen*, Berlin, Springer, 2006, pp. 159-187.

[92] A. Knowles and C. Zenk, "BCC-superalloys: Perspectives and challenges," *Scripta Materialia,* vol. 267, p. 116761, 2025.

[93] Y. Yamabe, Y. Koizumi, H. Murakami, Y. Ro, T. Maruko and H. Harada, "Development of Ir-base refractory superalloys," *Scripta Materialia,* vol. 35, no. 2, pp. 211-215, 1996.

[94] J. Calderon, M. Fine and J. Weertman, " Coarsening and morphology of β′ particles in Fe-Ni-Al-Mo ferritic alloys," *Metallurgical Transactions A,* vol. 19, p. 1135–1146, 1988.

[95] C. Stallybrass and G. Sauthoff, "Ferritic Fe–Al–Ni–Cr alloys with coherent precipitates for high-temperature applications," *Materials Science and Engineering: A,* vol. 387–389, pp. 985-990, 2004.

[96] K. Ma, T. Blackburn, J. P. Magnussen, M. Kerbstadt, P. A. Ferreirós, T. Pinomaa, C. Hofer, D. G. Hopkinson, S. J. Day, P. A. J. Bagot, M. P. Moody, M. Galetz and A. J. Knowles, "Chromium-based bcc-superalloys strengthened by iron supplements," *Acta Materialia,* vol. 257, p. 119183, 2023.

[97] L. Royer, S. Mathieu, C. Liebaut and P. Steinmetz, "Study of the microstructure and oxidation behavior of chromium base alloys strengthened by NiAl precipitates," *Materials Science Forum - Conference Paper,* Vols. 595-598, pp. 117-125, 2008.

[98] Ö. N. Doğan, X. Song, D. Palacio and M. Gao, "Coherent precipitation in a high-temperature Cr–Ni–Al–Ti Alloy," *Journal of Material Science,* vol. 49, pp. 805-810, 2014.

[99] A. Knowles, D. Dye, R. Dodds, A. Watson, C. Hardie and S. Humphry-Baker, "Tungsten-based bcc-superalloys," *Applied Materials Today,* vol. 23, p. 101014, 2021.

[100] A. Knowles, T.-S. Jun, A. Bhowmik, N. Jones, T. Britton, F. Giuliani, H. Stone and D. Dye, "A new beta titanium alloy system reinforced with superlattice intermetallic precipitates," *Scripta Materialia,* vol. 140, pp. 71-75, 2017.

[101] T. Hughes, E. Lautenschlager, J. Cohen and J. Brittain, "XRay Diffraction Investigation of β′NiAl Alloys," *Journal of Applied Physics,* vol. 42, no. 10, pp. 3705-3716, 1971.

[102] S. A. Kube, C. Frey, C. McMullin, B. Neuman and K. M. Mullin, "Navigating the BCC-B2 refractory alloy space: Stability and thermal processing with Ru-B2 precipitates," *Acta Materialia,* vol. 265, p. 119628, 2024.

[103] A. Förner, S. Giese, A. Felfer, C. Körner, S. Neumeier and M. Göken, "Nanoscaled eutectic NiAl-(Cr,Mo) composites with exceptional mechanical properties processed by electron beam melting," *Scientific reports ,* vol. 10, p. 15153, 2020.

[104] H. Cline and J. Walter, "The Effect of Alloy Additions on the Rod-Plate Transition in the Eutectic NiAl-Cr," *Metallurgical Transactions,* vol. 1, pp. 2907-2917, 1970.

[105] D. Wang, H. Ning, B. Wang, G. Liu and S. Yuan, "Fabrication of a NiAl–Cr(Mo) eutectic alloy with network microstructure for high-temperature

strengthening," *Materials Science and Engineering: A,* vol. 835, p. 142628, 2022.

[106] C. Gombola, A. Kauffmann, G. Geramifard, M. Blankenburg and M. Heilmaier, "Microstructural Investigations of Novel High Temperature Alloys Based on NiAl-(Cr,Mo)," *metals,* vol. 10, no. 961, 2020.

[107] H. Mehrer, "Interdiffusion and Kirkendal Effect," in *Diffusion in Solids: Fundamentals, Methods, Materials Diffusion-Controlled Processes*, Berlin, Springer, 2007, pp. 161-176.

[108] P. Kofstadt, "General Introduction," in *High temperature Corrosion*, New York, Springer, 1988, p. 5.

[109] A. S. Ulrich, "Entwicklung von ausscheidungshärtbaren Cr-Si-Basis-Legierungen für Hochtemperaturanwendungen: Mikrostruktur und Oxidation," Shaker Verlag, Frankfurt am Main, 2020.

[110] J. Smialek and G. H. Meier, "High temperature oxidation," in *Superalloys II*, Wiley-VCH GmbH & Co. KGaA., 1987, p. 293–326.